International journal for science, technics and innovations for the industry

MTM
MACHINES TECHNOLOGIES MATERIALS

ISSN PRINT 1313-0226
ISSN WEB 1314-507X
Issue 4 / 2019
YEAR XIII



Published by
Scientific technical
Union of Mechanical Engineering

MACHINES. TECHNOLOGIES. MATERIALS

INTERNATIONAL SCIENTIFIC JOURNAL

PUBLISHER

SCIENTIFIC TECHNICAL UNION OF MECHANICAL ENGINEERING "INDUSTRY 4.0"

108, Rakovski Str., 1000 Sofia, Bulgaria
tel. (+359 2) 987 72 90,
tel./fax (+359 2) 986 22 40,
office@stumejournals.com
www.stumejournals.com

ISSN PRINT 1313-0226, ISSN WEB 1314-507X, YEAR XIII, ISSUE 4 / 2019

EDITOR-IN-CHIEF

Prof. D.Sc. DHC Georgi Popov,
President of Bulgarian Scientific and Technical Union of Mechanical Engineering

EDITORIAL BOARD

MEMBERS	SCIENTIFIC COMPETENCE
Prof. Dimitar Damyanov	Automatisation of production
Prof. Dimitar Karaivanov	Mechanics of machines
Prof. Dimitar Stavrev	Technologies and materials
Prof. Dimitar Yonchev	National and industrial security
Prof. Galina Nikolcheva	Machines tools and technologies
Prof. Hristo Shehtov	Automatisation of production
Prof. Idilija Bachkova	Automatisation of production
Prof. Ivan Kralov	Mechanics of machines
Prof. Ivan Parshorov	Technologies and materials
Prof. Ivan Yanchev	Machines and technologies
Prof. Ivo Malakov	Automatisation of production
Prof. Kiril Angelov	Industrial Management
Prof. Lilo Kunchev	Transport Equipment and Technology
Prof. Lubomir Dimitrov	Machines and technologies
Prof. Miho Mihov	Agricultural machinery
Prof. Miroslav Denchev	Ergonomics and design
Prof. Mladen Velev	Economics and Marketing
Prof. Nikolay Diulgerov	Technologies and materials
Prof. Ognyan Andreev	Production management
Prof. Petar Kolev	Transport Equipment and Technology
Prof. Roman Zahariev	Robotics
Prof. Sasho Guergov	Robotic systems and technology
Prof. Tsanka Dikova	Technologies and materials
Prof. Vitan Galabov	Mechanics of machines

MACHINES. TECHNOLOGIES. MATERIALS

INTERNATIONAL SCIENTIFIC JOURNAL

ISSN PRINT 1313-0226, ISSN WEB 1314-507X, YEAR XIII, ISSUE 4 / 2019

EDITORIAL BOARD FOREIGN MEMBERS			
Prof. Adel Mahmoud	IQ	Prof. Marian Tolnay	SK
Prof. Ahmet Ertas	TR	Prof. Mark Easton	AU
Prof. Andonaq Londo	AL	Prof. Mart Tamre	EE
Prof. Andrei Firsov	RU	Prof. Maryam Ehteshamzade	IR
Prof. Andrzej Golabczak	PL	Prof. Michael Evan Goodsite	DK
Prof. Anita Jansone	LV	Prof. Mihail Aurel Titu	RO
Prof. Aude Billard	CH	Prof. Movlazade Vagif Zahid	AZ
Prof. Bojan Dolšak	SI	Prof. Natasa Naprstkova	CZ
Prof. Christian Marxt	LI	Prof. Oana Dodun	RO
Prof. Dale Carnegie	NZ	Prof. Oleg Sharkov	RU
Prof. Emilia Abadjieva	BG	Prof. Páll Jensson	IS
Prof. Ernest Nazarian	AM	Prof. Patrick Anderson	NL
Prof. Esam Husein	KW	Prof. Paul Heuschling	LU
Prof. Ewa Gunnarsson	SW	Prof. Pavel Kovac	RS
Prof. Filipe Samuel Silva	PT	Prof. Per Skjerpe	NO
Prof. Francisco Martinez Perez	CU	Prof. Péter Korondi	HU
Prof. Franz Haas	AT	Prof. Peter Kostal	SK
Prof. Genadii Bagliuk	UA	Prof. Juan Alberto Montano	MX
Prof. Georg Frey	DE	Prof. Raul Turmanidze	GE
Prof. Gregory Gurevich	IL	Prof. Renato Goulart	BR
Prof. Haydar Odinaev	TJ	Prof. Roumen Petrov	BE
Prof. Hiroyuki Moriyama	JP	Prof. Rubén Darío Vásquez Salazar	CO
Prof. Dr. Ilir Doci	Ko	Prof. Safet Isić	BA
Prof. Iryna Charniak	BY	Prof. Sean Leen	IE
Prof. Ivan Svarc	CZ	Prof. ShI Xiaowei	CN
Prof. Ivica Veza	HR	Prof. Shoirdzan Karimov	UZ
Prof. Jae-Young Kim	KR	Prof. Sreten Savićević	ME
Prof. Jerzy Jedzejewski	PL	Prof. Stefan Dimov	UK
Prof. Jean-Emmanuel Broquin	FR	Prof. Svetlana Gubenko	UA
Prof. Jordi Romeu Garbi	ES	Prof. Sveto Cvetkovski	MK
Prof. Jukka Tuhkuri	FI	Prof. Tamaz Megrelidze	GE
Prof. Katia Vutova	BG	Prof. Tashtanbay Sartov	KG
Prof. Kazimieras Juzėnas	LT	Prof. Teimuraz Kochadze	GE
Prof. Krasimir Marchev	USA	Prof. Thorsten Schmidt	DE
Prof. Krzysztof Rokosz	PL	Prof. Tonci Mikac	HR
Prof. Leon Kukielka	PL	Prof. Vasile Cartofeanu	MD
Prof. Mahmoud El Gammal	EG	Prof. Yasar Pancar	TR
Prof. Manolakos Dimitrios	GR	Prof. Yurij Kuznetsov	UA
Prof. Marat Ibatov	KZ	Prof. Wei Hua Ho	ZA
Prof. Marco Bocciolone	IT	Prof. Wu Kaiming	CN

C O N T E N T S

MACHINES

RELIABILITY EVALUATION OF ELECTRONIC COMPONENT IN MILITARY VEHICLES UNDER THERMAL EXPOSURE AND THERMAL CYCLING BY ACCELERATED TEST METHOD
Xuan Phong Cu, Ha Anh Bui..... 149

QUALITY CONTROL OF MULTI-PASS WELD BY MEANS OF ACOUSTIC EMISSION
Dmitry S. Bals, M Sc. Eng. Education, Leonid A. Vinogradov, M Sc. Eng. Education Yulija Soldatova, M Sc. Eng. Education 152

SYSTEM FOR PROCESSING CONCENTRATED AND NON-CONDENSING GASES IN BOILERS
Ch. Assistant Dr. Eng. Madzharova St., Assoc. Prof. Dr. Petrova T., Prof. Dr. Eng. Bozukov N. 155

STATISTICAL ANALYSIS OF LOCOMOTIVES TRACTION MOTORS PERFORMANCE
Oleksander Gorobchenko, Victor Tkachenko 158

EXERGY ANALYSIS OF WET COOLING TOWER AT VARIOUS LOADS AND AMBIENT TEMPERATURES
PhD. Mrzljak Vedran, PhD. Orović Josip, PhD. Poljak Igor, PhD Student Eng. Kocijel Lino 162

TECHNOLOGIES

PREPARATION AND PROPERTIES OF CARBON ADSORBENTS BASED ON PLANT RAW MATERIALS AND POLYMERIC WASTE
Assoc. Ph.D. Nistratov A.V., Prof. Dr. Klushin V.N. 166

SUPPLY CHAIN PLANNING METHODOLOGY FOR METALS
Ass. Prof., Candidate of Technical Sciences, Solodovnikov V. 171

TRAFFIC SYNTHETIC MODEL DEVELOPMENT AND CALIBRATION IN ANAMORAVA REGION
Dr.sc. Ramadan Duraku, Prof.dr.Vaska Atanasova 173

MATERIALS

RESEARCH INTO THE EFFECT OF CERTAIN CHEMICAL ELEMENTS IN MICROALLOYED STEEL GRADES ON CONCAST SLAB AND ROLLED PLATE SURFACE QUALITY
O. Isayev, O. Hress, S. Yershov, M.Q. Huang, K.L. Zhang 178

EVALUATION OF MECHANICAL PROPERTIES OF DUCTILE CAST IRON AND INVERSE REGRESSION
Assoc. Prof, PhD. Alexander Popov, PhD. Mr. Eng. Jan Ivanov , Br. Eng. Stefan Georgiev 183

THE INFLUENCE OF NATURAL AGING AND PRE-AGING ON THE MECHANICAL, PHYSICAL AND MICROSTRUCTURAL PROPERTIES OF THE EN AW-6060 ALUMINUM ALLOY
MSc. Stamenković U., Prof. Dr Ivanov S., Assist. Prof. Marković I., Prof. Dr Mladenović S., Prof. Dr Manasijević D., Prof. Dr Balanović Lj. 187

MATERIALSCIENCE – MATHEMATICS AND PHYSICS FOR EVALUATION OF LIQUIDS IN FOUNDRY
Chi. Ass. Eng. A. Maheva, PhD., Ass. Prof. Eng. St. Bushev, PhD. 190

THE MAXIMAL VALUES OF PACKING COEFFICIENT FOR PARTICLES WITH DIFFERENT FORMS
Prof. Dr. Phys. and Math. Liopo V., Mast. of Phys. Liaushuk I., Assoc. Prof. Dr. Eng.Auchynnikau Y. , Assoc. Prof. cand. Phys. and Math. Sabutz A., Assoc. Prof. cand. Eng. Sarokin V., PhD Yankov E. 194

RELIABILITY EVALUATION OF ELECTRONIC COMPONENT IN MILITARY VEHICLES UNDER THERMAL EXPOSURE AND THERMAL CYCLING BY ACCELERATED TEST METHOD

Xuan Phong Cu[1*], Ha Anh Bui[2]
[1]Faculty of Military Technology, University of Defence, Brno, Czech Republic
[2] University of Fire Fighting and Prevention, Hanoi, Vietnam

Abstract. *The majority of electronic components are susceptible to damage at high temperatures (overheating) and their reliability is affected by its operating temperature. The temperature can basically dictate the effective performance as well as the lifetime or life cycle of the electronic components. In addition, the reliability of electronic components is not only affected temperatures but also by changes in temperature over a period of time (thermal cycles). This article describes the methodology how to prepare, perform and evaluate the accelerated reliability compliance test of electronic components in military vehicles under thermal exposure and thermal cycling.*

1 Introduction

At present, the number of electronic components in military vehicles has greatly increased, combat vehicles achieve the parameters of the major military characteristics (tactical-technical parameters) through a high proportion of electronic components with digital control. These electronic components contribute significantly to the achievement of the reliability of vehicles. The military vehicle is considered a system of the overall defence system, in which crew members can receive and transmit orders (by voice, text, video, etc.), data exchange (point locations, area boundaries, logistic state, etc.) with partners. Therefore, combat vehicles are equipped with sophisticated communications systems including Battle Management Systems (BMS), Tactical Radio, Navigation Systems, Headsets, etc. At the same time, electronic and electromechanical technologies are replacing mechanical and hydraulic solutions in combat vehicles. For example, the electric turret motor has become popular, electro-mechanical transmissions are increasingly used to replace mechanical transmissions. The new operational systems are integrated into combat vehicles such as electrochemical or electromagnetic energy propelled ammunitions, active electromagnetic protections, active suspensions [1].

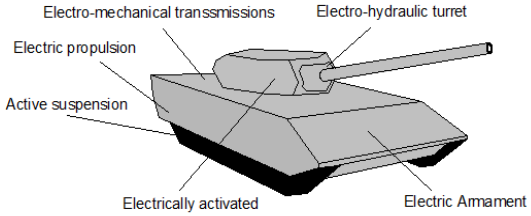


Fig. 1. *Electronic system in modern combat vehicles [1]*

Due to the increasing number of electronic systems in military vehicles, it can be said that this is the process of digitizing military technology. The reliability of the electronic components characterizes the resulting values of the reliability of the entire electronic system in military vehicles. Electronic component failure can lead to catastrophic effects in combat operations. For this reason, it is necessary to study and develop methods for predicting the reliability of electronic components used in military vehicles. At present, reliability of electronic components is estimated by using the standard handbook, statistical analysis of operation & maintenance data (reliability database) or performing reliability testing [2]. In general, the use of standard handbooks (e.g. MIL-HDBK-217, RIAC-217, PRISM), and reliability database (e.g. EPRD-2G14, FMD-2G16), have some inherent limitations such as these methods are based on assumptions about a constant failure rate that may incorrectly reflect the failure trend in the product life cycle; the methods cannot indicate basic failure mechanisms and do not provide the root cause of failure; the methods are not effective in predicting the reliability of new electronic components, etc. Hence, in order to obtain failures data of electronic components for analysing their failure modes and understanding life characteristics in a short period of time, another approach is developed, i.e. accelerated test method. This method has become increasingly important because of the need to develop newer, higher technology product, the shorter period between product design and release while improving productivity, quality, and reliability.

2 Effect of temperature and thermal cycling

There are many factors that influence on the reliability of electronic components, such as temperature, thermal cycling, heat shock, humidity, voltage, current, mechanical stress (vibration, shock) or combination of stresses. In this study, we conducted an accelerated reliability test (ART) with the combined temperature and thermal cycling stress to evaluate their influence on the product reliability.

2.1. Temperature

Most electronic components are susceptible to damage at high temperatures (overheating) and their reliability is influenced by its operating temperature [3]. It can be said that temperature is the enemy of reliability of all electronic components. Therefore, when analysing system errors of electronic components, it usually involves examining evidence or signs of overheating. Studies have also shown that there is a relationship between the performance, lifetime or life cycle of an electronic component with its specific operating temperature range. The temperature can basically dictate the effective performance as well as the lifetime or life cycle of the electronic components.

The temperature on electronic component includes the temperature of the environment (generated by the direct influence of solar radiation and heat exchange) and the temperature generated when the device is in operation. For example, the heat source is generated by the engine, by the action of friction and it is transmitted from mechanical energy to heat, the conductors emit heat when the current passes through, the heat dissipation from the semiconductor device, etc. High and low temperatures can make electronic components unsafe or unsuitable for use because they change the properties of materials used in the construction of electronic components. Failure mechanisms of electronic components due to high temperature are oxidation, physical expansion, softening/melting, chemical decomposition, etc., while due to low temperature are physical contraction, ice formation, embrittlement [4].

2.2 Thermal cycling

The reliability of electronic components is not only affected by low and high temperatures, but also by changes in temperature over a period of time (thermal cycles). These temperature variations depend on operating cycles of the electronic components (on/off) and variations in its environment (e.g. day/night). The thermal cycling particularly stresses on the solder joints, die attachments, wire bonds which can lead to catastrophic failure of the electronic components (e.g. breaking of solder joints, loss of conductive contact, deformation of the processor plate). The most common failure mode due to thermal cycling is fatigue. The lifetime of an item under thermal cycling stress depends on the thermal cycling profile, the coefficients of thermal expansion, and other material properties that determine crack initiation and propagation rates [5].

A thermal cycle is characterized by high temperature (T_{max}), low temperature (T_{min}), dwell time at high temperature (τ_{dw_high}), dwell time at low temperature (τ_{dw_low}), and rate of temperature change. Reliability testing with thermal cycling is specified in many different technical standards as an integral part of

environmental stress testing. For example, standard JESD22-A104E recommends thirteen thermal cycling test conditions for electronic components and solder interconnects [6]; standard MIL-STD-883F recommends six thermal cycling profiles for microcircuits [7].

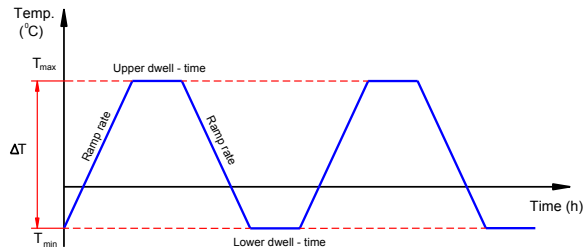


Fig. 2. *Schematic of temperature cycle profile [5]*

3 Design of accelerated reliability testing

3.1 Test conditions and stress levels

To successfully design an ART, it is necessary to have a good knowledge of the intended use environment, the environment profile and operating conditions of the product as well as product design capabilities [8]. In this case study, electronic components are designed for use in combat vehicles with the following operating and environmental conditions.

Table 1*. Operating conditions of electronic components*

Parameter	Symbol	Value
Required life	τ_r	15 years = 131400 h
Time - ON	τ_{ON}	4h/day = 21900 h
Temperature - ON	T_{ON}	60 °C
Time - OFF	τ_{OFF}	109500 h
Temperature – OFF	T_{OFF}	25 °C
Temperature change	ΔT_{use}	45 °C
Rate of temperature change	ξ_{use}	1.5 °C/min
Number of thermal cycles per day	N_{cy}	2
Total cycles	N_o	10950

In ART, to simulate a lifetime of actual stresses that the product will be exposed to, all of the test units are subject to each of the stresses in the entire test sequence. The failure data of the test units is required to estimate the reliability in the field and in order to obtain this information quickly, electronic components need to be operated at elevated stress conditions. The nominal time of testing for these stresses is determined based on the cumulative damage model, in which the equivalent test damage occurs by increasing the amplitudes of each individual stresses but ensuring within the maximum design limit of products.

In this paper, we focus on the effect of temperature, thermal cycle to reliability of electronic components. The characteristics of the thermal cycle in ART include the high temperature ($T_{\max}$) of 100 °C, low temperature ($T_{\min}$) of -40 °C, rate of temperature change in test (ξ_{test}) of 3.0 °C/min. The temperature change of ART is:

$$\Delta T = T_{\max} - T_{\min} = 140\ ^{o}\mathrm{C}$$

With the test stress is thermal cycle, according to Coffin-Manson model [8], the acceleration factor is:

$$A_{TC} = \left(\frac{\Delta T_{use}}{\Delta T_{test}}\right)^{-2} \cdot \left(\frac{\xi_{use}}{\xi_{test}}\right)^{-1/3} = 12.2$$

The total number of cycles of ART is then:

$$N_{test} = \frac{N_o}{A_{TC}} = \frac{10950}{12.2} = 897 \text{ cycles}$$

To determine the test time in ART under thermal stress, the time at the off- state (time – OFF) is normalized to the equivalent time at the on- state (time – ON).

$$\tau_{ON-N} = \tau_{ON} + \tau_{OFF} e^{\frac{E_a}{k_B}\left(\frac{1}{273+T_{OFF}} - \frac{1}{273+T_{ON}}\right)}$$

where E_a is the activation energy (eV); k_B is the Boltzmann's constant, k_B = 8,617385.10^{-5} (eV/K). The values of the activation energy for electronic component can be found in [9] ranging from 0.3 to 0.8 eV (see Table 2). In this case study, E_a = 0.8 eV is selected, then the equivalent time is:

$$\tau_{ON-N} = 21900 + \frac{109500}{26.4} = 26047 \text{ h}$$

Table 2*. Activation energies in different standards [9]*

Electronic components	MIL-HDBK-217F	RDF 2000 (2000)	RIAC-217 plus (2007)	FIDES (2009)
Bipolar logic	0.4 eV	0.4 eV	0.8 eV	0.7 eV
CMOS logic	0.35 eV	0.3 eV	0.8 eV	0.7 eV
BICmos logic	0.5 eV	0.4 eV	0.8 eV	0.7 eV
Linear	0.65 eV		0.8 eV	0.7 eV
Memories	0.6 eV		0.8 eV	0.7 eV
VHSIC	0.4 eV		0.8 eV	0.7 eV

With the test stress is temperature, Arrhenius model is used to calculate the acceleration factor [8].

$$A_T = e^{\frac{E_a}{k_B}\left(\frac{1}{273+T_{ON}} - \frac{1}{273+T_{test}}\right)} = 19.8$$

The necessary test duration of ART is:

$$\tau_{test} = \frac{\tau_{ON-N}}{A_T} = \frac{26047}{19.8} = 1315 \text{ h}$$

When conducting tests with a combination of thermal exposure and thermal cycling, thermal exposure over the high temperature of the thermal cycling is used to determine the dwell time at high temperature. Thus, dwell times at high temperature is:

$$\tau_{dw-high} = \frac{\tau_{test}}{N_{test}} = \frac{1315}{897} = 1.45 \text{ h} = 87 \text{ min}$$

The dwell time at low temperature of 45 min is selected to ensure the homogeneous temperature in the chamber was provided when reaching a maximum or a minimum temperature. The test duration of a temperature cycle is:

$$\tau_{TC} = 2\frac{\Delta T_{test}}{60\xi_{test}} + \tau_{dwell_high} + t_{dwell_low} = 225 \text{ min}$$

Table 3*. Test conditions*

Thermal Cycles	Number of Cycles	Current (mA)
-40 °C /45 min +100 °C /87 min 3 °C /min	897	1050
		525
		210

3.2 Experimental setup

The experiment has been conducted on Light Emitting Diodes (LEDs) in combat vehicles. The electrical and optical characteristics of the high-power LED at ambient temperature of 25 °C are described in Table 4.

Table 4. *Electrical-optical characteristics of LED*

Parameter	Min	Typ	Max	Unit
Luminous Flux	700	~	800	lm
Correlated Color Temperature/ Wavelength	2900	~	3200	K/nm
Color Rendering Index (CRI)	60	~	90	~
Forward Voltage	9	~	11	V
Power Dissipation	~	9.45	~	W
View Angle	~	90	~	deg.
Thermal Resistance	~	12	~	°C/W

The LEDs were placed in the climate chamber Votsch VC3 7034. The LEDs are then connected to the DC power supply (Keysight E3634A) and measure unit (Keysight 34980A Multifunction Switch/Measure Unit). The LEDs are supplied constant currents, and voltage in each LED are measured every 10 minutes. The measured values were continuously recorded using a PC with BenchLink Data Logger Pro software. The experimental setup for the ART of the high-power LEDs is shown in Fig.3.

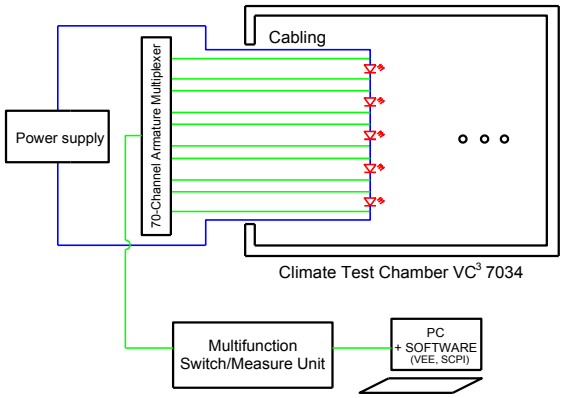


***Fig. 3** Experimental arrangements*

3.3 Experimental procedure

The thermal cycles were set so that after the test begins, the LEDs can be heated to +100 °C. When this temperature was reached, it was kept in the climate chamber for 87 minutes. The cooling cycle was then started, and LEDs were continually cooled to -40 °C. When this temperature was reached, the control program kept the temperature in the climate chamber for 45 minutes. After that, the heating cycle started again, and LEDs were continually heated to the maximum temperature (+100 °C). The speed of temperature change in test is 3 °C/min, and test duration of a thermal cycle is 225 minutes. The number of test samples includes 20 LEDs at current of 1050 mA (condition A), 25 LEDs at current of 525 mA (condition B), 30 LEDs at current of 210 mA (condition C). The test is terminated at test time of 897 cycles. The number of failures during the test is also a variable random. The failed units are not replaced by new ones during the test.

For LED reliability testing, there are two types of failure that are evaluated, i.e. catastrophic and degradation failure [10]. However, in the tests were performed above, all observed failures were catastrophic with open circuit failure. This failure is detected when the bias voltage drops to zero.

4 Evaluation of accelerated reliability testing data

The results of ART are evaluated using the principle of confidence limit and predicting the lower one-sided confidence of mean time to failure ($MTTF_L$). The formulas for establishing one-sided (i.e., lower limit) confidence limits on $MTTF_L$, respectively, are as follows [11]:

$$MTTF_L = \frac{2T_{OE}}{\chi^2_\alpha(\nu)}$$

where $\chi^2_\alpha(\nu)$ is the chi-squared distribution for number of degrees of freedom ν at confidence level α; T_{OE} is accumulated test time. The number of degrees of freedom is specified for each case related to the number of failures r recorded in the test. In case of test without replacement of failed units, the number of degrees of freedom is given by [11]:

$$\nu = 2r + 1$$

The accumulated test time depends on the test plan, number of samples and failures recorded in the test. Test is terminated at a pre-assigned test duration τ_o, without replacement of failed units, the accumulated test time is defined as follows [11]:

$$T_{OE} = \sum_{i=1}^{r} t_i + (n - r)\cdot\tau_o$$

where n is the sample size, t_i is the failure time of the i[th] sample; τ_o is the test time.

The experiments are still in progress. In the test, with condition A, the number of samples is 20 LEDs (n = 20). For example, during the test, four failed samples are observed (r = 4). The first failure occurs at N_1 = 405 cycles, the second failure at N_2 = 535 cycles, the third failure at N_3 = 715 cycles, and the fourth failure at N_4 = 845 cycles. The accumulated test time in this case is:

$$T_{OE} = \sum_{i=1}^{4} N_i \text{A}_{TC} + (20 - 4)\cdot N_o = 211465 \text{ cycles}$$

With the confidence level for reliability evaluation of $\alpha = 0.95$ and $\nu = 2\times4 + 1 = 9$, the chi-squared distribution is:

$$\chi^2_{0.95}(7) = 16.9$$

$MTTF_L$ of LED is then:

$$MTTF_L = 24343 \text{ cycles}$$

This corresponds to approximately 33.4 years under given conditions (as shown in Table 1).

5 Conclusion

This paper presents the effect of temperature and thermal cycling on the reliability of electronic components, and methodology how to prepare, perform and evaluate the ART of electronic components in military vehicles under their influence. LEDs were selected for testing because they are not only widely in many important applications, but they are also used in military equipment, especially in military vehicles. Based on operating and environmental conditions of military vehicles, combination of temperature and thermal cycling was used to conduct experiments. A monitoring system was set up to detect catastrophic failures and degradation failures of test units during testing. The ART is still undergoing. The information from tests will be analyse based on the principle of confidence limits on MTTF.

Acknowledgment

This paper has been prepared with the support of the Ministry of Defence of the Czech Republic, Partial Project for Institutional Development, MOBAUT, University of Defence, Brno.

References

1. KOLEKTIV. Military Vetronics Association. MILVA Vetronics handbook, NATO-LG/3, Brusel, 2006.
2. P. V. Varde. Physics-of-failure based approach for predicting life and reliability of electronics components. Barc Newsletter, **313** (2010).
3. L.M. Klyatis, E. Klyatis. Accelerated quality and reliability solutions. Elsevier, 2010.
4. S. U. M. Rao. Influence of environmental factors on component/equipment reliability. Indian Journal of Engineering & Materials Sciences, **5 (**1998).
5. G. Yang. Life cycle reliability engineering. New Jersey, Wiley, **10** (2007).
6. JESD22-A104E. Temperature Cycling. JEDEC solid state technology association, 2009, 18 p.
7. MIL-STD-883F. Test method standard microcircuits. Washington: US Department of Defense, 1997, 641 p.
8. IEC 62506. Methods for product accelerated testing. IEC, 2013, 88 p.
9. F. Bayle, A. Metta. Temperature acceleration models in reliability predictions: Justification & improvements. Proceedings-Annual Reliability and Maintainability Symposium (RAMS). IEEE, 2010.
10. M. H. Chang, et al. Light emitting diodes reliability review. Microelectronics Reliability, **5** (2012).
11. IEC 60605-4. Equipment reliability testing - Part 4: Statistical procedures for exponential distribution – Point estimates, confidence intervals, prediction intervals and tolerance intervals. IEC, 2001.

ABOUT WAVEGUIDE MODELING (TRANSMISSIONS OF ULTRASONIC TECHNOLOGICAL MACHINES)

Vitaly Krupenin, Vladimir Astashev
Mechanical Engineering Research Institute of the Russian Academy of Sciences, Moscow, Russia

Abstract. *The modeling of energy transfer systems in ultrasonic technological machines is considered. As such systems rod waveguides are usually used. These are, as a rule, distributed systems of variable cross-section, which must transmit energy from an electromechanical vibration exciter to a working body. Sometimes additional equipment is attached to the waveguide (core system), which should be modeled using lumped-parameter subsystems. This article discusses the problems related to the modeling and calculation of the so-called ultrasonic concentrators - waveguides that have a heterogeneous shape and are made to ensure optimal energy delivery to the working body (instrument). Examples of calculations are given that consider the influence of a nonlinear elastic-dissipative load, determined by the nature of the technological process. The analysis of real models is described*.

1 Introduction

Ultrasonic technologies make it possible to organize a universal way of highly effective effects on workpieces and environments. Three main components define ultrasonic machines: "electromechanical vibration exciter - waveguide (concentrator) - technological process". Thus, waveguides define the transmission systems of ultrasonic machines. This is, as a rule, a rod systems with distributed parameters, designed to transfer the energy of the exciter to the working part of the machine.

This paper discusses the problems of modeling and calculating the so-called ultrasonic concentrators - waveguides, which have a non-uniform shape and are made to ensure optimal energy delivery to the instrument.

The methods for calculating waveguides for ultrasonic machines under the assumption of linearity of rod systems are based on the methods of dynamic compliance, which are determined by solving the corresponding equations of motion in partial derivatives. When considering in the model of the workflow, which consists, in particular, in the interaction of the tool with the processed medium or workpieces, the equations of motion become strongly nonlinear and the methods for their analysis change. An efficient and fairly easy to interpret way to study the models under consideration is provided by frequency methods based on the ideas of equivalent linearization.

2 Source models

The theory of ultrasonic concentrators, suggesting their perfect matching at idle, is developed in [1-5]. Below will be considered models of rod concentrators with internal energy loss. The cross section x=0 of the concentrator 1 (Fig.1) is connected with the exciter oscillations 2, and in the section $x=l$ the tool 3 is fixed, which interacts with the workpiece or medium 4.

The oscillations of the cross section x of the concentrator will be described by the function $u_x(t) = a_x \exp i(\omega t - \varphi_x)$, where a_x, ω, φ_x — amplitude, frequency and initial phase.

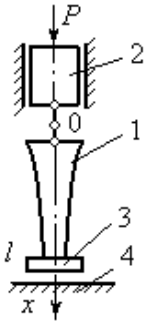


Fig. 1. *The scheme of the ultrasonic process.*

In technological ultrasonic machines and devices, the load on the oscillatory system from the side of the processed workpieces and media is, as a rule, non-linear. The corresponding reaction force can be represented as follows: $f(u_l) = [k(a_l) + j\omega\beta(a_l)]u_l$. Here and below, nonlinear forces are written using techniques equivalent linearization [4, 5]. The nonlinearity of the load is manifested in the fact that its elastic and dissipative components are dependent on the amplitude of oscillations of the tool. This dependency was repeatedly observed experimentally and was described in detail for a long time [6].

Mutual influence of the concentrator and the causative agent of oscillations will be assessed by the force acting in the place of their joint $f_0(t) = F_0 \exp i\omega t$.

The motion of the concentrator will be determined using the magnitude of the dynamic compliance $L_s(x, i\omega)$ that relates the displacement of u_x cross sections x with reactions $f(u_l)$, $f_0(t)$ and the inertial force $-M\omega^2 u_l$ from the attached tool with a mass M acting in cross sections s=0,l:

$$u_x(t) = L_{0x}(i\omega)F_0 \exp i\omega t - L_{0x}(i\omega)\left[g(a_l) - M\omega^2\right]u_l, \quad (1)$$

and $g(a_l) = k(a_l) + \beta(a_l)$. After a series of transformations, we find the formulas for the amplitude and phase of moving the cross-section of the concentrator at $x = l$:

$$a_l = F_0 |W(a_l i\omega)|^{-1} = F_0[(\mathrm{Re}W)^2 + (\mathrm{Im}W)^2]^{-0,5} \quad (2)$$

$$\cos\varphi_l = a_l F_0^{-1} \mathrm{Re}W(a_l, i\omega); \ \sin\varphi_l = a_l F_0^{-1} \mathrm{Im}W(a_l, i\omega).$$

We introduce the designation of dynamic stiffness:

$W(a_l, i\omega) = \{1 + L_l(l, i\omega)[k(a_l) - M\omega^2 + i\omega\beta(a_l)]\}L_0^{-1}(l, i\omega)$. Let $W_{sx}(i\omega) = U_{sx}(\omega) + iV_{sx}(\omega)$.

It is assumed that the level of damping is small, i.e. small quantities $V_{sx}(\omega), \beta(a_l)$. Equation (2) determines the amplitude-frequency characteristic of the concentrator when a force acts at the end of x = 0. The maximum amplitude of the instrument is achieved under the condition $\mathrm{Re}W(a_l, i\omega)$ =0, which can be brought to the following form: $U_{ll}(\omega) + k(a_l) - M\omega^2 = 0$.

In this case, of course, any given amplitude a_l is provided by some minimum force F_0. Consequently, the last relation turns out to be the condition for the best matching of the vibration exciter with the concentrator. We emphasize that in this case the concentrator carries a tool with a mass M and operates on a non-linear technological load.

Considering the obtained equalities, we find

$$K = \frac{a_l}{a_0} = \left|\frac{U_{00}(\omega)}{U_{0l}(\omega)}\right|. \quad (3)$$

By analogy with [1, 2, 5], the value $K = a_l / a_0$ characterizing the degree of transformation of the level of oscillations transmitted from the exciter to the tool will be called the gain coefficient of the concentrator. Note that the expression (3) in its form coincides with the previously known equality [4, 5], which determines the gain factor of the unloaded concentrator. For a given amplitude value a_0 of the exciter of the oscillations, the relation (3) immediately determines the amplitude of the working end of the concentrator, which satisfies the given condition of the best matching under load.

* Corresponding author: krupeninster@gmail.com

3 Attaching a concentrator

It should be noted that the attachment of the concentrator leads to the loading of the pathogen. Let the pathogen is not loaded by the concentrator and oscillates in accordance with the law of motion. $u_0^*(t) = = a_0^* \exp i(\omega t - \varphi)$.

At the point of connection of the concentrator on the vibration exciter force -$f_0(t)$. His movement under load will be described by the equation $u_0(t) = u_0^*(t) - f_0(t)W_0^{-1}(i\omega)$, where $W_0(i\omega) = = U_0(\omega) + iV_0(\omega)$ - dynamic stiffness of the exciter at the point of attachment of the concentrator.

Using the derived ratios, the magnitude of the reaction can be represented as $f_0(t) = iu_0(t)K^2\left[V_{ll}(\omega) + \omega\beta(a_l)\right]$.

In the books [4, 5], it was shown that in ultrasonic technological installations, resonant electroacoustic transducers are usually used as exciters. The condition of their resonant tuning is $U_n(\omega) = 0$. Now for the loaded transducer we get:

$$u_0(t) = u_0^*(t)\left[1 + V_{ll}(\omega) + \omega\beta(a_l)V_n^{-1}(\omega)K^2\right]^{-1}. \quad (4)$$

It follows that the connection of a consistent concentrator does not change the resonant tuning of the converter. At the same time, the change in the level of its oscillations is determined by the ratio of the dissipative parameters of the converter, the concentrator and the load. From the relation (3) considering the formula (4) we find the amplitude of oscillations of the tool

$$a_l = a_0^* K\left[1 + V_{ll}(\omega) + \omega\beta(a_l)V_n^{-1}(\omega)K^2\right]^{-1}. \quad (5)$$

4 Exponential concentrator

Let's consider, skipping some transformations, a situation arising from the ultrasonic processing of fragile materials. In [4, 5] it is shown that the processing occurs as a result of high-frequency vibro-impact interactions of the tool with the workpiece during their compression by the static force *P*. There, on the basis of the rheological model of the cutting process, expressions for the elastic and dissipative components of the load were obtained:

$$k(a_l) = \frac{D}{\pi a_l}\sin\frac{2\pi P}{D};\ \beta(a_l) = \frac{2D}{\pi\omega a_l}\sin^2\frac{\pi P}{D}, \quad (6)$$

where D is a value proportional to the area of the tool and depends on the material of the product, as well as the type of abrasive slurry.

After substituting expressions (6) into the formulas of the previous section, we obtain, after transformations, a system of equations, the solution of which determines the parameters and amplitude of oscillations of the concentrator matched under the load:

$$a_l = \frac{2P}{M\omega^2 - U_{ll}(\omega)} \quad (7)$$

$$a_l = a_0^* K\left[1 - K\frac{\pi P^2}{DV_n(\omega)}\right]\left[1 + K^2\frac{V_{ll}(\omega)}{V_n(\omega)}\right]^{-1} \quad (8)$$

Below are the results of the calculation of one of the most common type of ultrasonic concentrator. The concentrator 1 (Fig.1) at its end connected to the output of the oscillation exciter 2.

Dynamic compliance of concentrators of various types are defined in [4, 5] by solving the equations of longitudinal vibrations of rods of variable cross section.

Consider an exponential concentrator, the area S_x of the cross section x of which varies according to the law $S_x = S_0\exp(2\gamma x/l)$, $\gamma = \frac{1}{2}\ln(S_l/S_0)$.

Expression for dynamic compliances of an exponential waveguide were obtained in [4, 5] and for the corresponding operator $L_{lx}(i\omega)$ has the form

$$L_{lx}(i\omega) = \frac{\gamma\,\mathrm{sh}\lambda x - \lambda l\,\mathrm{ch}\lambda x}{\omega^2\rho S_0 l\,\mathrm{sh}\lambda}e^{\gamma\left(1+\frac{x}{l}\right)}. \quad (9)$$

where $\lambda = \frac{\omega}{c}\left(i\frac{c^2}{c_{\text{тм}}^2} + \frac{\psi}{2\pi}\right)^{1/2}$; $c_\phi = \frac{c}{\sqrt{1-(\gamma c/l\omega)^2}}$ — phase velocity of sound in an exponential waveguide; $c = \sqrt{E/\rho}$ - sound velocity in the concentrator material; *E*, ρ – elastic modulus and density of the concentrator material.

Suppose that the absorption coefficient [7] ψ, which describes the energy loss in the material of the concentrator, is small. We will find the expression for the components of the dynamic rigidity of the exponential concentrator and then we obtain two equations that determine the desired solution. Let $\xi = \omega l c_\phi^{-1}$. Taking into account formula (9), by conducting a series of transformations, relation (3) for the gain of a loaded concentrator can be converted to the following form

$$K = \frac{a_l}{a_0} = \left|\frac{\gamma\cos\xi + \xi\sin\xi}{\xi}\right|\sqrt{\frac{S_0}{S_l}} \quad (10)$$

After calculations, you can also get:

$$a_l = \frac{2P}{\omega w_l}\left(\mu + \frac{\sqrt{1+(\gamma/\xi)^2}}{\cos\xi + (\gamma/\xi)\sin\xi}\right)^{-1} \quad (11)$$

where $\mu = M\omega/w_l$; $w_l = S_l\sqrt{E\rho}$ - at the output end of the concentrator.

The joint solution of equations (10) and (11) determines the desired values of ξ and a_l for an exponential concentrator that is matched under load. Here the amplitude value at the input end of the concentrator is set. This solution is convenient to perform numerically. The length of the concentrator is determined by the formula $l = c\omega(\xi^2 + \gamma^2)^{0,5}$. That in the absence of load ($\xi = \pi n$) coincides with that obtained in [3-5].

Fig. 2 shows the dependences of the length *l* of the concentrator, matched under load, on the compressive force *P* for different values of the mass of the tool *M*. Here l_0 — the length of the free unloaded concentrator, which is determined by $\xi = \pi n$. In the calculations it was assumed: the oscillation frequency $f = \omega/2\pi$ =20 kHz; *K*=4; $w_l = 3{,}14\cdot10^3$ N·s/m; ψ=0,01; *D*=5·10^4 N.

At Fig.2: 1 – μ=0; 2 –μ=0,2; 3 – μ=0,4; 4 – μ=0,6; 5 – μ=0,8; 6 – μ=1.

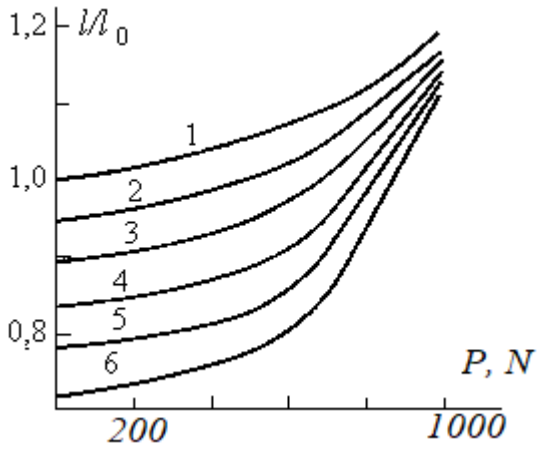


Fig. 2. *Concentrator length*

On this research problem cannot be completed. This is due to the fact that the connection of the concentrator affects the amplitude of the electroacoustic transducer. From the formula (8) it can be seen that the amplitude of oscillations at the output end of the concentrator depends on the ratio of dissipative losses in the converter and the concentrator.

Let, for definiteness, the transducer is a homogeneous rod of length l_n with a cross section S_n. Its dynamic stiffness tuning in resonance to the frequency of the first form of natural oscillations is given by the formula [4]: $V_n = 0,25\psi_n \omega w_n$, where $w_n = S_g\sqrt{E_n\rho_n}$ — wave resistance of the converter at the concentrator's connection point; E_n, ρ_n, ψ_n - elastic modulus, density and absorption coefficient of the converter material [7]. Joining even an unloaded (P = 0, M = 0) concentrator to a resonant vibration exciter changes its amplitude, which is found from the above formulas, so that

$$a_l^* = a_0^* K\left[1+\frac{\psi w_l K^2(1+\gamma^2/n^2\pi^2)}{\psi_n w_n}\right]^{-1}. \qquad (12)$$

From the last expression it is seen that the amplitude of oscillations of a concentrator with internal losses decreases in comparison with the ideal one. This decrease is the more significant, the greater the magnitude of these losses. The change in amplitude at the output of the hub depends on its gain coefficient K.

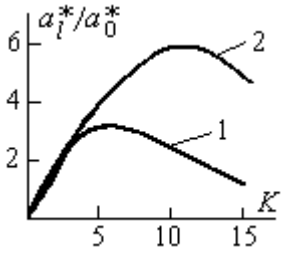


Fig. 3. *The oscillation amplitude of the end of the concentrator*

In Fig.3, formula (12) is used to build the dependence of the amplitude of oscillations of the free end of the exponential concentrator on the gain coefficient K (curve). Here $\psi_n w_a / \psi w_l = 65$. This shows that there is a gain coefficient K value at which the amplitude of oscillation of the output end of the concentrator is maximum.

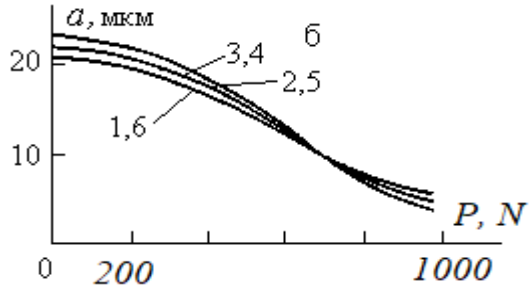


Fig. 4. *The dependence of the amplitude on the compressive force.*

In Fig.4, the dependences of the amplitude of oscillations of an exponential concentrator matched under load on the compressive force for various tool weights are plotted. The graphs are plotted with the same parameters as Fig.2. It was selected ω_n=4,084·10^4 N·s/m; ψ_n=0,05.

Research models of other types of concentrators is performed similarly. For example, curve 2 in Fig.3 corresponds to a step type concentrator consisting of two cylindrical bars [4, 5]. The corresponding calculation is not given here.

5 Conclusions

The analysis of concentrator models in ultrasonic technological machines and devices is reduced to the study of the features of longitudinal oscillations of rods with variable cross sections. Such rods function in the presence of an elastic-dissipative load, as well as several additional factors. At the same time, it is necessary to take into account the dissipative properties of the material of the concentrator itself. As a result, the studied models turn out to be essentially nonlinear. Their research and description can be performed using frequency methods based on ideas of equivalent linearization. These methods allow us to give an interpretation of the main dynamic effects, manifested in concentrators of different types.

The paper was supported by the Russian Science Foundation (project # 18-08-00168).

References

1. L. Merkulov *Acustical journal* **3**, 3 (1957)
2. L. Merkulov, A. Kharitonov *Acustical journal* **5,** 2 (1959)
3. I. Teumin *Ultrasonic oscillating systems* (Machgiz, Moscow, 1959)
4. V. Astashev, V. Babitsky *Ultrasonic Proocesses and Machines* (Springer, 2007)
5. V. Astashev, V. Krupenin *Non- linear Dynamics of Ultrasonic Technological Processes* (MGUP im Ivana Fedorova, Moscow, 2016)
6. L. Rozenberg, V. Kazantsev *Machine-tools and tools* 5 (1959)
7. E. Sorokin *To the theory of internal friction in the oscillation of elastic systems* (Gosstroiizdat, Moscow, 1966)

SYSTEM FOR PROCESSING CONCENTRATED AND NON-CONDENSING GASES IN BOILERS

Ch. Assistant Dr. Eng. Madzharova St.[1], Assoc. Prof. Dr. Petrova T.[2], Prof. Dr. Eng. Bozukov N.[1]
University of Food Technologies, Plovdiv, Bulgaria[1]
Institute for Food Research and Development - Plovdiv, Bulgaria[2]

nitani@abv.bg

Abstract: *A heat regeneration system is presented for the emptying of the lime boilers in a normally conventional lime-room to reduce the sulphur gases emitted from the blowing tank. The vapor passes through the pipes from the blowing tank to the blowing condensate reservoir for regeneration of valuable secondary heat. Non-condensing gases are discharged from the blowing condensate tank to the gas cooler and then additionally for combustion. The condenser formed in the heat recovery condenser is led to the sewer. Heat recovery system for the emptying of the lime boilers reduces both gas emissions and energy costs.*

KEYWORDS: *CONCENTRATED AND NON-CONDENSING GASES, HEAT REGENERATION, STEAM*

1. Introduction

The object of the examination is a pulp mill, in which there is a conventional conventional boiler room consisting of six boiler boilers blowing to one blow tank. Sulfur gas contributes to the bad odor (stench) in the surrounding environment if it is not regenerated. This sulfur is oxidized and contributes to acid rain [1]= A large amount of valuable heat is regenerated from the vapor. Heat is used to produce large amounts of hot water, which reduces or eliminates the use of steam for heating liquids when flushing or bleaching. The steam passes through the pipes from the blow tank to the blow-off condensate reservoir to regenerate valuable secondary heat. Non-condensing gases are taken from the blow-off condensate tank to the gas cooler and then further incinerated. The condensate formed in the heat recovery condenser is drawn to the sewer.

There are three main outlets for concentrated non-condensing gases in a sulphate cellulose plant:

1. Gases from the steam condenser in the boiler department.
2. Gases from the pit of the vacuum boxes in the Evaporative Station.
3. Gases from the treatment of contaminated condensate.

The characteristic smell originates from the volatile sulfur compounds that are produced during digestion. Sulfide ions (HS^-) react with lignin during digestion, leading to the four most observed smell compounds. These are hydrogen sulphide (H_2S), methyl mercaptan (CH_3SH), dimethyl sulphide (CH_3SCH_3) and dimethyl disulfide (CH_3SSCH_3). Other hazardous compounds that are produced during cooking are methanol (CH_3OH) and turpentine. The common properties of these gases are: hazard, toxicity, smell bad and colorless. The amount of gas produced depends on the boiling conditions and the raw material. High sulphide, low Karra number, long boiling time and high boiling liquor temperature lead to increased sulfur emissions.

2. Description of the process

The boiling process is carried out in six boiler boilers by heating pine chips in an aqueous solution containing sodium hydroxide (NaOH) and sodium sulfide (Na_2S). The content of the boiler boiler is released to the blow tank by opening the blowing valve. A large amount of steam is formed in the blow tank when the hot mixture of lye and pulp flare. Pulp and black liquor are separated from blowing vapor and concentrated noncondensing gases. The pulp and black liquor are removed from the bottom of the flushing tank in the flushing system. The vapor and gas are removed from the top of the blow tank and taken to the steam condenser where the steam energy is regenerated [2].

The vapor condenser condenses much of the vapor that leaves the blow tank.

The energy is regenerated from circulating hot water through the steam condenser. In each blow, hot water is pumped into the recirculation system, producing the same amount of hot water. Condensate from the steam condenser is pumped to sewerage in the evaporation zone.

The gas and steam which do not condense in the vapor condenser are fed to the gas cooler where the residual vapor condenses at the same time as the gas is cooled to a suitable temperature (~ 50° C). Concentrated non-condensing gases from the gas cooler are fed to the collector tank.

The cooling fluid during this process is soft water. If fresh water is used instead of soft water in the heat recovery condenser when the boilers are emptied, there is a risk of precipitation of CaCO3 on the heating surfaces. The condensate from the gas cooling process is returned back to the main condensate stream from the steam condenser.

Concentrated non-condensing gases from the heat recovery system when emptying boiler boilers are above the upper explosion limit and it is important that they remain above the boundary and not be diluted.

In the burner for concentrated non-condensing gases, natural gas is used in the ignition flame. Natural gas is also used as an auxiliary fuel in the soda-regeneration boiler.

The concentrated non-concentrating gas pipeline is equipped with double shut-off valves and a ventilation valve as well as a protective membrane and flame retardant located near the incineration point. If the combustion in one source stops for some reason, the double shut-off valves are automatically closed and the drain valve opens. The combustion of concentrated non-condensing gases then switches automatically to the available incineration sites as described below in the section on combustion of concentrated noncondensing gases.

If the protective membrane is broken, the temperature indicator after it will include the signaling. The pressure in the condensed noncondensing gas pipeline is controlled by adjusting the position of the conveying tube of concentrated non-condensing gases in the burner or by the low-pressure steam that is fed to the line if the pressure becomes too low and the pipe is in the final position.

All necessary equipment is connected to an emergency power supply.

The entire condensate from the concentrated non-condensing gases is collected to the pumping tanks and pumped into the sewer, which is in the evaporation zone.

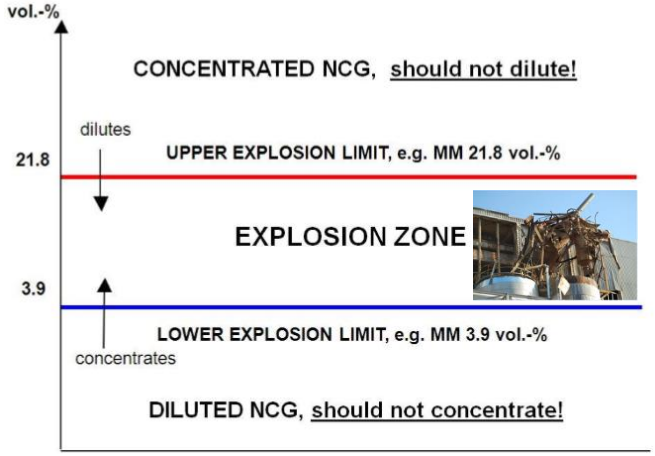


Fig. 1. *Explosive limits of non-condensing gases*

3. Heat Regeneration System for Vacuum Boilers Emptying

Various boilers are discharged to the existing vent tank, the pressure of which is set to 1.0 bar. The evaporating mixture of hot lye / pulp releases a large amount of steam, which is directed to a blowing condensate reservoir.

The blowing steam flow is calculated from the boiler boiler data according to Table 1. The blowing vapor flow is shown as a diagram in Diagram 2.

Table 1. *Data for boiler boiler feed in the plant for production of cellulose*

	Today	Future	
design power	272	386	adt/24h
number of blowouts /24h	27	38	
boiler volume	110	110	m³
moisture of wood	50	50	%
wood temperature	30	30	°C
damp wood	45	45	t
dry wood	19,3	19,3	t
output	48	48	%
boiler output	10	10	adt
active base of white liquor	128	128	kgNaOH/adt
liquor /wood	4,2	4,2	t/t
white liquor	33	33	m³
black liquor temperature	80	80	°C
steam release	1860	1860	kg/adt
boiling temperature	170	170	°C
duration of blowing	17	17	min

The pressure in the blow tank is used as an input to the pressure regulator that determines the velocity of the soft water pump. The higher the pressure, the higher the pump speed. Cooling water at about 40 ° C from existing soft water tanks is pumped to the suction of the cooling water recycling pump. The purpose of the regulator is to reduce the delay time in the blasting condensate tank, which leads to better control of the pressure of the blow tank. The hot cooling water is discharged to the existing battery that will be used as a clean water storage.

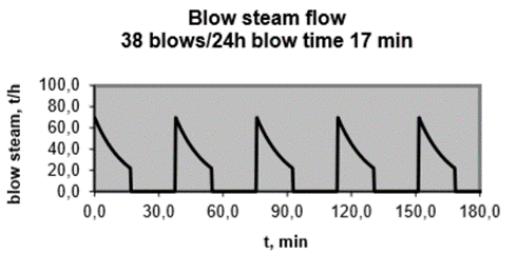


Fig. 2. *Typical flow of boiling vapor from boiler boilers, calculated from the heat balance and blowing time of the boiler*

The blowing vapor streams and the corresponding cooling / hot water streams are calculated for pulp production capacities corresponding to 27 ... 38 puffs / 24h. Soft water from a tank is used as cooling water in the blowing condensate tank, the produced hot water is pumped to the hot water tank. The bleeding tank is tightly closed (under pressure). The pressure in the tank will usually vary between - 5 kPa (g) ... 20 kPa (g). The tank is equipped with safety devices for high pressure and low pressure situations. Such a situation can occur, for example, if the cooling water pumps and / or do not work.

Table 2. *Heat production when emptying boiler boilers and secondary heat.*

	Today	Future	
steam to blowdown tank, normal	13,0	18,0	t/h
steam to blow tank, max	69,0	69,0	t/h
discharge to a bleeding tank	1,4	2,0	t/h
warm water temperature	45	45	°C
flow of warm water	194	273	t/h
hot water temperature	85	85	0C
hot water flow	194	273	t/h

The bladder tank has dual high-pressure protection. The regulator will open a valve and excess steam blows into the atmosphere. If the regulator fails, a protective membrane protects the tank and the steam is blown into the atmosphere. The bursting pressure on the membrane is 1 bar.

The reservoir is protected against low pressure with a mechanical safety valve that opens at -10 kPa. It is important to avoid leakage of air to the blow tank between blows. The entrained air is an inert gas that will reduce the performance of the blowing condensate reservoir and will also disrupt the operation of combustion systems of concentrated noncondensing gases in the water intake pipes, and the mixture of concentrated non-condensing gases and air is highly explosive. The basic low pressure protection is a sealing vapor that is regulated by a regulator. The regulator will add backing steam to the blow tank at low underpressure. At even lower pressure, a regulator will open, and then the mechanical safety valve, the ejection of the reservoir.

The contaminated condensate is collected at the bottom of the blowing condensate tank. Condensate is pumped with a level regulator to the sewer pipe located in the evaporation zone.

The conductivity of the condensate is measured. If the conductivity level is above the setpoint, the condensate returns to the equalization tank.

Non-condensing gases, from the blowing condensate tank, are directed to the gas cooler. The purpose of the cooler is to reduce the water pressure in the system, thereby reducing the volume of gas. The softened water is used as a cooling liquid. The water is added to the temperature control device The hot water produced is taken to the hot water tank by means of a blowing condensate tank. The contaminated condensate from the cooler drains through a seal to the blowing condensate reservoir and then pumped to the evacuation zone sewer pipe.

The pressure regulator is mounted between the blow-off condensate tank and the gas cooler. The purpose of this regulator is to protect the system of concentrated non-condensing gases from excessive suction.

Evaporation vapor condensation

The blowing valve under each boiler boiler is left open when the boiling time is reached. The valves are programmed to open gradually to reduce the impact of the system pressure during blowing. The pulp, the steam, the black liquor and the gas are fed to the blower by the boiler pressure. The steam and gas are fed to the steam blowing condenser The pressure in the purge tube between the blow tank and

the steam condenser is maintained by adjusting the speed of the pump for softened water when the pressure is increased. If the pressure drops, the low pressure steam is taken to the system to maintain normal operating conditions. To increase overall safety during each blowout, the bladder tank is equipped with an overpressure protective membrane along with a mechanical vacuum safety valve.

Heat Regeneration System

The main part of condensation from the steam blowing is in the steam condenser, the main condenser. The circulation of the steam condenser cooler, the softened water, is maintained by a pump. Hot water is pumped from the softened water tank with a pump by adjusting the pump speed. The pressure regulator controls the speed of the pump. High pressure results in a higher spin speed. The energy that is released when condensing vapor condenses goes to the circulating hot water. The temperature of the resulting hot water is between 80-100°C when the hot water is taken to the hot water tank. The level controller controls the condensate level in the steam condenser. Emergency low level blocks a pump, the high level restarts the pump, and the emergency level high opens the valve. Uncondensed blowing vapor and non-condensing gases are fed to a gas cooler. The gas flow is controlled by a pressure regulator, and a valve balances the pressure fluctuation during each blow (the set point is between -3 - 0 kPa). The outside temperature of the gas cooler controls the amount of cooling water needed. When the cooling water temperature (about 40°C) has reached a temperature of about 50°C, the valve is set to an open position. In this way, cold water flows into the system at the same time as the hot coolant is pushed into the steam cycle of the steam condenser. The resulting condenser from the gas cooler is fed to the suction side of a pump.

Collector and air conditioning system

Concentrated non-condensing gases from the pre-treatment compartment are collected in a reservoir with a hydraulic lock / collecting tank for the CNG . The sum is taken up in the water jet for the CNG under the surface of the liquid to avoid backflow. The CNG is then sent to the CNG condenser to reduce moisture [3].

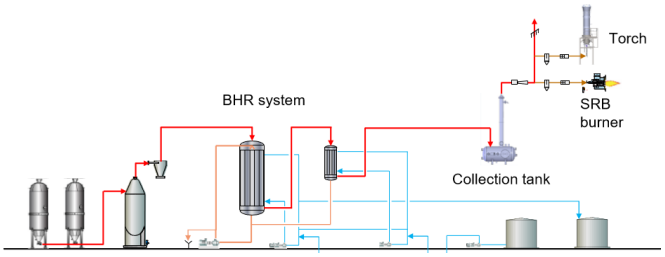


Fig. 3. *Simplified pipeline process for condensed non-condensing gases - collector and air conditioning*

Transfer of concentrated noncondensing gases

There is an ejector for transporting concentrated non-condensing gases from the bulk tank to the available incineration site. The ejector is located in the building of the soda regeneration boiler and is used when combustion of the concentrated noncondensing gases is carried out.

4. Conclusion

The construction of the heat recovery system when emptying the boiler boilers reduces the debilitating gases emitted from the blow tank. Non-condensing gases are removed and further incinerated. A system of heat recovery when emptying boilers generates financial gains associated with energy costs and reduced emissions of greenhouse gases.

5. References

[1] Василев П., П. Петров., П. Минчев., С. Табаков. Производство на целулоза, Хартия и Картони част I и II. София, Техника, 1964.

[2] Kirwan Mark J. Handbook of Paper and Paperboard Packaging Technology, New York, United States, John Wiley & Sons Inc, 2013.

[3] https://www.valmet.com/

STATISTICAL ANALYSIS OF LOCOMOTIVES TRACTION MOTORS PERFORMANCE

Oleksander Gorobchenko[1], Victor Tkachenko[1*]
[1]State University of Infrastructure and Technologies, Department of Traction Railway rolling stock, Kyiv, Ukraine

Abstract. *In this article the authors quoted results of traction motors speed performance variations statistical analysis and wage wheels bands diameters deviations according to operation data. The authors of this publication offered the method of determining the non-uniformities of current distribution in the power circuit of the locomotive, based on probabilistic approach, and also performed its comparison with classic computation approach. The next statistical performance of the continuous current locomotives traction drive is as follows: mathematical expectation of the motors magnetic flux; mean square deviation of magnetic flux; statistical dispersion and average square deviation of wage wheels bands diameters. With help of the received data it became possible to improve determination of non-uniformities currents deviations on traction motors during loading of the electric locomotives*.

1 Introduction

As operation experience says, efficiency of the locomotives work can be significantly increased provided that we use trailing weight, power of traction electric drives to a fuller extent and improve the traction electric drives control systems [1,2] .

The existing diagrams and control algorithms do not allow to implement potentialities of traction rolling stock concerning using of trailing weight and power of electric drives completely. One of the main reasons is non-uniformity of using the power of the drives.

The main method to improve performance of the locomotives is to develop devices for the locomotive traction control system altogether and for each wage wheels individually [3, 4]. Most of the locomotives, used at the railways of post-Soviet countries, are equipped with classic control systems [5, 6], which do not provide control of load reallocation on axes. So determination and elimination of factors, which have an impact on inequality of the current distribution at the power circuits of the locomotives is a currently central issue. When we solve this issue, it will allow us to improve traction output performance of the existing rolling stock.

2 Problem discussion

The purpose of this work is to obtain statistical values of traction electric transmission parameters distribution. This will allow to justify the methods of eliminating the non-uniformities of current distribution at the power circuits of the locomotive wage wheels drive in a more qualitative manner.

We found that the crucial influence on current distribution at the power circuits is caused by such factors as velocity performance of traction electric motors, surfaces wheels rolling wage wheels diameters, resistance of the electric motors electric coils [7–9].

There is a small probability that in one locomotive at the parallel paths we find the motors with extreme deviations of velocity performance [10]. In this case we will have disadvantageous combination of them with wage wheels.

We need to use the data which are closer to reality when we forecast tendency to non-uniform current distribution of the locomotives. According to results of calculations we can conclude that using of special devices to flatten the currents for particular brands of the locomotives is rational.

3 Analysis of traction drives velocity performance variations according to operation data

To analyze velocity performance of traction motors we made a data retrieval from tests reports of electric locomotive continuous current traction electric motors with voltage in the contact system 3000 V. We analyzed 428 motors. We analyzed performances of the motors during clockwise and anticlockwise rotation. The results of statistical analysis are on Fig. 1 and 2. We measure frequency of the motors rotation during rated one hour's duration current, which is 380 A.

Average rotation frequency

$$\overline{n}_m = \frac{1}{z}\sum_{i=1}^{k} N_i z_i \qquad (1)$$

where z_i is a number of motors in i-type rotation frequency interval;

z – general number of motors

k – number of intervals;

$\boldsymbol{N_i}$ – number of motors, which are classified to interval by test results.

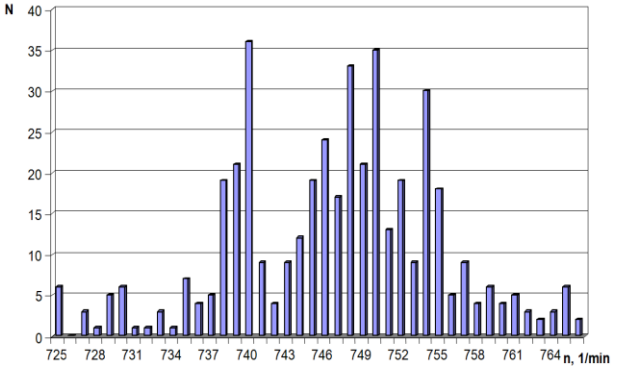


Fig. 1. *Distribution of number of the motors on rotation frequencies during clockwise rotation –* $\overline{n}_{mr}$

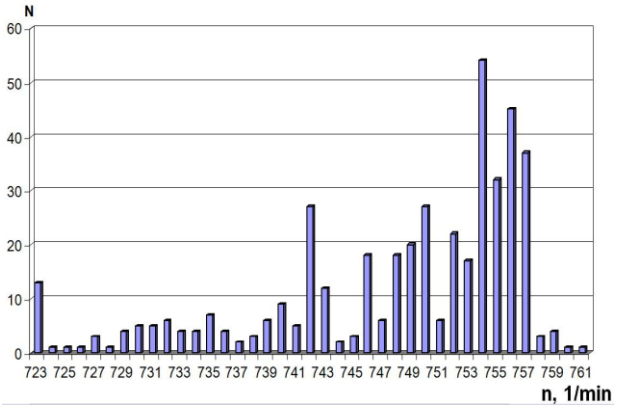


Fig. 2. *Distribution of number of the motors on rotation frequencies during anticlockwise rotation –* $\overline{n}_{ml}$

Analysis results: $\overline{n}_{mr}$ = 746,8 rpm; $\overline{n}_{ml}$ = 748 rpm; $\overline{n}_m$ = 747,45 rpm.

Therefore, average motors rotation frequency in operation is exaggerated comparing to rated one (735 rpm).

Rotations frequency dispersion:

$$D^*_n = \frac{1}{z}\sum_{i=1}^{k}(N_i - \overline{n}_{cp})^2 z\,. \qquad (2)$$

* Corresponding author: v.p.tkachenko.detut@gmail.com

When we put in the data on rotation frequencies, we will obtain for clockwise rotation of traction electric motors D^*_{nmr}=67,15, for anticlockwise rotation of traction electric motors – D^*_{nml}=81,15.

Statistical average square deviation of rotation frequencies by formula

$$\sigma^*_n = \sqrt{D^*_n} \; .. \qquad (3)$$

During calculation we obtain (for clockwise and left side anticlockwise rotation):

σ^*_{nmr} = 8,19;

σ^*_{nml} = 9.

Due to the fact that difference of velocity performance of only one locomotive influences non-uniformity of current distribution, we processed statistical data concerning ultimate difference of rotation frequencies within one locomotive. As a result we obtained the following set of data, which are shown as histogram on Fig.3 and 4.

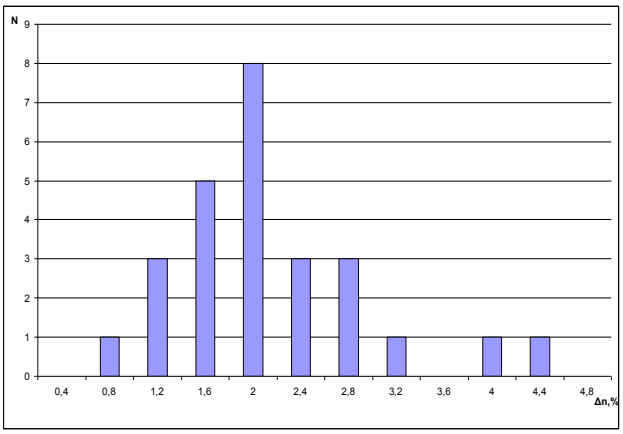


Fig. 3. *Distribution of deviations in difference of the velocity performances within one locomotive during clockwise rotation of the traction electric motors*

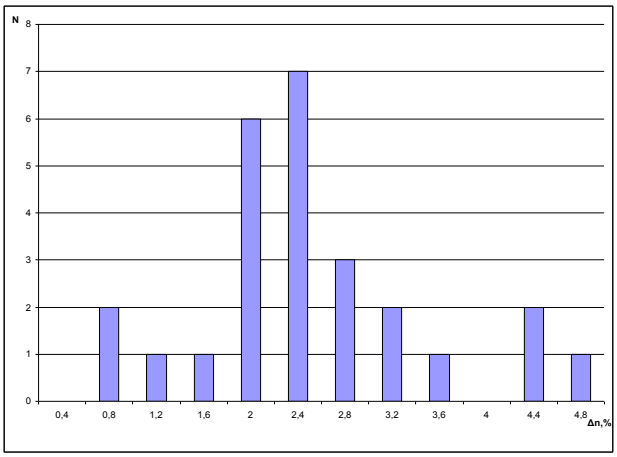


Fig. 4. *Distribution of deviations in difference of the velocity performances within one locomotive during anticlockwise rotation of the traction electric motors*

On the ground of the statistical data processing we obtained the following results:

- average deviation of performances within one locomotive:

- during clockwise rotation of the traction electric motors – Δn = 2,13%;

- during anticlockwise rotation of the traction electric motors – Δn = 2,5%;

- statistical dispersion: $D^*_{n\%r}$=0,664, $D^*_{n\%l}$=0,955;
- average square deviation $\sigma^*_{n\%r}$=0,815, $\sigma^*_{n\%l}$=0,977.

4 Statistical analysis of locomotives rolling wheel surfaces diameters deviations according to operation data

In order to consider impact of locomotives rolling wheel surfaces diameters spread on non-uniformity of the current distribution between the traction electric motors we conducted research of the continuous current electric locomotive fleet, which are operated on Ukrzaliznytsia – Ukrainian railway, namely 40 locomotives of ВЛ18 series. As a result we obtained statistical data, shown on Fig.5.

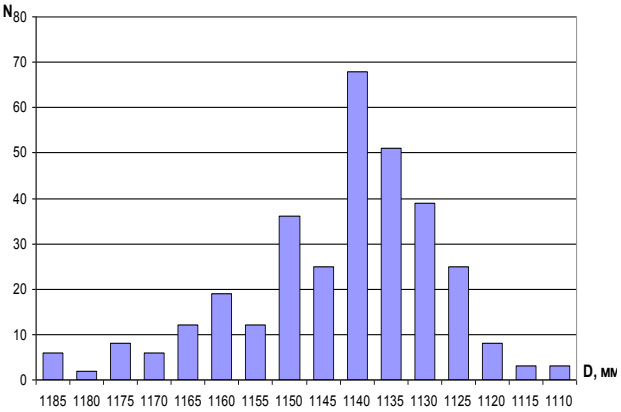


Fig. 5. *Distribution of wage wheels on locomotives wage wheels diameters on wage wheels surfaces diameters*

Average value of bands diameters D is calculated using the formula

$$\overline{D} = \frac{1}{n}\sum_{i=1}^{k} D_i n_i \; , \qquad (4)$$

where n is general number of wheels;

k – number of intervals;

D_i – average interval value of wheels diameters;

n_i – number of wage wheels, classified to interval according to results of measurements.

Dispersion of wheels diameters D_D are found using the formula:

$$D^*_D = \frac{1}{n}\sum_{i=1}^{k} (D_i - \overline{D})^2 n_i \; . \qquad (5)$$

Statistical average square deviation of wheels diameters is found using the formula $\sigma^*_D = \sqrt{D^*_D}$.

We obtained the following performances:

- average value of wheels diameters: $\overline{D}$ = 1142 mm;
- dispersion of wheels diameters: D_D = 214 mm;
- statistical average square deviation of wheels diameters – σ_D =14,63.

The crucial thing is that spread of wheels diameters within one section of he locomotive has an impact on non-uniformity of current distribution. We presented the obtained results on Fig. 6.

On the ground of processing of the selected material we obtained the following results:

- average value of ultimate difference of diameters ΔD = 13,9 mm;
- statistical dispersion D_D = 14,95 ;
- statistical average square deviation σ_D =3,87.

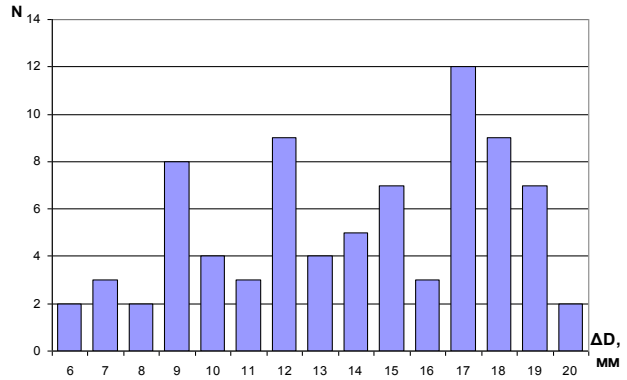


Fig. 6. *Distribution of e locomotives on difference of wheels rolling surfaces diameters within on section of the locomotive*

5 Correlation of the current distribution non-uniformities, calculated on limiting and probabilistic laws

Magnetic flux of i-type drive Φ_i is a normal random variable, [11]

$$f_1(\Phi_i)=\frac{1}{\sigma_1\sqrt{2\pi}}e^{\frac{-(x-m_1)}{2\sigma_1^2}}, \quad (6)$$

where m_1 is a moral expectation Φ_i;

σ_1 – average square deviation Φ_i;

Also there is the other normal random variable – wheels rolling surfaces diameters D_b

$$f_1(D_b)=\frac{1}{\sigma_2\sqrt{2\pi}}e^{\frac{-(y-m_2)}{2\sigma_2^2}}, \quad (7)$$

where m_2 is a moral expectation D_b;

σ_2 - average square deviation D_b.

It is natural to suppose that random variables – magnetic flux and bands diameters – are independent. In this case density of random variables system distribution Φ_i and D_b looks like $f(\Phi_i, D_b)=f_1(\Phi_i)f_2(D_b)$.

Spheres S (Fig. 7), in which there will be parameters Φ_i and D_b with probability γ, is found by means of calculating the integral

$$\gamma=\iint\limits_S f(x,y)dxdy=\iint\limits_S f_1(\Phi_i)f_2(D_b)d\Phi_i dD_b=$$

$$=\int\limits_{a_1}^{b_1} f_1(\Phi_i)d\Phi_i\int\limits_{a_2}^{b_2} f_2(D_b)dD_b, \quad (8)$$

where a_1,b_1,a_2,b_2 – are limits of the sphere of change of parameter Φ_i and Db.

It is natural to choose the intervals, situated symmetrically towards moral expectation of the random variable.

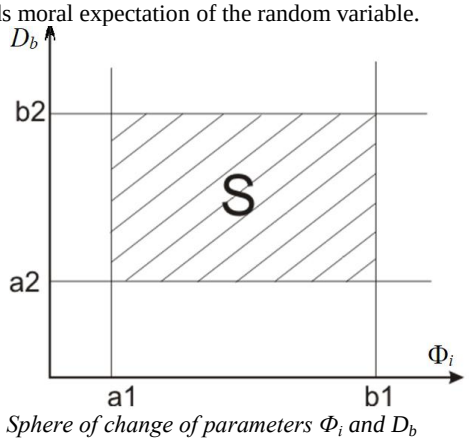


Fig. 7. *Sphere of change of parameters Φ_i and D_b*

As we can see from the Fig. 8 and 9, for the random variable Φ_i we can choose the intervals [m1-c1; m1+c1], ad for the random variable D_b – interval [m2-c2; m2+c2].

Probabilities of penetration of the random variables Φ_i and D_b into the considered intervals are calculated using the following formulas:

$$P_1=P(m_1-c_1<\Phi_i<m_1+c_1)=P(|\Phi_i-m_1|<c_1)=2F(\frac{c_1}{\sigma_1}) \quad (9)$$

$$P_2=P(m_2-c_2<D_b<m_2+c_2)=P(|D_b-m_2|<c_2)=2F(\frac{c_2}{\sigma_2}) \quad (10)$$

where $F(x)=\frac{1}{2\pi}\int\limits_0^x e^{-\frac{t^2}{2}}dt$ is a Laplace integral.

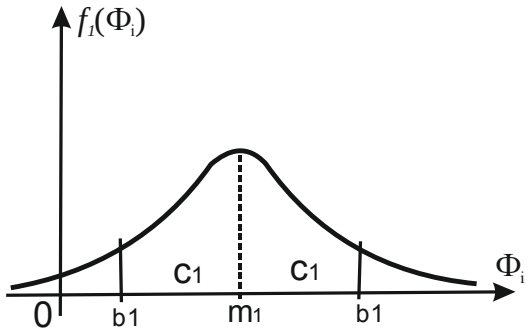


Fig. 8. *Curvature of distribution density for the magnetic flux*

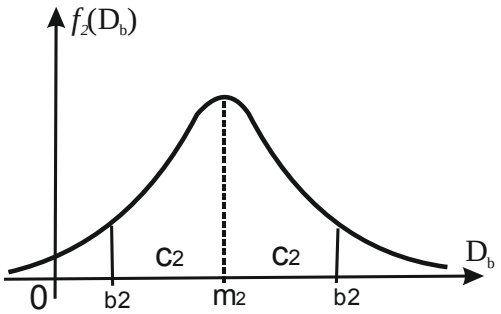


Fig. 9. *Curvature of the wheels diameters density*

The function $F(x)$ is a tabulated function. The tables of its values are known from [11].

The variables c_1 and c_2 are chosen provided that

$$P_1P_2=4F\left(\frac{c_1}{\sigma_1}\right)F\left(\frac{c_1}{\sigma_1}\right)\geq\gamma, \quad (11)$$

where γ is chosen, coming from engineering and operation conditions.

In rated static mode the current of the traction electric motor is determined using the known formula

$$I=\frac{U-c_E n\Phi}{R}, \quad (12)$$

where U is voltage put to the motor, V;

c_E is a constant by electromotance;

n is a frequency of the motor rotation, rpm;

Φ – magnetic flux, Wb;

R – equivalent motor resistance, Ohm.

Increase of the current is described by the following dependence

$$\Delta I=\frac{\partial I}{\partial n}\Delta n+\frac{\partial I}{\partial \Phi}\Delta\Phi, \quad (13)$$

where $\frac{\partial I}{\partial n}=-\frac{C_E\Phi}{R}$; $\frac{\partial I}{\partial \Phi}=-\frac{C_E n}{R}$.

Altogether we obtain

$$\Delta I=-\frac{C_E}{R}(\Phi\Delta n+n\Delta\Phi). \quad (14)$$

For the simple reason that $n = \frac{60iV}{3.6\pi D_b}$ and $\Delta n = \frac{60iV}{3.6\pi D^2_b}\Delta D_b$ we have

$$\Delta I = -\frac{60C_E iV}{3.6\pi RD_b}\left(\frac{\Phi}{D_b}\Delta D - \Delta\Phi\right), \quad (15)$$

where i is a reduction ratio of thrust actuator;

V – a vehicle unit velocity, km/h.

6 Conclusions

We determined how difference between traction electric motors and diameters of the locomotives wheels impacts on distribution of currents in electric locomotives drive power circuits. We developed the method of calculating parameters of current distribution and took into account allowances on traction electric motors and practical deviations of their performances during operation. The proposed method gives us the opportunity to evaluate non-uniformity of traction electric motor current distribution in broad limits of engineering and operation allowances.

In accordance with statistical data for continuous current electric locomotives we obtained the following variables: moral expectation of the motors magnetic flux m_1=0,146 Wb, average square deviation of magnetic flux $\sigma_1=7\cdot10^{-4}$ Wb,. For moral expectation of the bands diameters we determined m_2 =1142 mm and average square deviation of the bands diameters σ_2=9,92 mm.

According to statistical analysis probability γ =0,9 will allow the magnetic flux of the motors to change in the interval (0,14162–0,15038)Wb, and bands diameters – in the interval (1131,7–1152,4) mm. For example, for the electric locomotive ДЕ1 non-uniformity of the current distribution in one hour's mode is 32A. The obtained results tell us that the current distribution calculated on the set probabilistic distributions, gets closer to the one obtained thanks to calculations, performed with using maximum allowance.

The results of the presented analysis tell us about availability and degree of tendency of the traction electric motors to overload within one locomotive. It is necessary to take into consideration during repair of the electric locomotives during establishing wheels and motors unit in the bogie frames. The given results it is necessary to take into consideration during setting of the clutch controlling systems and protection of the wage wheels from boxing. When we implement this proposal it will give us the opportunity to improve the traction properties of the locomotives, reduce the expenditures of power on traction and to enhance reliability of capacity value transmission.

References

1. Shamardina, V. N., Anishchenko, M. V., Lemeshko, S. M., & Kanunnikov, R. V. (2017). Functional efficiency enhancement of diesel-electric locomotive traction system. *Modern Electrical and Energy Systems (MEES), International Conference on* (20-23). IEEE.
2. Mikhailov, E., Semenov, S., Tkachenko, V., & Sapronova, S. (2018). Reduction of Kinematic Resistance To Movement Of the Railway Vehicles. In *MATEC Web of Conferences* (Vol. 235, p. 00033). EDP Sciences. Vol. 235. EDP Sciences, 2018. (doi : 10.1051/matecconf/201823500033).
3. Spiryagin, M., Wolfs, P., Szanto, F., & Cole, C. (2015). Simplified and advanced modelling of traction control systems of heavy-haul locomotives. *Vehicle System Dynamics*. 53(5), 672-691.
4. Ishrat, T., Ledwich, G., Vilathgamuwa, M., & Borghesani, P. (2016). Wheel slip control based on traction force estimaton of electric locomotives. *Power Engineering Conference (AUPEC), Australasian Universities* (1-6). IEEE.
5. Hill, R. J. (1994). Electric railway traction. I. Electric traction and DC traction motor drives. *Power Engineering Journal*. 8(1), 47-56.
6. Nategl, S., Lindberg, D., Aglen, O., Brammer, R., & Boglietti, A. (2018). Review and Trends in Traction Motor Design: Electromagnetic and Cooling System Layouts. *XIII International Conference on Electrical Machines* (ICEM) (2600-2606). IEEE.
7. Gorobchenko, O., Fomin, O., Fomin, V., & Kovalenko, V. (2018). Study of the influence of electric transmission parameters on the efficiency of freight rolling stock of direct current. *Восточно-Европейский журнал передовых технологий*, 1(3), 60-67.
8. Горобченко, А. Н. (2006). Методика расчета токов в силовой цепи электровоза. *Collection of scientific papers of the Donetsk Institute of Railway Transport*. 5, 119-128.
9. Горобченко, О. М., Кривошея, Ю. В., & Гатченко, В. О. (2008). Розробка комплексної математичної моделі силового кола електровоза з використанням програмного пакету Matlab. *Collection of scientific papers of the Donetsk Institute of Railway Transport*. 13, 86-96.
10. Steimel, A. (2008). Electric traction-motive power and energy supply: Basics and practical experience. *Oldenbourg Industrieverlag*.
11. Gnedenko, B. V. (2017). Theory of probability. *Routledge*.

EXERGY ANALYSIS OF WET COOLING TOWER AT VARIOUS LOADS AND AMBIENT TEMPERATURES

PhD. Mrzljak Vedran[1], PhD. Orović Josip[2], PhD. Poljak Igor[2], PhD Student Eng. Kocijel Lino[1]
[1]Faculty of Engineering, University of Rijeka, Vukovarska 58, 51000 Rijeka, Croatia
[2]University of Zadar, Maritime Department, M. Pavlinovića 1, 23000 Zadar, Croatia
E-mail: vedran.mrzljak@riteh.hr, jorovic@unizd.hr, ipoljak1@unizd.hr, lkocijel@gmail.com

Abstract: *This paper presents an exergy analysis of wet cooling tower at three different loads and in a range of the ambient temperatures. Increase in cooling tower load increases its exergy destruction and simultaneously decreases cooling tower exergy efficiency, while an increase in the ambient temperature causes a decrease in cooling tower exergy destruction and simultaneously decreases its exergy efficiency. The lowest cooling tower exergy destructions (between 1417.54 kW and 2925.65 kW) are obtained at low load. The highest cooling tower exergy efficiencies are calculated at the lowest observed ambient temperature of 5 °C - they amount 64.31 % at low load, 54.80 % at middle load and 53.94 % at high load. The change in ambient temperature for 5 °C resulted with a change in cooling tower exergy efficiency of 4 % or more on average.*

KEYWORDS: EXERGY ANALYSIS, WET COOLING TOWER, VARIOUS LOADS, CHANGE IN AMBIENT TEMPERATURE

1. Introduction

Steam condenser is one of the essential elements of any steam power plant [1]. Its operation significantly influences steam turbine and steam expansion process through the turbine. For adequate steam condensation in the condenser a proper cooling medium is required, which is, in most cases, water [2] (or in some situations air [3]).

Cooling water which passes through the condenser tubes (in the most used water cooled steam condensers) must be cooled and returned back to condenser (with decreased temperature) so that it could take the heat from steam again.

Cooling of water which takes heat from the steam in steam condenser can be performed in several ways. It can be used wet or dry cooling tower with natural air circulation or with air circulation caused by fans (forced air circulation). In the cooling towers in general, the ambient air is used for cooling the water, which is delivered from steam condenser or more of them [4].

This paper presents an exergy analysis of wet cooling tower with natural air circulation from cogeneration power plant. Exergy analysis is performed at three cooling tower loads and in a range of ambient temperatures. Calculations show that the highest cooling tower exergy efficiencies and the lowest exergy power losses will be obtained at low cooling tower load. Cooling tower has the lowest exergy power losses at the highest observed ambient temperature, while the highest cooling tower exergy efficiencies are obtained for the lowest observed ambient temperature.

2. Description and operating characteristics of the analyzed wet cooling tower

General scheme of the analyzed wet cooling tower along with marked operating points of each fluid flow stream (water and air) necessary for the exergy analysis is presented in Fig. 1.

Wet cooling towers operate on the principle of evaporative cooling. The hot water flow stream from the steam condenser is sprayed into the air flow stream (operating point 2, Fig. 1), which allows both sensible and latent heat transfer. In such cooling towers the water flow stream is cooled to near the wet-bulb temperature of air. Such heat transfer makes wet cooling tower more efficient (when compared to dry cooling towers).

Analyzed wet cooling tower has natural air circulation. Therefore, air fans for increasing air velocity (and thus improving heat transfer between water and air) are not used.

Inside the cooling tower, the flow arrangement between air and water flow streams can be crossflow, counterflow and parallelflow. Cooling towers with counterflow arrangement, as the one analyzed in this paper, where the air flow is opposite to the water flow, in general achieves the best efficiencies during its operation.

As presented in Fig. 1, cooled water is collected in a water pool at the cooling tower bottom and delivered again (by a pump) into the steam condenser.

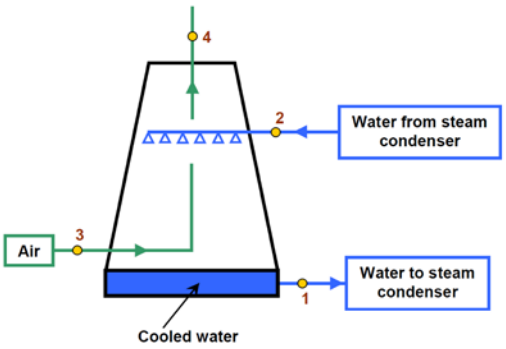


Fig. 1. *Cooling tower scheme with marked operating points necessary for the analysis*

3. Exergy analysis equations

3.1. General exergy analysis equations valid for any volume or system

The second law of thermodynamics defines exergy analysis of a system or volume, [5] and [6]. For a volume or system in steady state, the main exergy balance equation can be defined as [7]:

$$\dot{X}_{\text{heat}} - P = \sum \dot{m}_{\text{OUT}} \cdot \varepsilon_{\text{OUT}} - \sum \dot{m}_{\text{IN}} \cdot \varepsilon_{\text{IN}} + \dot{E}_{\text{ex,D}} \tag{1}$$

Specific exergy of any flow stream is defined, according to [8], as:

$$\varepsilon = (h - h_0) - T_0 \cdot (s - s_0) \tag{2}$$

The exergy power of any flow stream can be defined by an equation [9]:

$$\dot{E}_{\text{ex}} = \dot{m} \cdot \varepsilon = \dot{m} \cdot \left[(h - h_0) - T_0 \cdot (s - s_0)\right] \tag{3}$$

At temperature T, the exergy transfer by heat ($\dot{X}_{\text{heat}}$) can be defined, according to [10], as:

$$\dot{X}_{\text{heat}} = \sum (1 - \frac{T_0}{T}) \cdot \dot{Q} \tag{4}$$

The exergy efficiency of any system or a volume has an overall definition which can be found in [11]:

$$\eta_{\text{ex}} = \frac{\text{Exergy output}}{\text{Exergy input}} \tag{5}$$

In the exergy analysis of any volume or a system in steady state it is usually assumed that leakage of any flow stream does not occur (or if does, it should be measured and included in the exergy balance). Following such assumption, as described also in [12] and [13], the mass balance equation is:

$$\sum \dot{m}_{IN} = \sum \dot{m}_{OUT} \quad (6)$$

3.2. Equations for the exergy analysis of investigated wet cooling tower

Investigated cooling tower exergy analysis (as well as exergy analysis of any other control volume or system) depends on ambient conditions (the ambient pressure and temperature). The base ambient conditions (base ambient state) for the cooling tower exergy analysis are the ambient pressure of 1 bar and the ambient temperature of 15 °C.

During the exergy analysis of any steam system or any of its components, numerical change in the ambient temperature can be performed in order to investigate the ambient temperature influence on the system or component exergy losses and exergy efficiencies, [14] and [15]. The change in ambient pressure, in most cases, is not significant and it cannot have a notable influence on any steam system or component exergy losses and exergy efficiencies.

The exergy analysis equations of wet cooling tower investigated in this paper are presented according to cooling tower operating points from Fig. 1:

Mass flow balance

- Water mass flow balance:

$$\dot{m}_1 = \dot{m}_2 \quad (7)$$

- Air mass flow balance:

$$\dot{m}_3 = \dot{m}_4 \quad (8)$$

Exergy balance

- Cooling tower exergy power input:

$$\dot{E}_{ex,IN} = \dot{m}_2 \cdot \varepsilon_2 + \dot{m}_3 \cdot \varepsilon_3 \quad (9)$$

- Cooling tower exergy power output:

$$\dot{E}_{ex,OUT} = \dot{m}_1 \cdot \varepsilon_1 + \dot{m}_4 \cdot \varepsilon_4 \quad (10)$$

- Cooling tower exergy destruction:

$$\dot{E}_{ex,D} = \dot{E}_{ex,IN} - \dot{E}_{ex,OUT} = \\ = \dot{m}_2 \cdot \varepsilon_2 + \dot{m}_3 \cdot \varepsilon_3 - \dot{m}_1 \cdot \varepsilon_1 - \dot{m}_4 \cdot \varepsilon_4 \quad (11)$$

- Cooling tower exergy efficiency:

$$\eta_{ex} = \frac{\dot{E}_{ex,OUT}}{\dot{E}_{ex,IN}} = \frac{\dot{m}_1 \cdot \varepsilon_1 + \dot{m}_4 \cdot \varepsilon_4}{\dot{m}_2 \cdot \varepsilon_2 + \dot{m}_3 \cdot \varepsilon_3} \quad (12)$$

4. The operating parameters of cooling tower necessary for the exergy analysis

Wet cooling tower exergy analysis is performed by using temperatures, pressures and mass flows of each cooling tower fluid stream (in each operating point from Fig. 1). Those operating parameters were found in [16].

The cooling tower load is defined by a temperature of cooling water that enters from steam condenser into the cooling tower (operating point 2, Fig. 1). At low cooling tower load cooling water temperature at the cooling tower inlet is equal to 38.84 °C, at middle load is equal to 44.82 °C and at high cooling tower load is equal to 45.44 °C. Temperature of cooling water and thus cooling tower load is proportional to steam condenser load - higher steam mass flow at the steam condenser inlet denotes a higher condenser load [17]. Steam mass flows at the condenser inlet at low, middle and high cooling tower loads are 14.750 kg/s, 22.361 kg/s and 23.417 kg/s, respectively.

In the analyzed wet cooling tower heat is transferred from hot water (operating point 2, Fig. 1) to air (operating point 3, Fig. 1). Each cooling tower load, at each ambient temperature, required calculation of air specific exergies (operating points 3 and 4, Fig. 1), that are necessary for cooling tower exergy analysis. From NIST REFPROP 9.0 software [18] air is selected with characteristics and specifications presented in Table 1.

Table 1. *Characteristics and specifications of air used in cooling tower exergy analysis*

Air mass fractions	Nitrogen	75.57 %
	Oxygen	23.16 %
	Argon	1.27 %
Critical properties	Temperature	-140.32 °C
	Pressure	38.508 bar
	Density	344.76 kg/m^3
Air molar mass		28.959 kg/kmol

The operating parameters of each fluid flow stream required for the cooling tower exergy analysis are presented in Table 2 for low cooling tower load, in Table 3 for middle cooling tower load and finally in Table 4 for high cooling tower load.

Specific enthalpies and specific exergies of each fluid flow stream are also presented in Table 2, Table 3 and Table 4. They were calculated by using NIST REFPROP 9.0 software [18]. Specific exergies of any fluid stream presented in all three tables are calculated for the base ambient state (the ambient pressure of 1 bar and the ambient temperature of 15 °C).

Table 2. *Operating parameters of the analyzed cooling tower - low cooling tower load*

OP*	Temperature (°C)	Pressure (bar)	Mass flow (kg/s)	Specific enthalpy (kJ/kg)	Specific exergy (kJ/kg)
1	29.41	5.00	826.389	123.70	1.857
2	38.84	5.00	826.389	163.10	4.306
3	32.70	1.01	613.333	306.20	1.349
4	35.40	1.01	613.333	308.92	1.517

* OP = Operating Point (according to Fig. 1)

Table 3. *Operating parameters of the analyzed cooling tower - middle cooling tower load*

OP*	Temperature (°C)	Pressure (bar)	Mass flow (kg/s)	Specific enthalpy (kJ/kg)	Specific exergy (kJ/kg)
1	30.48	5.00	826.389	128.20	2.079
2	44.82	5.00	826.389	188.10	6.435
3	32.70	1.01	613.333	306.20	1.349
4	39.10	1.01	613.333	312.64	1.784

* OP = Operating Point (according to Fig. 1)

Table 4. *Operating parameters of the analyzed cooling tower - high cooling tower load*

OP*	Temperature (°C)	Pressure (bar)	Mass flow (kg/s)	Specific enthalpy (kJ/kg)	Specific exergy (kJ/kg)
1	30.58	5.00	826.389	128.60	2.100
2	45.44	5.00	826.389	190.70	6.681
3	32.70	1.01	613.333	306.20	1.349
4	39.50	1.01	613.333	313.05	1.816

* OP = Operating Point (according to Fig. 1)

5. Cooling tower exergy analysis results and discussion

In the investigated cooling tower exergy analysis, each calculated operating parameter, regardless of the current cooling tower load, is presented for the various ambient temperatures. Throughout the complete analysis, the ambient temperature was varied in a range from 5 °C to 20 °C, with a step of 5 °C.

Exergy power input of the analyzed cooling tower at each observed load and at each ambient temperature is calculated by using Eq. 9.

Fig. 2 presents that the highest cooling tower exergy power input is at high cooling tower load and then decreases with a decrease in

cooling tower load. This fact is valid regardless of the observed ambient temperature.

In the observed ambient temperature range (between 5 °C and 20 °C) a decrease in the ambient temperature results with an increase in cooling tower exergy power input. This fact is valid regardless of the observed cooling tower load. Therefore, the highest cooling tower exergy power inputs were obtained at the ambient temperature of 5 °C and are 8197.89 kW at low cooling tower load, 10612.60 kW at middle and 10883.66 kW at high cooling tower load, Fig. 2.

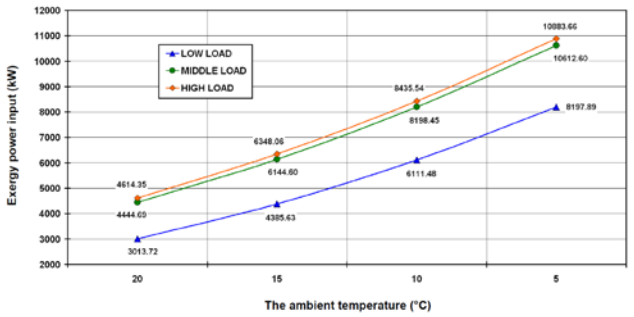


Fig. 2. *Change in the analyzed cooling tower exergy power input for the different ambient temperatures at three condenser loads*

Change in analyzed cooling tower exergy power output has identical trends as the change in cooling tower exergy power input, Fig. 2 and Fig 3. Cooling tower exergy power output at each observed load and at each ambient temperature is calculated by using Eq. 10.

The highest cooling tower exergy power output can be seen at the high cooling tower load and then decreases with a decrease in cooling tower load, what is a valid conclusion regardless of the observed ambient temperature, Fig. 3.

An increase in the ambient temperature resulted with a decrease in cooling tower exergy power output, what is a valid conclusion regardless of the observed cooling tower load. The highest cooling tower exergy power outputs were obtained at the ambient temperature of 5 °C and amounts 5272.24 kW at low cooling tower load, 5815.67 kW at middle cooling tower load and 5870.55 kW at high cooling tower load, Fig. 3.

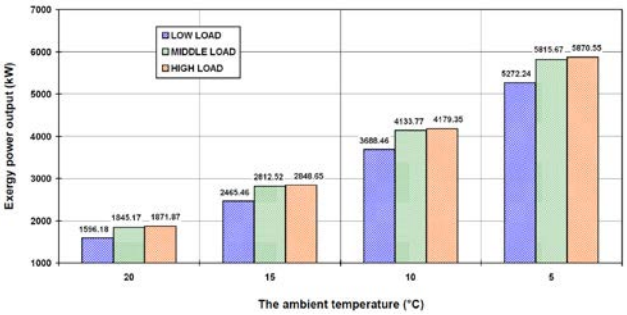


Fig. 3. *Change in the analyzed cooling tower exergy power output for the different ambient temperatures at three condenser loads*

Exergy destruction (exergy power losses) of the analyzed cooling tower is calculated by Eq. 11, regardless of cooling tower load and the ambient temperature.

The lowest cooling tower exergy destruction is obtained at low cooling tower load and in the observed ambient temperature range it amounts between 1417.54 kW and 2925.65 kW, Fig. 4. Increase in cooling tower load resulted with an increase in exergy destruction, which is therefore the highest at high cooling tower load.

An increase in the ambient temperature decreases cooling tower exergy destruction, regardless of the observed cooling tower load, Fig. 4. At the highest observed ambient temperature of 20 °C the lowest cooling tower exergy destructions are calculated which are 1417.54 kW at cooling tower low load, 2599.52 kW at the middle and 2742.48 kW at high cooling tower load.

From the exergy destruction aspect, for the analyzed cooling tower it would be advisable to operate at low load and at the highest possible ambient temperature - for such operating conditions cooling tower exergy destruction will be the lowest.

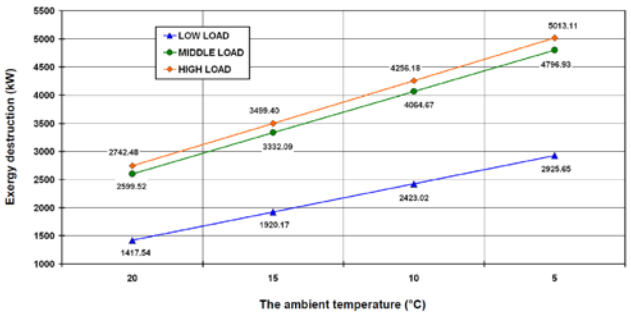


Fig. 4. *Change in the analyzed cooling tower exergy destruction for the different ambient temperatures at three condenser loads*

The exergy efficiency of the cooling tower analyzed in this paper is calculated by using Eq. 12 at any ambient temperature and cooling tower load.

Cooling tower at low load has the highest exergy efficiencies (between 52.96 % and 64.31 % in the observed ambient temperature range). Increase in cooling tower load results with a decrease in exergy efficiency at any ambient temperature, Fig. 5.

Decrease in the ambient temperature increases cooling tower exergy efficiency at any load. Therefore, the highest cooling tower exergy efficiencies are calculated at the ambient temperature of 5 °C and are 64.31 % at cooling tower low load, 54.80 % at middle load and 53.94 % at cooling tower high load, Fig. 5.

Considering the cooling tower exergy efficiency only, the best option for cooling tower operation will be low load and the lowest possible ambient temperature. During such operating condition cooling tower exergy efficiency will be the highest.

The analyzed cooling tower is one of the components of the entire cogeneration power plant which exergy efficiency is significantly influenced by the ambient temperature change. The change in ambient temperature for 5 °C resulted with a change in cooling tower exergy efficiency of 4 % or more on average, while taking into account all of the observed cooling tower loads.

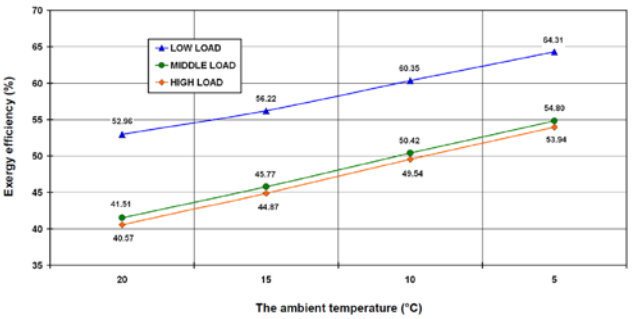


Fig. 5. *Change in the analyzed cooling tower exergy efficiency for the different ambient temperatures at three loads*

Presented wet cooling tower exergy analysis enables two important conclusions for its operation. From the aspect of cooling tower load its operation should be performed at low load - at low load cooling tower exergy destruction is the lowest while exergy efficiency is the highest when compared to other loads. This conclusion is valid for any ambient temperature.

From the ambient temperature aspect, optimal cooling tower operation cannot be obtained because at low ambient temperatures cooling tower will have the highest exergy efficiencies but also the highest exergy destructions. At high ambient temperatures, cooling tower exergy destructions will be the lowest but simultaneously, exergy efficiencies will be the lowest, Fig. 4 and Fig. 5. Finally, from the aspect of the ambient temperature, the priority in the analyzed cooling tower operation should be determined - minimum exergy destructions or maximum exergy efficiencies.

6. Conclusions

In this paper an exergy analysis of wet cooling tower from cogeneration power plant is presented. The cooling tower is analyzed at three different loads and in a range of the ambient temperatures. The most important conclusions of the analysis are:

- Cooling tower exergy power input and output has identical trends during the change in load and ambient temperature. Increase in cooling tower load resulted with an increase in the exergy power input and output (at any ambient temperature), while an increase in the ambient temperature resulted with a decrease in cooling tower exergy power input and output (at any cooling tower load).
- Increase in cooling tower load increases cooling tower exergy destruction, regardless of the ambient temperature. An increase in the ambient temperature causes a decrease in cooling tower exergy destruction, regardless of the current load. In a range of observed ambient temperatures (from 5 °C to 20 °C) cooling tower exergy destruction at low load is between 1417.54 kW and 2925.65 kW, while at high load exergy destruction range is between 2742.48 kW and 5013.11 kW.
- Increase in cooling tower load decreases cooling tower exergy efficiency, regardless of the ambient temperature. An increase in the ambient temperature causes a decrease in cooling tower exergy efficiency, regardless of the current load. The highest cooling tower exergy efficiencies are calculated at the lowest observed ambient temperature of 5 °C - they amounts 64.31 % at low load, 54.80 % at middle load and 53.94 % at high load.
- The analyzed cooling tower is one of the steam power plant components which exergy efficiency is significantly influenced by the ambient temperature change. The change in ambient temperature for 5 °C resulted with a change in cooling tower exergy efficiency of 4 % or more on average (by taking into account any cooling tower load).
- From the viewpoint of cooling tower load - cooling tower should operate at low load - at low load cooling tower exergy destruction is the lowest and exergy efficiency is the highest when compared to other loads, at any ambient temperature.
- Optimal cooling tower operation from the viewpoint of the ambient temperature cannot be obtained because an increase in the ambient temperature resulted with a simultaneous decrease in exergy destruction and in exergy efficiency, and vice versa. Therefore, from the aspect of the ambient temperature the priority in the analyzed cooling tower operation should be determined - minimum exergy destructions or maximum exergy efficiencies.

7. Acknowledgment

This work has been fully supported by the Croatian Science Foundation under the project IP-2018-01-3739.

8. Nomenclature

Latin Symbols:		***Greek symbols:***	
$\dot{E}$	the total exergy of flow, kW	ε	specific exergy, kJ/kg
h	specific enthalpy, kJ/kg	η	efficiency, -
$\dot{m}$	mass flow rate, kg/s		
p	pressure, bar	***Subscripts:***	
P	power, kW	0	ambient state
$\dot{Q}$	heat transfer, kW	D	destruction (ex. loss)
s	specific entropy, kJ/kg·K	ex	exergy
T	temperature, °C or K	IN	inlet (input)
$\dot{X}_{\text{heat}}$	heat exergy transfer, kW	OUT	outlet (output)

9. References

[1] Erdem, H.H., Akkaya, A.V., Cetin, B., Dagdas, A., Sevilgen, S.H., Sahin, B., Teke, I., Gungor, C., Atas, S.: *Comparative energetic and exergetic performance analyses for coal-fired thermal power plants in Turkey*, International Journal of Thermal Sciences 48, p. 2179–2186, 2009. (doi:10.1016/j.ijthermalsci.2009.03.007)

[2] Koroglu, T., Sogut, O. S.: *Conventional and Advanced Exergy Analyses of a Marine Steam Power Plant*, Energy 163, p. 392-403, 2018. (doi:10.1016/j.energy.2018.08.119)

[3] Aljundi, I. H.: *Energy and exergy analysis of a steam power plant in Jordan*, Applied Thermal Engineering 29, p. 324–328, 2009. (doi:10.1016/j.applthermaleng.2008.02.029)

[4] Blecich, P., Senčić, T., Wolf, I., Bonefačić, I.: *Numerical investigation of heat and mass transfer inside a wet cooling tower*, Technical Journal 12 (3), p. 131-138, 2018. (doi:10.31803/tg-20171017145907)

[5] Mrzljak, V., Poljak, I., Medica-Viola, V.: *Energy and Exergy Efficiency Analysis of Sealing Steam Condenser in Propulsion System of LNG Carrier*, International Journal of Maritime Science & Technology "Our Sea" 64 (1), p. 20-25, 2017. (doi:10.17818/NM/2017/1.4)

[6] Mrzljak, V., Poljak, I., Medica-Viola, V.: *Thermodynamical analysis of high-pressure feed water heater in steam propulsion system during exploitation*, Shipbuilding 68 (2), p. 45-61, 2017. (doi:10.21278/brod68204)

[7] Mrzljak, V., Senčić, T., Žarković, B.: *Turbogenerator Steam Turbine Variation in Developed Power: Analysis of Exergy Efficiency and Exergy Destruction Change*, Modelling and Simulation in Engineering 2018. (doi:10.1155/2018/2945325)

[8] Poljak, I., Orović, J., Mrzljak, V.: *Energy and Exergy Analysis of the Condensate Pump During Internal Leakage from the Marine Steam Propulsion System*, Scientific Journal of Maritime Research 32 (2), p. 268-280, 2018. (doi:10.31217/p.32.2.12)

[9] Mrzljak, V., Poljak, I., Medica-Viola, V.: *Dual fuel consumption and efficiency of marine steam generators for the propulsion of LNG carrier*, Applied Thermal Engineering 119, p. 331–346, 2017. (doi:10.1016/j.applthermaleng.2017.03.078)

[10] Mrzljak, V., Poljak, I., Mrakovčić, T.: *Energy and exergy analysis of the turbo-generators and steam turbine for the main feed water pump drive on LNG carrier*, Energy Conversion and Management 140, p. 307–323, 2017. (doi:10.1016/j.enconman.2017.03.007)

[11] Orović, J., Mrzljak, V., Poljak, I.: *Efficiency and Losses Analysis of Steam Air Heater from Marine Steam Propulsion Plant*, Energies 2018, 11 (11), 3019 (doi:10.3390/en11113019)

[12] Mrzljak, V., Prpić-Oršić, J., Senčić, T.: *Change in Steam Generators Main and Auxiliary Energy Flow Streams During the Load Increase of LNG Carrier Steam Propulsion System*, Scientific Journal of Maritime Research 32, p. 121-131, 2018. (doi:10.31217/p.32.1.15)

[13] Mrzljak, V.: *Low power steam turbine energy efficiency and losses during the developed power variation*, Technical Journal 12 (3), p. 174-180, 2018. (doi:10.31803/tg-20180201002943)

[14] Mrzljak, V., Poljak, I., Medica-Viola, V.: *Efficiency and losses analysis of low-pressure feed water heater in steam propulsion system during ship maneuvering period*, Scientific Journal of Maritime Research 30, p. 133-140, 2016. (doi:10.31217/p.30.2.6)

[15] Mrzljak, V., Poljak, I., Žarković, B.: *Exergy Analysis of Steam Pressure Reduction Valve in Marine Propulsion Plant on Conventional LNG Carrier*, International Journal of Maritime Science & Technology "Our Sea" 65(1), p. 24-31, 2018. (doi:10.17818/NM/2018/1.4)

[16] Burin, E. K., Vogel, T., Multhaupt, S., Thelen, A., Oeljeklaus, G., Gorner, K., Bazzo, E.: *Thermodynamic and economic evaluation of a solar aided sugarcane bagasse cogeneration power plant*, Energy 117, Part 2, p. 416-428, 2016. (doi:10.1016/j.energy.2016.06.071)

[17] Medica-Viola, V., Pavković, B., Mrzljak, V.: *Numerical model for on-condition monitoring of condenser in coal-fired power plants*, International Journal of Heat and Mass Transfer 117, p. 912–923, 2018. (doi:10.1016/j.ijheatmasstransfer.2017.10.047)

[18] Lemmon, E.W., Huber, M.L., McLinden, M.O.: *NIST reference fluid thermodynamic and transport properties REFPROP*, version 9.0, User's guide, Colorado, 2010.

PREPARATION AND PROPERTIES OF CARBON ADSORBENTS BASED ON PLANT RAW MATERIALS AND POLYMERIC WASTE

Assoc. Ph.D. Nistratov A.V., Prof. Dr. Klushin V.N.
Faculty of Biotechnology and Industrial Ecology -
Mendeleev University of Chemical Technology of Russia

alvinist5@gmail.com

Abstract: *The object of the research is waste polyethylene, polypropylene, polyethyleneterephthalate and polyvinylchloride, which are subjected to pyrolysis utilization with plant raw materials as a carrier. The purpose of the study is the thermal processing of these wastes into carbon adsorbents and the analysis of their adsorption properties. Combinations of the most spread polymeric wastes and plant raw materials, as well as products of its transformation (wood, peat, lignite, coal and its coke) were studied as feedstocks for the production of carbon adsorbents. The temperature regime of pyrolysis of plant materials was determined according to the results of thermographic analysis. The effect of the type of raw materials and polymeric wastes on the yield and on the parameters of porous structure of the produced adsorbents was estimated and the high-quality samples among them were selected.*

Keywords: *PLANT RAW MATERIAL, POLYMER WASTE, UTILIZATION, PYROLYSIS, ADSORBENTS*

1. Introduction

These studies are aimed at implementing the state strategy in the field of recycling production and consumption wastes [1], in particular, waste packaging polymers. According to various estimates, the volume of formation of polymer waste in Russia is 700–900 thousand tons per year, with packaging materials made of polyethylene (PE, 34%), polyethylenterephthalate (PET, 20%) and polypropylene (PP, 14%) prevail in their composition. Polyvinylchloride (PVC), predominantly in the form of plastic utensils, also constitutes a significant part of municipal solid waste (MSW). The introduction of the system of separate collection of the latter from 2019 will stimulate the utilization of MSW, however, the contaminated and mixed part of them is not recyclable and will be taken out of circulation.

Disposal of polymer wastes is possible in several ways: mechanical, chemical, thermal processing (pyrolysis and incineration), the latter being expedient for heterogeneous and contaminated polymer wastes. Unlike combustion, pyrolysis allows one to produce liquid fuel from such materials. It is promising to study the production of carbon-containing adsorbents by pyrolysis of these wastes in the presence of mineral and carbon carriers, which can increase the profitability of such disposal.

The listed wastes belong to polymeric materials that do not form a solid residue at complete thermal decomposition. The possibility of their involvement, like other organic wastes, in the production of composite adsorbents is provided by the CVD method — pyrolysis of the precursor, accompanied by “chemical vapour deposition” and carbonization of its products with the formation of pyrolytic carbon on porous mineral carriers — silica gels, clays, zeolites [2]. With respect to polyurethane waste, the described process, called “heterogeneous secondary pyrolysis” [3], was investigated using activated carbon and the solid pyrolysis product of polyurethane itself as carriers. The result was a change in the composition of the liquid pyrolysis products and the formation of an additional amount of coke on the surface of the carriers, but the materials obtained were not considered as adsorbents. For the purpose of producing the described adsorbents, it is promising to use carbon-rich kinds of plant materials - wood, peat, coal, lignite, and coke.

2. Experimental part

To carry out research, the studied wastes (precursors) were prepared as follows: packages from transparent LDPE polyethylene cut into strips about 1 cm wide, fragments of glasses from polypropylene and bottles from polyethylenterephthalate up to 2 cm in size, and white PVC shavings up to 1 mm thick. Relatively cheap materials of plant origin were used as carriers: pine sawdust, sedge peat from the field «Krasny Mokh», lignite from Tulgan field, coal mixture from JSC «Moskoks», metallurgical (russian state standard GOST 3340-88) and pitch coke (GOST 3213-91). All they besides powder-form peat were shredded to give fraction 1-2 mm and then dried at 110 °C to reach constant weight.

In order to determine the rational temperature regime of pyrolysis of these plant materials, their thermal analysis was carried out. The measurements were performed using a Q-1200 derivatograph (MOM, Hungary) by heating shredded air-dry samples to 900 °C for 100 minutes in a nitrogen atmosphere. The mass of the samples and the range of the weight scale G are indicated on the corresponding thermograms.

Based on construction of pyrolytic furnaces with a retort chamber, which are common in practice, the conditions of their functioning at laboratory scale were reproduced in a non-hermetically sealed porcelain crucible placed in a muffle furnace with an adjustable temperature. In such experiments, a sample taken from a hand-made mixture of a plant material and a polymer waste in a mass ratio of 1 : 1 was loaded into a porcelain crucible, which was covered with a steel lid. The latter was placed in a muffle furnace. The pyrolysis parameters (heating rate, final temperature and holding time) were set by the furnace regulator using the data of the below described thermographic tests.

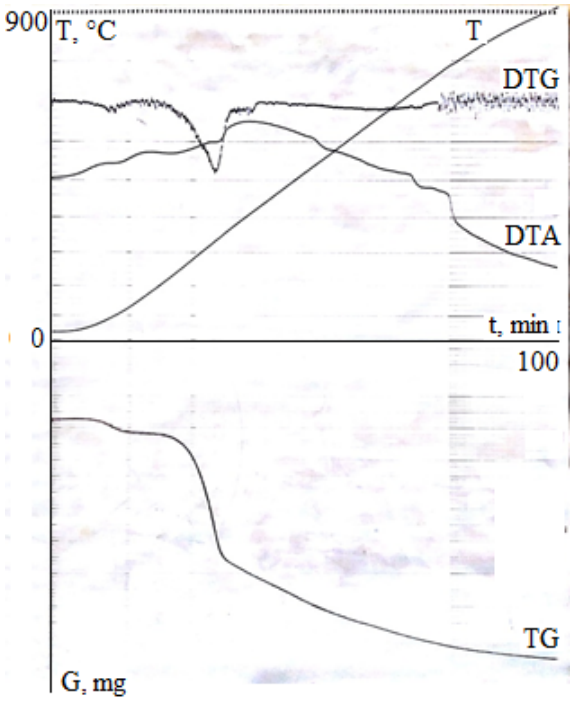
Upon completion of the pyrolysis, the crucible was removed from the furnace and placed in a desiccator, where it cooled to room temperature. Then, by weighing it, the yield of each adsorbent was calculated as the ratio of its mass to the mass of the raw mixture and to the mass of the carrier. The content of pyrolytic carbon in the adsorbent also was estimated by difference between yields of the adsorbent in presence and without precursor in raw mixture.

Parameters of porous structure, ash content and abrasion hardness of the products were found using methods described below.

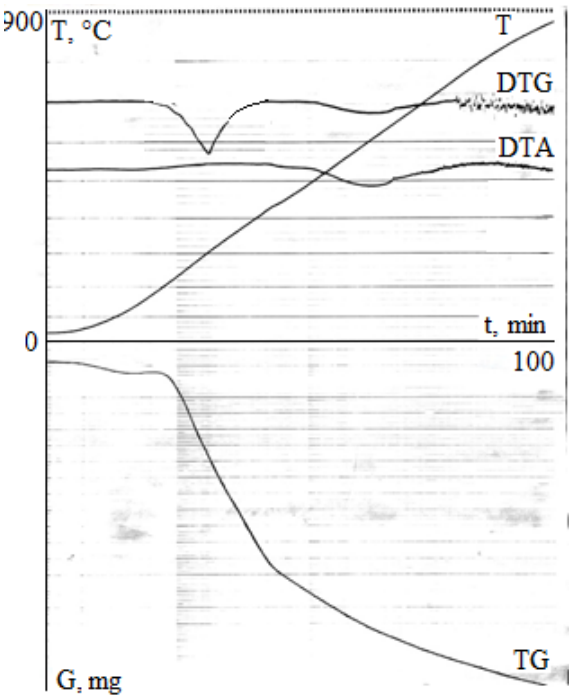
3. Results and discussion

3.1. Thermographic analysis of plant materials

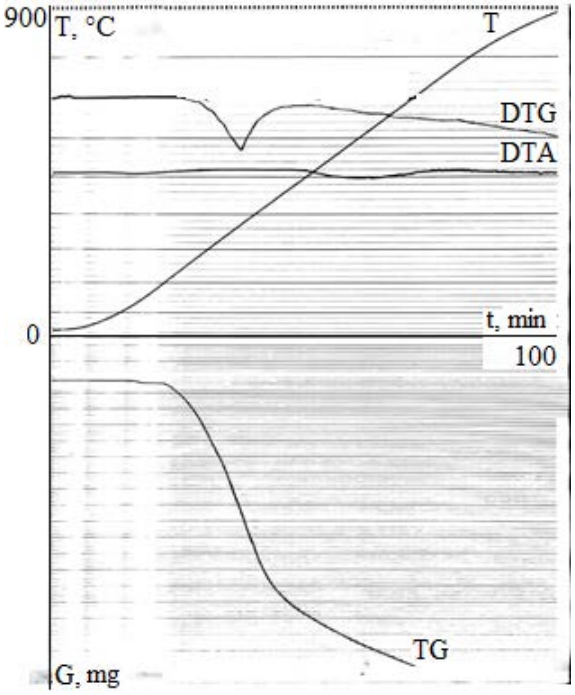
The characteristic quantitative parameters of the presented in fig. 1 thermograms and indicators of the obtained carbonized residues of the materials studied are given in table 1.



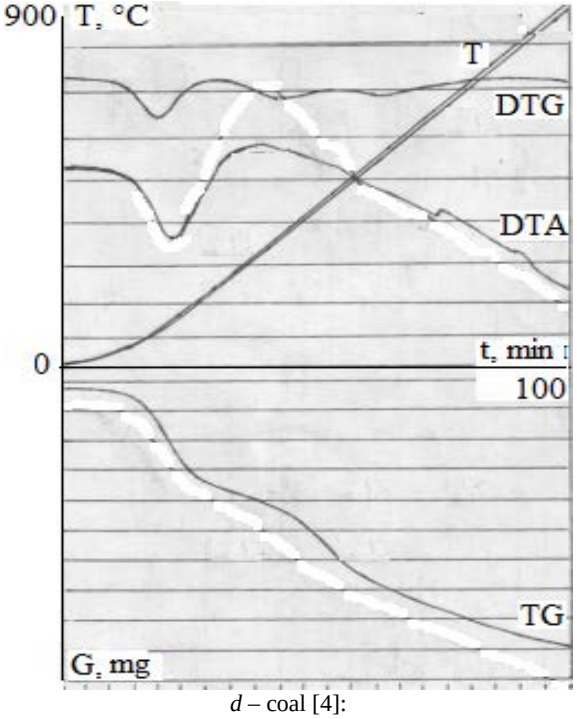
a – pine sawdust:
batch 141 mg, scale G 200 mg



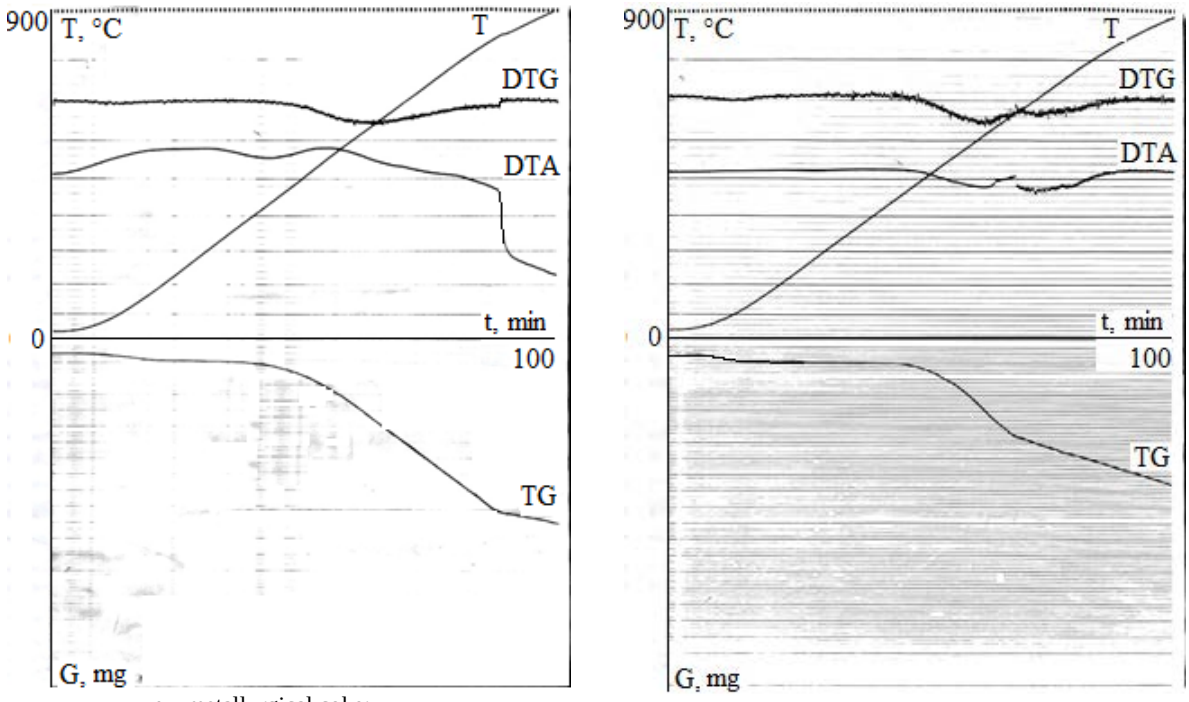
b – peat:
batch 323 mg, scale G 200 mg



c – lignite:
batch 364 mg, scale G 200 mg



d – coal [4]:
batch 821 mg, scale G 500 mg



e – metallurgical coke:
batch 749 mg, scale G 200 mg

f – pitch coke:
batch 619 mg, scale G 200 mg

Fig. 1 *Thermograms of plant raw materials*

Table 1: *Data of thermographic analysis of plant materials*

Raw material	Mass [mg]		Residue [%] at temperature, °C				Temperature range of the most intense mass loss, [°C]	Exterior of residue
	initial	final	300	500	700	900		
Sawdust	141	0,4	73	22	6,4	0,3	200-370	black dust
Peat	323	6,1	78	53	44	1,9	160-420	brown crumbly clumps
Lignite	364	37	90	59	50,5	10	240-460	brown grains and powder
Coal	821	391	80,5	65,5	52,5	47,6	60-240 260-500	black particles
Metallurgical coke	749	638	99	98	92	85	450-820	black loose powder
Pitch coke	619	395	99	98	90,5	64	430-650	black loose powder with shrinkage

The presented data demonstrate that the studied materials differ in proceeding of their thermal decomposition. It should be noted that the heat resistance (the yield of a solid residue at a given temperature), is expected to increase as the plant mass turns into carbon material in nature. For all materials, except coal, one stage of decomposition (an interval of intense mass loss) is characteristic, shifting to higher temperatures during the transition from wood to coke. The exothermic heat effect of the pyrolysis processes in the case of sawdust, which is fixed by the DTA curve (Fig. 1*a*), mainly degenerates upon the transition to materials of a greater degree of metamorphism. Along with this, it can be stated that the main transformations of non-coked materials occur up to 500 °C. The yield of residues (carbonizates) in this case, with the exception of sawdust, exceeds 50% by weight, and at 700 °C it decreases by another 6-15,6%. Further heating is accompanied by a smooth loss of mass, mainly without pronounced thermal effects.

The types of coke industrially obtained from coal naturally belong to heat-resistant materials, a noticeable decomposition of which (mass loss of more than 2 %) occurs only at 500–900 °C (table 1). The carbonized coal and cokes have the most practical granular form, the other materials form powder products.

The recommended [5] pyrolysis (carbonization) temperatures are very similar for coal, peat and wood - 500-750 °C. The degradation temperatures of the studied polymers, on the contrary, are different [6]: for PE, PP, PET, PVC are >300, 200-300, >800, >400 °C, respectively. Therefore, the preparation of adsorbents from mixtures of these materials was carried out at a fixed temperature of 500 °C. The heating rate for slow carbonization was set at 5 °C / min, holding at the final temperature – for 0,5 h.

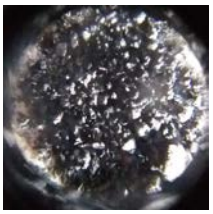
The composition of the by-products of pyrolysis of wood and peat is well studied [7, 8], vapor-gas species are represented by resinous substances, water, volatile compounds (alcohols, acids, esters, carbonyls) and gases (CO_2, CO, CH_4, light hydrocarbons, H_2). Coals during pyrolysis form in addition to coke, polyaromatics, benzene and its derivatives, as well as H_2O, CH_4, H_2, NH_3, H_2S [9].

3.2. Yields of adsorbents

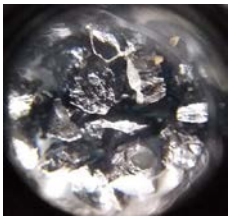
The look of the adsorbents obtained on the basis of the mentioned plant and polymeric materials is illustrated in fig. 2. According to the presented photos, the most macroporous materials are obtained by pyrolysis of sawdust and coke.



a - sawdust



b – peat



c – coal



d – coke

Fig. 2 *Images of carbon adsorbents obtained from plant raw materials (magnification x60)*

The outputs of the target products of the pyrolysis of raw materials are characterized in table 2 by 1) the ratio of their mass to the mass of the carriers, 2) to their mixtures with wastes and 3) the change in the yield of each adsorbent in the presence of various polymers in the feedstock (the latter indicator estimates the content of pyrocarbon in the adsorbent from the precursor).

Table 2: *Indicators of output of the adsorbents*

Raw material	Raw mass [g]	Adsor-bent mass [g]	Adsorbent yield [%]	Adsorbent yield from carrier [%]	Change in adsorbent yield [%]
Sawdust	1,5	0,37	24	24	-
Sawdust + PE	1,5	0,26	17	34	10
Sawdust + PP	1,45	0,24	16	32	8
Sawdust + PET	1,47	0,38	26	52	28
Sawdust + PVC	5,07	1,72	34	68	44
Peat	3,1	1,54	50	50	-
Peat + PE	2,72	0,87	32	64	12
Peat + PP	1,66	0,35	21	42	-8
Peat + PET	1,57	0,45	27	54	4
Lignite	1,28	0,73	57	57	-
Lignite + PE	2,56	0,78	30,5	61	4
Lignite + PP	2,56	0,7	27,5	55	-2
Coal	2,32	2	84	84	-
Coal + PE	3,08	1,85	60	120	36
Coal + PP	3,08	1,77	57,5	115	31
Coal + PET	3,08	1,68	54,5	109	25
Coal + PVC	3,08	1,85	60	120	36
Metall. coke + PE	3,08	1,61	52	104	4
Pitch coke + PE	3,08	1,7	55	110	10

In terms of experience, both types of coke do not change the mass, coal decomposes only by 16 %, lignite loses 43, peat – 50, and wood – 76 % of the mass. The content of pyrocarbon deposited on carriers during the decomposition of polymers varies within wide limits (table 2). In particular, wood precipitates 8-44 % of the mass of polymer-precursor in the form of pyrocarbon; lignite - up to 4; peat - from 4 to 12; coal - from 25 to 36 %; the rest of the polymers spent under the described conditions is converted into vapor-gas products. It is noticeable that thermoplastic polymers (PE, PP, PET) provide a smaller cover of adsorbents than thermosetting PVC. The fact, that polypropylene combined with peat and lignite results in unexpected mass loss (-8 and -2 % respectively), points to chemical activity of products of its destruction.

3.3. Porous structure of adsorbents

Characteristics of the porous structure of initial and carbonized materials are shown in table 3 as volumes of pores sorbing vapour substances with different molecular size: H_2O (ultramicropores) < C_6H_6 (micro- and mesopores) < CCl_4 (mesopores).

An analysis of the initial and carbonized materials at 500 °C reveals appearance of micro- and mesopores, which adsorb organic substances, during pyrolysis. Water-adsorbing micropores are most developed in the lignite sample, mesopores absorbing CCl_4 in the peat sample. The carbonized coal and coke remains low-porous.

Joint pyrolysis of raw materials and polymers in most cases leads to the development of their porous structure. Presumably, it happens by the mechanism of narrowing the existing pores of the carrier by covering them with a layer of pyrocarbon [10]. For adsorbents based on sawdust and thermoplastic polymers, new micropores appear, whose volume is record for PP (table 3), and for PET and PVC there are also new mesopores. The sample from pine sawdust and PP has the greatest volume of micropores (0.523 - 0.025 = 0,498 cm^3/g) that exceeds the same of active carbon from birch wood BAU (0.22-0.25 cm^3/g) [5].

For peat-based adsorbents, the resulting structure depends on the type of the polymer: the maximum volume of ultramicropores is due to the addition of PP, the micro- and mesopores sorbing benzene — the addition of PET, although these indicators are relatively small. Positive changes in the porous structure of wood-based and peat-based adsorbents are correlated with the content of pyrocarbon 4–44 % (table 2).

Using the example of joint pyrolysis of lignite with polymers, it can be seen that the effect of pyrolytic carbon deposition may be excessive - the volume of ultramicropores of samples with the addition of PE, PP is reduced in comparison to that of carbonized lignite. At the same time, samples from a mixture of components acquire additional mesopores. These changes mean the ability of adsorbents to absorb organic solvents predominantly compared to water (table 3).

Table 3: *Indicators of the porous structure of the adsorbents*

Raw material	Volume of pores [cm^3/g] sorbing vapours		
	H_2O	C_6H_6	CCl_4
Sawdust	0,144	0,102	0,049
Sawdust + PE	0,17	0,314	0,047
Sawdust + PP	0,361	0,523	0,025
Sawdust + PET	0,320	0,241	0,118
Sawdust + PVC	0,328	0,238	0,146
Peat	0,103	0,136	0,169
Peat + PE	0,052	0,073	0,065
Peat + PP	0,195	0,104	0,069
Peat + PET	0,052	0,261	0,075
Lignite	0,208	0,321	0,12
Lignite + PE	0,119	0,329	0,139
Lignite + PP	0,101	0,353	0,168
Coal	0,056	0,031	0,018
Coal + PE	0,018	0,032	0,021
Coal + PP	0,017	0,018	0,021
Coal + PET	0,029	0,033	0,027
Coal + PVC	0,015	0,024	0,029
Metall. coke + PE	0,010	0,008	0,011
Pitch coke + PE	0,017	0,018	0,016

All adsorbents based on coal and coke derived from it, despite the macropores (fig. 2*e*) and the deposition of 4-36 % of pyrocarbon, have low-developed porous structure, often inferior to those of carbonized carrier-materials.

Mineral impurities in the carbonizates of plant materials are commonly expressed by ash content, that was determined by calcination of the samples in opened crucibles at 800 °C for 2,5 hours: pine wood – 4,5; peat - 4; lignite – 17,1; coal – 12,4; metallurgical coke – 11,8, while the high-quality adsorbents should contain up to 5% ash.

A practically important property of carbon adsorbents is the abrasion hardness, which was estimated for granular adsorbents by their abrasion in rotating inner and outer cylinders for 3 minutes: lignite — 97 %, coal — 75 %, metallurgical coke — 98 % with an acceptable value of more than 85 % [5]. Consequently, only lignite adsorbents possess a combination of porous structure and mechanical hardness.

4. Conclusion

In the performed study, the pyrolytic decomposition of wood, peat, lignite and coal, metallurgical and pitch coke samples was studied, temperature of their processing with polymeric wastes to obtain carbon adsorbents with a maximum yield was substantiated, the contribution of polymer pyrolysis to their formation was estimated, and basic indicators of the porous structure of carbonized materials were found.

The effect of joint pyrolysis of raw materials and polymers with the ratio of 1 : 1 on the indicators of the porous structure of the adsorbents was revealed: additives of thermoplastics provide an increase in the sorbing pore volumes for H_2O, C_6H_6, CCl_4. The maximum pore volume for benzene of the sample based on sawdust and polypropylene (0,52 cm^3/g) exceeds that of most of industrial active carbons. Lignite gives hard and porous, but high-ash carbonizates. Coal and coke do not form porous adsorbents in combination with any polymers. Thus selection of the best sample depends on requirements to adsorbent properties.

Finding the best conditions for producing the studied adsorbents requires varying the ratio of components and temperature of pyrolysis. For low-porous adsorbents based on coal materials, vapor-gas activation can be recommended.

This work was supported by the Mendeleev University of Chemical Technology of Russia. Project number 004-2018.

5. Literature

1. Strategiya razvitiya promyshlennosti po obrabotke, utilizacii i obezvrezhivaniyu othodov proizvodstva i potrebleniya na period do 2030 g. Order of the Government of the Russian Federation No. 84-P. at 25.01.2018.

2. Eletsky P.M. Diss. Ph.D. Novosibirsk: Institute of Catalysis of G.K. Boreskov of Siberia Department of the Russian Academy of Sciences. 2009. 115 p.

3. Takamoto D.Y., Petrich M.A. Effect of Heterogeneous Secondary Pyrolysis Reactions on Thermal Decomposition of Polyurethane Scrap. Ind. Eng. Chem. Res. 1994. V. 33. P. 3004-3009.

4. Zo E. Nayng, Klushin V.N. Osobennosti termicheskogo i termookislitel'nogo raspada iskopaemogo uglya mestorozhdeniya Tejchik. Uspekhi v himii i himicheskoj tekhnologii. 2017. V. 31. No. 9. S. 34-36.

5. Mukhin V.M., Klushin V.N. Proizvodstvo i primenenie uglerodnyh adsorbentov: Moscow.: Mendeleev University of Chemical Technology of Russia, 2012. 308 p.

6. Ustinov V.A., Kozlita A.N., Lyulkin M.S. Vybor temperaturnogo rezhima v apparate piroliza na osnovanii himii processa. Neftegazovoe delo. 2011. No. 3. P. 208-214. URL: http://www.ogbus.ru.

7. Deineko I.P. Piroliz drevesiny. Bolshaya Rossijskaya Encyclopedia. URL: https://bigenc.ru/chemistry/text/3140758# (access date: 01/29/2019).

8. Zabelkin S.A. et al. Issledovanie processa termohimicheskoy pererabotki torfa i svoystv produktov poluchennyh pri raznyh temperaturah piroliza. Vestnik Kazanskogo Tehnologicheskogo Universiteta. 2013. № 21. URL: https://cyberleninka.ru/article/issledovanie-protsessa-termohimicheskoy-pererabotki-torfa-i-svoystv-produktov-poluchennyh-pri-raznyh-temperaturah-piroliza (access date: 01/29/2019).

9. Filonenko Yu.Y., Kaufman A.A., Filonenko V.Yu. Teoreticheskie osnovy tekhnologii koksovaniya kamennyh uglej. Lipeck: Lipeckij gosudarstvennyj tekhnicheskij universitet, 2015. 192 p.

10. Dabrowsky A., Tertykh V.A. Adsorbtion on new and modified in organic sorbents. Amsterdam: Elsevier, 1996. P. 115-146.

SUPPLY CHAIN PLANNING METHODOLOGY FOR METALS

Ass. Prof., Candidate of Technical Sciences, Solodovnikov V.[1,2]

[1] LOGIS Research and Development Laboratory, Frenstat pod Radgostem, Czech Republic
[2] National Research University Higher School of Economics, Moscow, Russia
E-mail: vsolodovnikov@hse.ru

Absract *The paper contains the results of the study on the systematization and formalization of specialized approaches to planning supply chains of leading metal companies and comparison of these practices with the standard supply chain management models SCOR & CCOR & DCOR and GSCF. The paper defines the main directions of development of the methodology of supply chain planning in terms of its adaptation to the specifics of metals.*
KEYWORDS: SUPPLY CHAIN MANAGEMENT, METALLURGY

1. Introduction

A series of changes in global markets led to a significant transformation of the supply chain management systems of leading metallurgical companies [1,2]. To improve competitiveness companies were forced to restructure their business processes and increase efficiency. Leading metal companies have developed specialized supply chain management approaches which in practice proved to be highly efficient around the world.

These methods in order to be used have to be formalized and studied. In this article, the author formalizes the main directions of development of the methodology of supply chain planning in terms of its adaptation to the specifics of the metals.

2. Preconditions and means for resolving the problem

The result of the survey conducted by the author were the systematization and formalization of the processes and their interactions, a comparison of these processes with the standard supply chain management models like SCOR + CCOR + DCOR [3,4,7] and GSCF [5-7].

The study was based on the analysis of public data of leading steel companies such as TimkenSteel, USA; Trinecke Zelezarny, Czech Republic; Severstal, Russia; MMK, Russia; OMK, Russia; Mechel, Russia; VSMPO-AVISMA Corporation, Russia and many other. A large contribution to this study has made materials from the leading providers of Advanced Planning and Scheduling software for the metallurgical industry: LOGIS, i2 Technologies, and others.

Figure 1 shows the organization of key planning processes in Metals. It is a generalization of the best practices of the abovementioned companies in the area of processes and supporting systems.

3. Results and discussion

From Supply Chain Management (SCM) point of view there are two most common cross-industrial SCM standards in the world: the SCOR model with extensions CCOR and DCOR from Supply Chain Council (SCC) and the model from the Global Supply Chain Forum (GSCF).

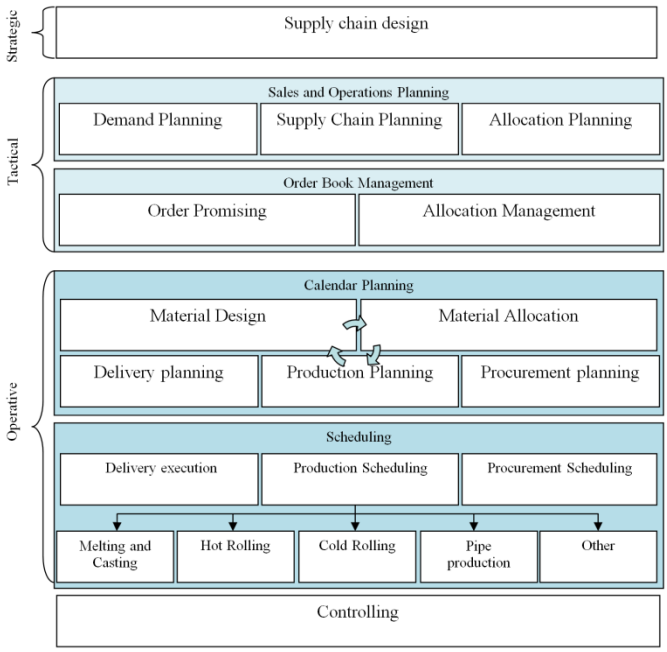


Fig 1 *Organization of key planning processes in Metals*

SCC is an independent, non-profit organization formed in 1996 by the global consulting company Pittiglio Rabin Todd & McGrath (PRTM) and research company Advanced Manufacturing Research (AMR) from Cambridge. At the beginning of its activity, SCC included 69 companies; today the list of participants includes more than 1000 companies.

GSCF under the guidance of Dr. Douglas M. Lambert provides an opportunity for practitioners and theorists to investigate critical issues related to the quality of customer service and operational efficiency, regardless of the specific functional expertise. The professional community of GSCF includes about 14 leading international companies [5,6], recognized as leaders in their industries.

The results of the comparison of the best practices of the organization of business processes of supply chain planning of metallurgical companies with standard models of supply chain management are given in table 1.

For ease of use, the processes of the GSCF model are numbered from 1 to 8 according to the original sequence [6].

For strategic level sub-processes, the suffix S is introduced, for operational level - O.

Table 1. *The results of the comparison of the best practices of the organization of business processes of supply chain planning of metallurgical companies with standard models of supply chain management*

Main process/level	Subprocesses		Model xCOR	Model GSCF
Supply Chain Design	Supply Chain Design		M4SC: SCOR tools could be used for that purpose	4S OF 1S CRM 6S SRM
Tactical planning				
• S&OP	Demand Planning		CCOR:Plan sP1.1	1O CRM 3O DM: forecasting
	Supply Chain Planning		sP1	3O DM: Synchronization
	Allocation Planning		sP1	3O DM: Synchronization
• Order Book Management	Allocation Management		sP1	3O DM: Synchronization
	Order Promising		sD1.2 sD2.2 sD1.3/sD2.3 sD3.3	2O CSM 4O OF
Operative Planning				
• Calendar planning	Production	Material planning/design/technology development	DCOR:Design	7O PDaC
		Material Allocation	sD1.3/sD2.3 sD3.3	4O OF: Process Order
		Production Planning	sP3	5O MFM
	Delivery planning		sP4	4O OF
	Procurement planning		sP2	4O OF
• Scheduling	Production scheduling		sM1.1 sM2.1 sM3.2	5O MFM
	Delivery execution		sD1.3/sD2.3 sD3.3	4O OF
	Procurement scheduling		sS1.1	4O OF
Efficiency evaluation	KPI		sED2 sES2 sEM2	Subprocess «Measure Performance» of corresponding GSCF processes

The presented comparative analysis of the best practices of planning in metallurgy with the known SCM models (SCOR, GSCF) determines the directions of development of these methodologies in terms of their adaptation to the features of supply chain planning of metallurgical companies:

1. Re-engineering the links of existing planning processes according to best practices in metallurgy planning.
2. Consolidating CCOR, SCOR and DCOR models into a single supply chain planning process system.
3. Adding clarification steps of the planning processes, introduction of additional if necessary.
4. Formalization of planning methods and models.
5. Requirements definition for supporting information technologies.

4. Conclusion

The formalization of the best practices of planning in metallurgy given in this article, as well as the results of their comparison with the standard models SCOR+CCOR+DCOR and GSCF, determine the main directions of development of the supply chain management methodology in terms of its adaptation to the specifics of planning in the metallurgical industry.

The need to systematize and develop the planning methodology is determined by the need for its application to ensure the competitiveness of metallurgical companies in a tough struggle in the global market.

5. Literature

[1] PwC, Steel in 2025: quo vadis?, PwC, 2015.
[2] KPMG, Global Metals Outlook, KPMG, 2015.
[3] Supply Chain Operations Reference Model v 10.0, Supply Chain Council, 2010, p. 856.
[4] V. Sergeev, Supply Chain Management, Uright, Moscow, 2015. P. 480. (in Russian)
[5] GSCF http://fisher.osu.edu/centers/scm/members/
[6] D. Lambert, Supply Chain Management: Processes, Partnerships, Performance. 3rd Edition, Supply Chain Management Institute, 2008, p. 431.
[7] H. Stadtler, Ch. Kilger, Supply Chain Management and Advanced Planning. Third Edition, Springer, Berlin, 2004, p. 512.

TRAFFIC SYNTHETIC MODEL DEVELOPMENT AND CALIBRATION IN ANAMORAVA REGION

Dr.sc. Ramadan Duraku[1], Prof.dr.Vaska Atanasova[2]
University of Prishtina"Hasan Prishtina", Faculty of Mechanical Engineering, Prishtina, Kosovo[2]
University "St.Kliment Ohridski", Faculty of Technical Sciences, Bitola, Macedonia[2]
E-mail: ramadan.duraku@uni-pr.edu, vaska.atanasova@tfb-uklo.edu

Abstract: *The main objective of this paper is to develop and calibrate traffic synthetic model for forecasting traffic demand in Anamorava region. The model on existing situation is developed based on "meta model" which uses PTV Visum software. In order to set up a model were taken into account input variables number of residents, number of people employed, working places available as well as the traffic volume entering and exiting this region at "peak hour". With intention to have traffic volumes as an outcome expressed as AADT, correction coefficients are applied. Multiplying the traffic volumes with correction coefficient there is traffic demand gained for the period of 24 hours which is an indicator to be used for comparison of results. In order to get the reliable model for forecasting, calibration of it is done through TFlow Fuzzy algorithm technique based on GEH test, R^2 and percentage deviation criterions. Once the level is completed satisfactory, the final model can be used to forecast the traffic demand for this region.*

Keywords*: SYNTHETIC MODEL, TRAFFIC DEMAND, MODELING, CALIBRATION.*

1. Introduction

Due to rapid changes of demographic as well as social-economic trends followed by changes in the living style, recently there is increasing requirement for development of models for traffic forecasting. Depending on zones to which it will be applied they could be macroscopic, mesoscopic and microscopic [1]. In the view of modelling period they could be 24 h or "peak hour" models, while on the aspect of treatment of trips they can also be classified as aggregate and disaggregate [2].

In this study is developed and calibrated synthetic four step traffic demand macro model through modelling techniques by PTV Visum software at the Anamorava region. These kind of models usually are used for strategic studies of traffic in which as an outcome there is generation of traffic expressed as Annual Average Daily Traffic AADT in road transport network [3].

They are used to generate traffic volumes distributed on the existing road network which is after compared with counting completed on some specific locations of this network. In case outcome data in traffic volumes are approximate the model as such can be used to forecasting. In case there is incompliance it should then make adjustment and calibration of them through various statistics indicators [2]. Since the model is developed by PTV Visum, in this case for adjusting and calibration of results are used TFlow Fuzzy algorithm technique which takes as basis GEH test, R^2 and percentage deviation indicators.

This is the way to give the significance of it in forecasting traffic demand.

2. Materials and methods

For development and calibration traffic synthetic model, study area is determined, research techniques and procedures, development synthetic model, traffic volume at specific road network sections, discussion results including calibration model and conclusions.

3.1 Study area

Development of the model is done for Anamorava region which is one of seven main regions of Kosova and as such this region is composed of six municipalities (Gjilani, Parteshi, Vitia, Kllokoti, Kamenica and Ranillugu) with total 166 settlements with the surface of 1331 km^2 [4]**.** It is limited with Prishtina region at North-West and Ferizaj at South, while with Serbia at South-West and Macedonia at South.

4.2 Research techniques

In order to complete this model the modelling technique is applied the process goes through four steps: design, verification, calibration and validation [5]. Design includes construction of the model taking into account graphical substrate, geometric elements of the road network, setting up O-D matrix etc.

Verification has to do with visual check of the model design and results should have logical sense. This could be used to detect incompliance's of the model in early stage and in this way we can avoid bigger errors in the later stage.

Calibration is the process of comparison of traffic data gained according to the model and data gained by field counting [6].

Validation has to do with assessment of model calibration process comparing values calibrated of model with real data gained by traffic counting with condition that some data are not included in setting the model. In this research three steps are applied and the last step in validation is ignored due to the lack of additional data to complete this action.

5.3 Synthetic model development

In order to develop synthetic model of traffic PTV Visum software is used, as such it contain special model known "meta-model" [7]. In this regard for its completion there is necessity to collect data on input variables such is population, number of employed persons, number of work places and the traffic volume on one side (demand model) and the data on road network on the other side (network model) [8]. All data is received from state authorities [9] who are competent to record and register these kinds of data as shown in Figure 1.

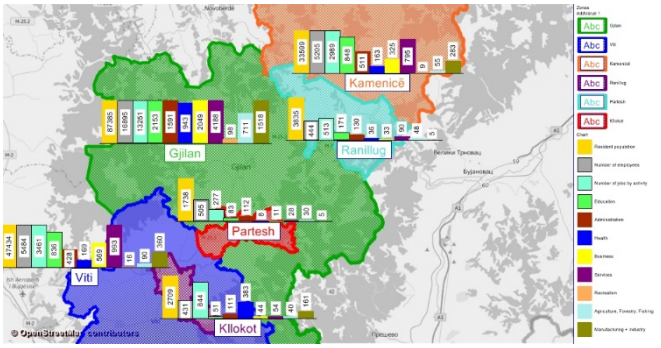


Figure 1*. Data for variables in Anamorava region – 2016*

In order to design the model there is a need to follow some steps such is selection of transport network (zoning, selection of road network, assigning attributes such is capacity, speed limits, installation of centroids and connectors) on one side and on the other side data on traffic demand expressed like AADT gained from counting of traffic participants. In this way the possibility is established to assess current and future traffic demand.

Zoning is composed from total 13 zones and most of them are inner zones (Gjilan, Vitia, Kamenica, Kllokot, Partesh and Ranillug), while seven of them are outer : 101 – Novoberdo, 102 –

Llabjan, 103 – Lipjan, 104 – Ramjan, 105 – Kacanik, 106 – Preshevo, and 107 – Bujanovc, which are presented in Figure 1.

The road network forms the basis of every transport-modelling project. In this case the road network is classified as require by the literature [10] taking into account only traffic volumes which are significant as presented in Figure 2.

Each link is associated thereafter with parameters defined, such as: capacity per lane, number of lanes, length, speed restrictions, allowed types of transport, etc.

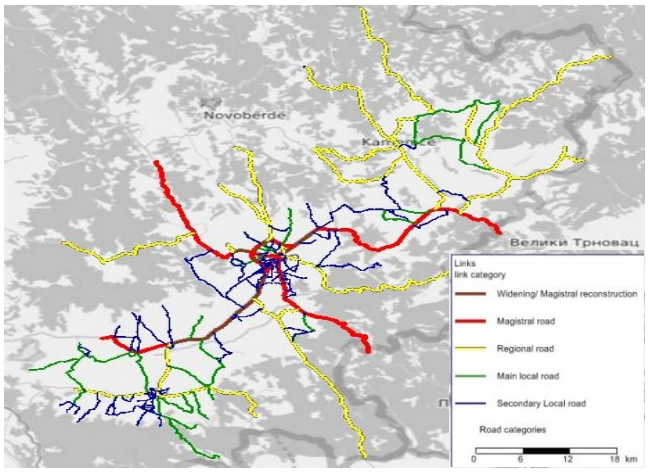


Figure 2. *Current road network of Anamorava region*

One of the most important actions in the zones is putting data attributes. Attributes are a key component in creating the model [11]. For normal functioning of traffic attributes of networks, elements must be defined for all activities and trips for each traffic zone in the region, which comprise 10 attributes inserted in PTV Visum software, as presented in Figure 3.

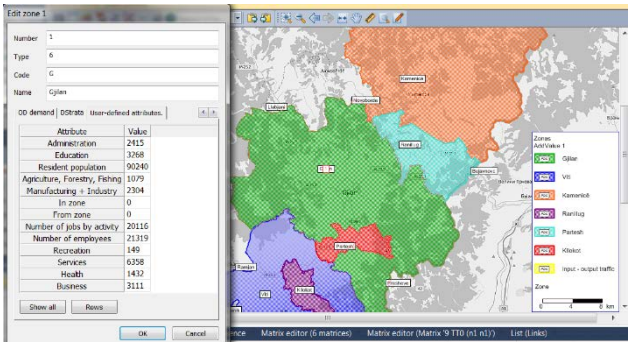


Figure 3. *Presented attributes in one zone (Gjilan).*

Centroids and their connectors play an important role in modelling. The centre of each zone is presented by centroids. Centroids make connection of each zone to the road network through connectors which make possible movement of private and public transport vehicles from Origin to Destination (O-D).

Connectors include distance, time and cost connection of transport system. Connectors for all 13 zones (6 municipalities and 7 transit zones) presented in Figure 4. The connectors in the case are shown in yellow colour.

Apart from input data there is necessity to get information on the intensity of traffic flow entering and exiting Anamorava region. Firstly specific locations are determined for which counting is done in order to review the traffic demand for this region.

After this counting is done at peak hour 16:00–17:00 on 15th January 2016, assisted by students of the Traffic and Transport Department at the University of Prishtina.

Recording of traffic flow according to directions and vehicle categories is done manually recording as well registration plates by the form which has been designed specifically for this purpose.

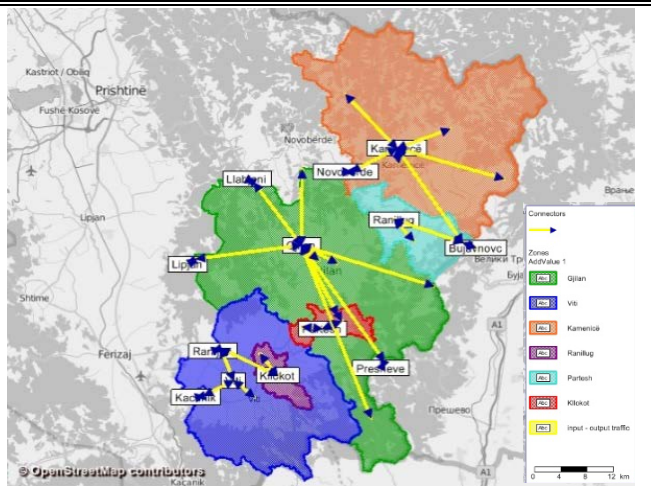


Figure 4. *Zones, centroids and connectors*

Locations in which counting are completed for entering and exiting traffic for Anamorava region is presented in Figure 5.

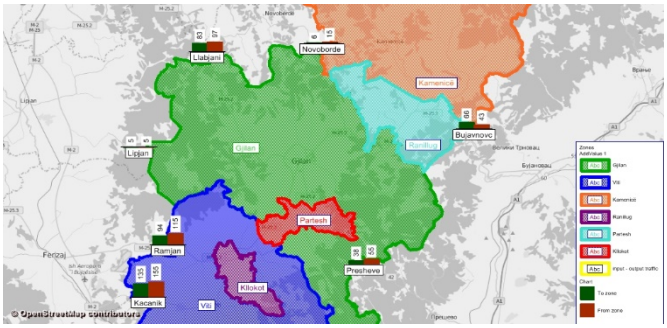


Figure 5. *Entering/Exiting traffic flow in Anamorava region – 2016*

These locations are connection of this region with other regions in Kosovo and neighbouring countries. Apart from the traffic entering and exiting this region there is also necessity for information related to the intensity of vehicles going transit classified in two categories as passenger vehicles and commercial vehicles as presented in Table 1 and Table 2.

Table 1: *Transit of passenger vehicles – C transit (vehicles/h)*

Entry/Exit	*101*	*102*	*103*	*104*	*105*	*106*	*107*
101	*0*	*0*	*0*	*0*	*1*	*0*	*0*
102	*0*	*0*	*0*	*0*	*1*	*7*	*12*
103	*3*	*0*	*0*	*0*	*2*	*0*	*0*
104	*0*	*0*	*0*	*0*	*0*	*0*	*0*
105	*0*	*0*	*0*	*0*	*0*	*0*	*0*
106	*0*	*6*	*0*	*0*	*0*	*0*	*0*
107	*0*	*10*	*0*	*0*	*0*	*0*	*0*

Table 2: *Transit of commercial vehicles – TT transit (vehicles/h)*

Enter/Exit	*101*	*102*	*103*	*104*	*105*	*106*	*107*
101	*0*	*0*	*0*	*0*	*0*	*0*	*0*
102	*0*	*0*	*0*	*0*	*0*	*3*	*4*
103	*0*	*0*	*0*	*0*	*0*	*0*	*0*
104	*0*	*0*	*0*	*0*	*0*	*0*	*0*
105	*0*	*0*	*0*	*0*	*0*	*0*	*0*
106	*0*	*2*	*0*	*0*	*0*	*0*	*0*
107	*0*	*3*	*0*	*0*	*0*	*0*	*0*

Counting shows that there are two categories of vehicles which have an influence in traffic and as such it is necessary to convert them to unit vehicles so that traffic influences to be approximately the same. Counting based on vehicle categories and converted to unit vehicles equivalent to passenger cars based on the standard presented in Table 3**.**

Thus, values gained should be multiplied by a coefficient $K_k=1.4$ to the equivalent "Passenger Car Space Equivalent" *(PCSE)* recommended by literature [12].

***Table 3**: Converting vehicles to PCSE*

Category of vehicle	*C*	*V&P*	*SM*	*LB*	*ST*	*MT*	*HT*
PCSE	*1.0*	*1.2*	*1.2*	*1.6*	*1.4*	*1.6*	*1.8*
Avg. PCSE	$K_e=1.4$						

Where: C-Car, VP-Vans&Pick UP, SM-Small Buses, LB-Large Buses, ST-Small Truck, MT-Medium Truck, HT-Heavy Truck.

Counting are accomplished on 15th January 2016 during peak hour for the period of 12h and as such is facilitated by nonlinear monthly seasonal coefficient $K_s=1.34$ as well as weekly one coefficient $K_w=1.01$.

On this base taking into account traffic flow per 12h and converted for 24h, multiplied by above coefficients we may determine value of traffic volume entering and exiting Anamorava in the period of 24h. These values can be obtained by using Eq. (1):

$$AADT = VOL \cdot K_e \cdot K_s \cdot K_w \qquad (vehicle/24h) \tag{1}$$

Where:
AADT- annual average daily traffic,
VOL - traffic volume,
K_e - passenger car space equivalent,
K_s - seasonal coefficient and
K_w -weekly nonlinear coefficient.

In setting up the model of PT Visum software are taken into consideration six types of trips as presented in Table 4 [13]. To get balancing of trips generated and attracted in the phase of distribution, gravity model is used for a single constrained. Assessment of parameters is done through "Tanner deterrence" function for travel time as input in the process of distribution by using Eq. (2) [5]:

$$f(t_{ij}) = a \cdot t_{ij}^{b} \cdot e^{c \cdot U_{ij}} \tag{2}$$

Where:
t_{ij}- value of travel time from zone *i* to zone *j*,
U_{ij}- travelling utility which are $U_{ij}=1/t^2_{ij}$,
a,b,c-parameters.

Factors distribution for six purposes of trips regarding the parameters a, b and c are given in Table 4.

***Table 4:** Factor distribution for parameters a, b and c*

		Parameters		
Purpose		*a*	*b*	*c*
Purpose 1	*n1 – home-work*	*4.3*	*1*	*-0.08*
Purpose 2	*n2 – home-school*	*3.8*	*1*	*-0.08*
Purpose 3	*n3 – home-business*	*3*	*1*	*-0.08*
Purpose 4	*n4 – home-shopping*	*3*	*1*	*-0.08*
Purpose 5	*n5 – home-other*	*4.2*	*1*	*-0.08*
Purpose 6	*n6 – not from home*	*3.8*	*1*	*-0.08*

According to the procedure of iteration and application of four step model (generation, distribution and assignment) traffic volume is generated in the road network classified according to road categories expressed as AADT, as presented in Figure 6. Initially productivity and attraction of trips is done followed by their distribution and at the end assignment of trips in the road network according to equilibrium assignment technique which function according to Wardrop's first principle [5]. Modal split is ignored in this case due to the fact that vehicles are converted into unit vehicles.

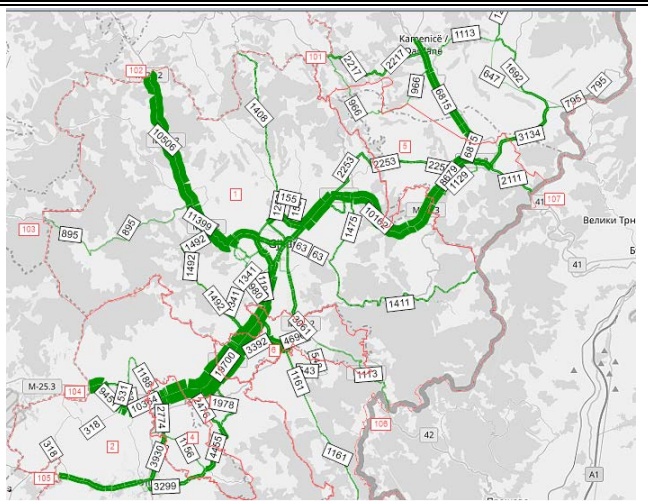


***Figure 6.** Traffic demand according to current situation*

6.4 Traffic volume at specific roadside locations

Once modelling process is applied in PTV Visum software synthetic model is gained which does not describe all trips from one zone to another. This is expected due to the lack of data road network design, lack of attributes in software etc. In this regard there were no studies of this kind accomplished before so that data could be used to compare traffic volume.

This is the reason why this research has been undertaken to count and interview traffic flow at eight locations within and in the surrounding of Anamorava region.

This research enabled to do counting and interviewing traffic participants according to "face to face" principle. For its completion initially forms for counting and interviews are designed which contain the following: the date and time, location of interview, occupation, and transport mean used for travelling, direction of trip (O-D), purpose of trip, frequency of trips, number of passengers in vehicle, etc.

Following the aim of trips hereunder are trips: external–internal, internal–external, internal–internal and transit traffic.

Traffic conducted within one zone was not subject of survey and all trips qualified as such were not taken into consideration.

This field survey is facilitated by students of the Faculty of Mechanical Engineering – Traffic and Transport Department assisted by Kosovo Police Service. Some locations in roadside are identified to be with dominant flow of vehicles and students were assigned to places to conduct counting and interviewing. Counting and interviews were completed simultaneously on 18.05.2016 and 21.05.2016 and continuously for 12 hours from 07:00 a.m. until 19:00 p.m.

As a result, there were 11 523 interviews completed, comprising 19.43% of total traffic volumes, and also showing 59 317 vehicles counted manually. Accurate position of roadside locations is shown in Figure 7.

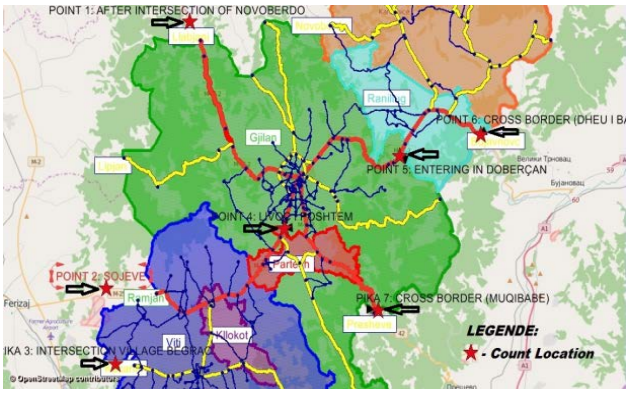


Figure 7. *Locations of counting and interviews*

Data collected are processed by MS Excel. It is obvious that there was not possible to interview every traffic participant and for this reason in order to get general number of vehicles travelled through each location interviewing coefficient K_{int} is used as an average of two days as given by Eq. (3):

$$K_{\text{int}} = \frac{VOL_{12}}{I_{12}} \tag{3}$$

Where:
K_{int} - coefficient of interview,
VOL_{12}- number of vehicles counting in 12 hours' time interval and
I_{12} - number of interviews in 12 hours' time interval.

Table 5 reflect values of this coefficient separately for each roadside location.

Table 5: *Interview coefficient for each roadside location*

No.	Location	VOL_{12}	I_{12}	%	K_{int}
1	Slivovo	5494	1131	18.01	4.86
2	Sojevo	5981	1092	15.42	5.48
3	Begraca	3137	880	24.23	3.56
4	Kllokot	4749	925	17.73	5.13
5	Dheu i Bardhe	1148	278	57.43	4.14
6	Ranillug	5350	894	16.47	5.99
7	Livoc i Poshtem	7173	1354	18.41	5.30
8	Muqibabe	571	115	59.62	4.96

In this regard, by application of this coefficient is gained traffic volume for an interval of 12 h, by applying Eq. (4):

$$VOL_{12h} = I_{12} \cdot K_{\text{int}} \qquad (vehicle/12h) \tag{4}$$

Where:
VOL_{12h}-traffic volume realized by vehicles in time interval 12 h.

In order to find out traffic flow expressed as AADT it was applied converting coefficient K_{con} from 12h to 24h by Eq. (5).

$$K_{con} = \frac{VOL_{24}}{VOL_{12}} \tag{5}$$

Where:
K_{con} - converting coefficient of traffic from 12h to 24h,
VOL_{24} –traffic volume by MTC counting in time interval 24h and
VOL_{12} –traffic volume by MTC counting in time interval in 12h.

Traffic flow counting for the period of 12h and 24h is done using mobile automatic traffic counting (MTC) in four locations as presented in Figure 8 for an entire week counting and registering vehicles passed doing at the same time also manual counting and interviewing.

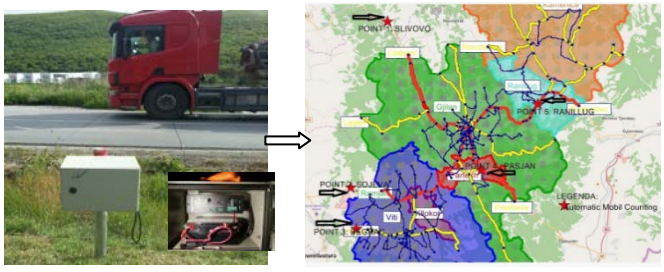


Figure 8. *Locations of Mobil Traffic Counting (MTC)*

After processing of data on the traffic volume by MTC for the period of 24 hours there was the possibility to get converting coefficient from 12h into 24h, as expressed in Table 6.

Table 6. *Converting coefficient K_{con} from 12h to 24 h*

Location	Day	Date	Manual Counting	Mobile Counting	Ratio	Average
Slivovo	W	18.05	5396	8526	1.58	1.49
	S	21.05	5396	7829	1.40	
Ranillug	W	18.05	5592	8022	1.50	1.42
	S	21.05	5348	7119	1.33	
Gap	W	18.05	5353	11120	1.52	1.55
	S	21.05	7316	11036	1.57	
Sojevo	W	18.05	7029	9666	1.49	1.51
	S	21.05	6487	8320	1.52	

Days in week: W-Wednesday, S-Saturday

Thus, taking into account four locations and two week days, given coefficient should be an average for all of them and it results to be $K_{con(12h/24h)}=1.5$. By application of coefficients K_e, K_{int} and $K_{convert(12h/24h)}$ it was possible to get flow of vehicles travelled during the period of 24 h, by Eq. (6):

$$AADT_{24h} = VOL_{12} \cdot K_e \cdot K_{\text{int}} \cdot K_{con} \quad (vehicle/24h) \tag{6}$$

Where:
$AADT_{24h}$–traffic volume realized by vehicles in time interval 24h.

Seasonal coefficient K_s and weekly nonlinear coefficient K_w are ignored since counting and interviews are done for two days in May of 2016 and average values are taken into consideration. May month is taken as reference because it was verified that the seasonal coefficient got the $K_s=1$.

3. Discussion results and calibration

After development of synthetic model and the values gained by field counting, comparison is done for traffic volumes modelled and those observed which are based on the counts in each location of the main network, as presented in Table 7 and Table 8.

Due to incompatibility FlowFuzzy algorithm technique is applied for correction and adjustment of data measured and modelled. This works according to the approach given in Figure 9 [14].

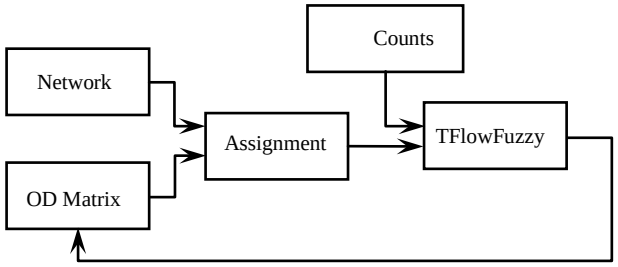


Figure 9. *TFlowFuzzy for the correction of the initial synthetic model*

Based on literature [15], the criterion for model calibration of traffic model is fulfilled if $GEH<5$ on 85% of all locations taken into account and coefficient of determination ($R^2>0.85$).

Given indicators are used to measure the scale performance of approximation of results and it provides an indication of the error of a model. The calculation of values of the GEH test, which takes into account the difference value obtained according to the model vs. observed. GEH test can be calculated by Eq. (7), as follows:

$$GEH = \sqrt{\frac{2 \cdot (O_i - M_i)^2}{(O_i + M_i)}} \tag{7}$$

Where:
O_i-value obtained by observed, M_i-value obtained from the model.

In Table 7 and 8 in summary is the comparison of traffic volumes of traffic measured and modelled expressed as AADT levels according to *GEH test*, R^2 and *percentage deviation*.

Results by the Tabs 7 and 8 below shows that the GEH index for all roadside locations, except for location No. 28 are lower than

5 (GEH<5). Based on this result it is obvious fulfilment of GEH<5 on 85% of all locations that are taken into consideration

Table 7: *Summary of GEH test indicators*

Evaluation aggregate	
GEH: Avg.	*2*
GEH: <5.0	*86%*
Deviation: Avg.	*3%*
Deviation: Avg. weighted	*4%*

Table 8: *Presentation of results of GEH test*

Link		Census	Model	Evaluation	
Number	*From nodes*	*Count [veh/24]*	*Volume [veh/24h]*	*% – Deviation*	*GEH*
28	*109*	*13 123*	*14 009*	*6%*	*5.5*
28	*110*	*12 960*	*11 932*	*-8%*	*6.7*
88	*225*	*1999*	*1938*	*-3%*	*1*
88	*339*	*2166*	*2073*	*-4%*	*1.5*
92	*8*	*10 178*	*10 119*	*-1%*	*0.4*
92	*11*	*11 411*	*11 223*	*-2%*	*1.3*
145	*403*	*5210*	*5273*	*1%*	*0.6*
145	*404*	*4326*	*4264*	*-1%*	*0.7*
921	*309*	*9916*	*10 309*	*4%*	*2.8*
921	*739*	*9397*	*8997*	*-4%*	*3*
1048	*607*	*10 004*	*9836*	*-2%*	*1.2*
1048	*827*	*9831*	*10 125*	*3%*	*2.1*
1071	*278*	*918*	*960*	*4%*	*1*
1071	*843*	*1159*	*1155*	*0%*	*0.1*

In order to verify the quality of calibration, the coefficient of determination (R^2) is also used. The referred literature [16] show that the value of this coefficient is approaching to 1 and this is an indicator that there is compliance of results compared which is in this case the result of traffic volume according to the model and to the field counting. A value from 0.9 to 1 is considered acceptable.

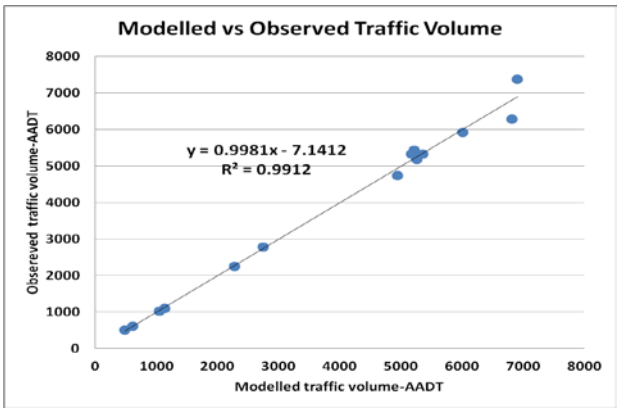


Figure 10: *Demand model according to counting and interviews*

In the above graphics, the relation between this characteristic is expressed also by equation y=0.9981x-7.1412. This value is R^2=0.9912, which means that the value as such is exceptionally good.

4. Conclusion

Initially in this study synthetic model is developed on traffic demand for Anamorava region. This is done using demographic and social-economic variables and the traffic volumes on the "peak hour" as an input to PTV Visum software.

The outcome of this model is the traffic volume expressed as AADT on the main road network of this region.

According to this model the traffic demand was not described enough for the main road network and this is why additional research is undertaken to accomplished counting and interviews in order to get real traffic volumes for certain location of this network. Once given data is collected they were processed through application of correction coefficient so that traffic volumes expressed as AADT, and consequently comparison is done.

In order to get a satisfactory distribution of traffic volumes for the road network TFlow Fuzzy algorithm technique is used. Verification of results related to fulfilment of criterions is done by GEH test, R^2 and percentage deviation indicators. All these indicators resulted to meet threshold suggested by literature.

Based on results gained it was obvious that the final model is suitable and as such it may be used to forecast the traffic demand for this region.

This model may also be used by competent institutions in drafting transport strategies and other relevant studies related to Anamorava region.

5. References

[1] Kutz, M. Handbook of Transportation Engineering, Volume II: Applications and Technologies. McGraw-Hill Professional, Second Edition, 2004.

[2] Zdenek, R. & Dytrych, J. Peak-period Models and 24-hour Models Comparison. Proceedings of the 2nd International Conference on Environment, Economics, Energy, Devices, Systems, Communications, Computers, Mathematics (EDSCM'12), 175-180, 2012.

[3] Luburić, G., Šoštarić, M. & Slavulj, M. (2011). Measuring of Transit Traffic in Cities. Technical Gazette, 18(4), 619-625. https://hrcak.scrce.hr/75412.

[4] Kosovo Census Atlas. Geographic and Administrative Division of Kosovo, ASK, Prishtina, 2013.

[5] Ortuzar, J. & Willumsen, L. Modelling Transport 4th Edition. Chichester: Wiley, 2009.

[6] TRB, Highway Capacity Manual 2010. Transportation Research Board-Special Report 209, Edition 2010.

[7] PTV Vision Visum 15 User's Manual.

[8] Yatskiv, I.; Savrasov, M.: Development of Riga-Minsk transport corridor simulation model. Transport and Telecommunication, Volume 11, No. 1, 38-47, Latvia, 2010.

[9] General Statistics of Kosovo ASK, Prishtina, 2014.

[10] Grujić, A. & Jokanović, I. Classification and Categorization of State Roads – Comparative Analysis of Regulations. Proceedings of Papers of Civil Engineering Faculty of Subotica, No.22, 159-171, 2013.

[11] Atanasova, V., Angelevska, B., Krstanoski, N. & Cvetanoski, I. Calculation of Transport Demand by Applying Software PTV Vision Visum. International Scientific Journal. Machines, Technologies and Materials (MTM). Issue 3, Sofia, Bulgaria, 2017.

[12] Mikolaj, J. & Remek, L. Traffic Flow Modelling based on ISOHDM Study. Proceedia Engineering, Vol.111, 522-529. doi:10.1016/j.proeng.2015.07.126, 2015.

[13] Haxhipetkovska, K. Creation of Macro Model for Transport Demand for City and Region. Master Thesis. University "St Kliment Ohridski" Faculty of Technical Sciences Bitola, Macedonia, 2015.

[14] PTV AG. How to work with TFlow Fuzzy. Official Manual, PTV Vision Visum, Karlsruhe, 2008.

[15] TII Publications PE-PAG-02015. Project Appraisal Guidelines for National Roads Unit 5.1 – Construction of Transport Models. Transport Infrastructure Ireland (TII), 2016.

[16] Friedrich, M.; Nökel, K.; Mott, P.: Keeping Passenger Surveys Up to Date: A Fuzzy Approach, Transportation Research Records, No. 1735, pp. 35-42, 2000.

RESEARCH INTO THE EFFECT OF CERTAIN CHEMICAL ELEMENTS IN MICROALLOYED STEEL GRADES ON CONCAST SLAB AND ROLLED PLATE SURFACE QUALITY

O. Isayev, O. Hress, S. Yershov, M.Q. Huang, K.L. Zhang

The State Key Laboratory for Refractories and Metallurgy, Hubei Province Key Laboratory of Systems Science in Metallurgical Process, International Research Institute for Steel Technology, Wuhan University of Science and Technology, Wuhan 430081, China
e-mail gunung1961@mail.ru

Abstract: *Investigators has developed a complex technology of manufacture of high quality skelp and shipbuilding grades and nickel-, chromium-, molybdenum-, niobium- and vanadium- microalloyed steels with carbon mass fraction within 0.06% to 0.22% and manganese mass fraction within 1.0% to 1.7%. Over the course of the research, relative occurrence of surface cracks of various morphology – transverse, longitudinal, spider, net-like – on the concast slab surface has been determined. The above research resulted in the development of a number of technological innovations both in preparation of liquid steel for casting and in continuous casting itself, preventing initiation or reducing by 30% – 40% the amount of surface defects on the rolled plates.*
KEY WORDS*: PERITECTICAL STEEL GRADES, CHEMICAL COMPOSITION, CASTING TECHNOLOGY*

Introduction

The experience of prime steel production made it possible to find out that the surface of a concast slab and consequently that of plate steel under certain conditions has a number of defects like cracks of different morphology – cross, longitudinal, net-like and star cracks.

Experimental

A complex procedure of plate steel production of prime steels for large diameter gas line pipes, shipbuilding and steel structures of critical application microalloyed with niobium wherein carbon weight fraction. is in the range of 0.06 to 0.22% and manganese weight fraction – 1.0 to 1.7% was developed and implemented at the Iron and Steel Works. Steel was made in 350 t converters and put to ladle treatment at the metal-refining plants with introduction of silicocalcium wire. Continuous casting was done at curvilinear slab concasters into 220…300 x 1550…2100 mm section slabs as to a worked-out procedure.

Chemical composition of the steel grades studied is shown in Table 1.

Table 1. *Steel chemical composition*

Steel grade	Application	Elements weight fraction, %							
		C	Mn	Si	S	P	Al	Nb	V
08MnNb	Skelp	0.06–0.09	1.00–1.35	0.15–0.35	max 0.006	max 0.020	0.020–0.050	0.020–0.040	0.015–0.035 Ti
09Mn2VNb	Skelp	0.08–0.11	1.50–1.70	0.15–0.35	max 0.006	max 0.020	0.020–0.050	0.020–0.040	0.050–0.070
13Mn1SiNb	Skelp	0.12–0.15	1.30–1.60	0.40–0.60	max 0.007	max 0.025	0.020–0.050	0.020–0.040	0.015–0.035 Ti
ASTMA572	Structure	0.12–0.16	0.80–1.00	0.15–0.35	max 0.015	max 0.020	0.020–0.060	0.005–0.020	–
S355J2G3	Structure	0.16–0.19	1.40–1.60	0.15–0.40	max 0.015	max 0.020	0.020–0.050	0.020–0.040	–

* - other elements are in the range specified by standards for residual content

.

For a more serious study of concast slabs affected with surface defects, determination of factors conducive to crack formation process and elaboration of practices aimed at reducing defect occurrence, surface templates were cut from middle slabs of 5 to 10 heats of the above-mentioned BOF shop current production steel grades. To reveal surface defects the said templates were put to hot etching with 50% aqueous solution of hydrochloric acid. The evaluation of surface quality was done as per the current scales and procedure of researches institutes. Evaluated were the slab wide face surfaces corresponding to the smaller and larger concaster radii (in percentage) and the extent of defect development (severity evaluation system).

In the course of the study relative affection of the concast slab with surface cracks was determined. Each typical concast slab defect, unless revealed and rectified, gets transformed into plate steel surface defects. Slabs with revealed and identified defects were selected for rolling to study concast slab surface defects transformation into plate steel surface defects. Slab rolling was done at 3600 mm Plate Mill as per conventional procedure of slab preheating and rolling.

Results and Discussion

Based on the results of rolling slabs having surface defects transverse cracks 0.5 to 3.0 mm deep as per the folds of the mould oscillation were found to get transformed depending on the gauge of plates, into rolling skin of specific appearance – so called "μ - defects" having the depth of penetration of up to 0.03 mm (vide fig.1). Longitudinal cracks having the depth of 0.5 to 3.5 mm get transformed into skin spread along rolling direction to a considerable length resembling so-called "streaks". Check cracks 0.5 to 3.0 mm deep and star cracks, 3.0 to 10.0 mm deep after rolling plates look like randomly oriented skins and cracks with different depth of penetration (vide fig.2).

Metallographic studies revealed certain regularity between steel product quality indexes and steel chemical composition and, accordingly, between polymorphous transformations of iron-carbon alloy with a number of alloying elements being used.

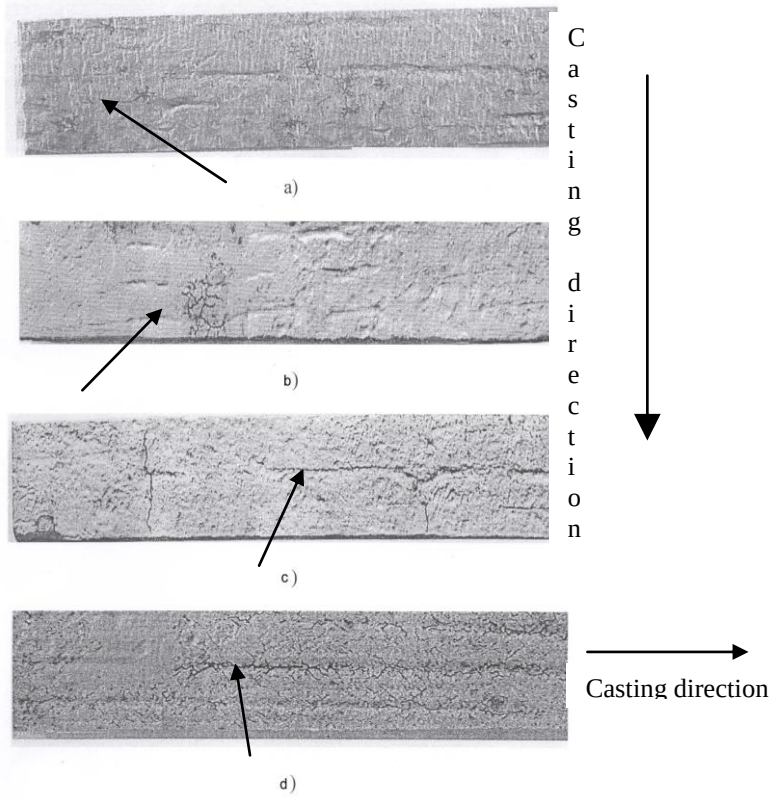


Fig. 1. *Typical slab surface defects.*
a – "star" cracks; ; b – netlike cracks; c – transversal cracks; d – longitudinal cracks

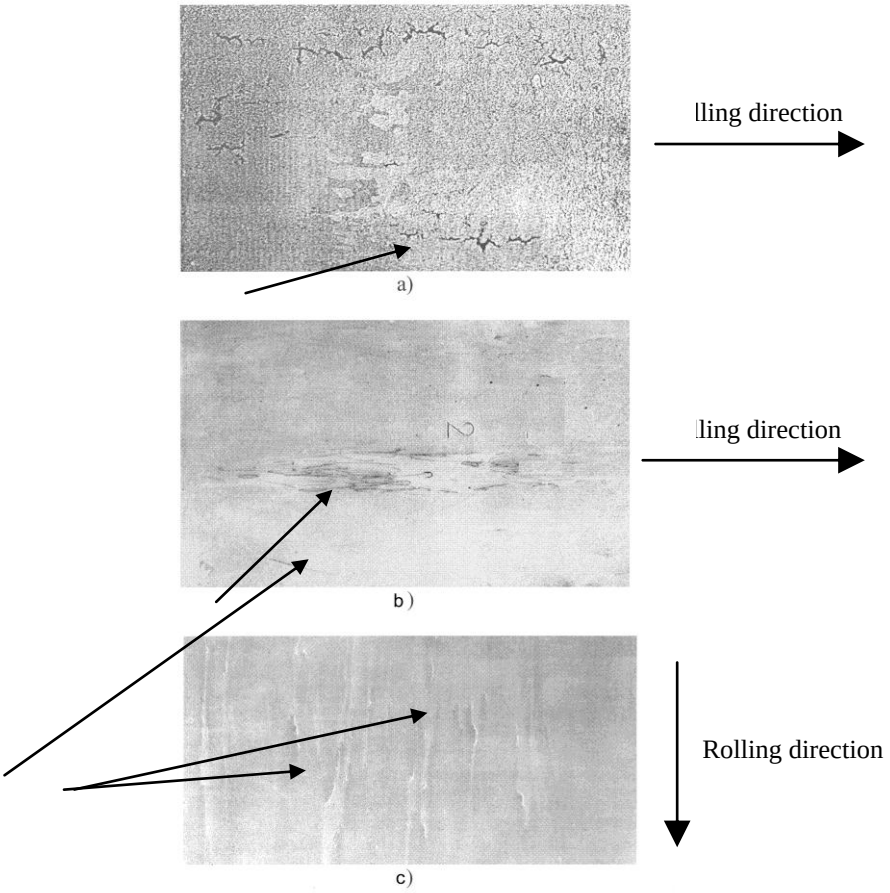


Fig. 2. *Transformation of slab defects to rolling plates.*
a – netlike cracks; b – rough scab; c – shallow scab ("µ"-defect).

Carbon content impact

In the course of study observed was an obvious tendency of crack number increase per unit of area and the degree of their development with an increase of carbon content in the examined range of carbon content changes – from 0.07% to 0.21%. The integral value of the defect-stricken surface of slab of steel grade 08MnNb with carbon content being 0.06 ÷ 0.09% was taken for a unit of crack formation conventional index. The crack formation conventional index takes into account both the value of the slab surface affection with cracks and the crack depth penetration.

Simultaneously it was observed that along with carbon concentration change from 0.09% to 0.21% surface crack morphology undergoes certain changes – at carbon weight fraction being in the range of 0.10 ÷ 0.14% check cracks are prevalent, while at carbon content being 0.15–0.21% there was a considerable amount of transverse and star cracks observed along with check cracks.

Analysis of the Fe-C diagram at carbon weight fraction in steel being within 0.08 to 0.45% shows presence of 3 principally different areas of the melt solidification. Comparing the data of the table and the Fe-C diagram it was noted that steel grades 08MnNb and 09Mn2VNb solidification takes place in the area where there's a transition from δ-iron to γ-iron in the completely solidified metal.

For steel grades 13Mn1SiNb and ASTMA572 having δ-γ transition in accordance with the standard interval of carbon content there's a provision both for a variant of transition into a completely solidified metal and for a variant of peritectic transformation from "δ+liquid" to "δ+γ" at constant temperature. For steel grades S355J2G3 or St52.3 the following variants of solidification are possible: "δ+liquid" into "δ+γ" or "δ+liquid" into "γ+liquid". Under such conditions the factors, which usually play unimportant role, have significant influence on quality indexes of the surface of metal. To these factors should be referred minor fluctuations of hot metal level in the mould while casting steel at a concaster, inessential moisture deviations and deviations of granulometric slag-forming composition (within the limits stated by normative documents), technological deviations of casting rate related to changes of submerged nozzles, tundishes etc.

Based on the results of the study, considering that carbon weight fraction in steel affects consumer qualities of finished metal product to a large extend, the Works' specialists focused their special attention to such steel grades, that were most susceptible to defect formation processes. As a result, a whole series of engineering measures and corrective actions both in the field of preparation of liquid steel for casting and directly at concasting of steel were worked out to avoid or to reduce essentially defect formation processes essentially.

Manganese content impact

It was established that, fraction of surface defects had steady tendency to increase with growth of manganese weight fraction in steel, which was confirmed with essentially greater number of defects on the surface of steel 13Mn1SiNb and 13Mn1Si (manganese content up to 1.6%) in comparison with steel grade ASTM A572 (manganese content up to 1.0%). It was found, that with increase of manganese weight fraction in steel in 0.05% in the range of 1.2% to 1.8% of manganese content defect-stricken surface of the concast billet increased approximately in the same value according to linear dependence. In addition, it was found that most unfavorable conditions of billet skin formation in the mould at casting steel are observed for the grades, whose solidification was possible under various variants so-called peritectic steel grades – 13Mn1SiNb and S355J2G3.

Aluminum and nitrogen content impact

The impact of such elements as aluminum and nitrogen was put to the study too. As a result of these elements emission at grain boundaries in the form of aluminum nitride ALN metal ductility in the temperature interval of embrittlement while casting steel of peritectic type decreased. It promotes the formation of small-sized longitudinal cracks at the temperature of slab surface of 700–900°C, that corresponds to the area of a billet unbending at the concaster secondary cooling zone (curvilinear area), where slab crust is put to considerable fluctuating load. As a result of transformation of this type of defects at rolling, shallow skins were formed, which are situated mostly at side area at a distance of up to 300 mm from the plate edge. Based on the results of the study it was stated, that minimal propagation of longitudinal cracks was formed at nitride content less than 0.006% and aluminum weight fraction in the range of 0.029–0.032%.

Impact of impurities of nonferrous metal

Taking into account, that peritectic steels are susceptible to crack formation initially rather topical question is the issue of rating of impact of impurities of nonferrous metals on quality of concast slab and plate products. It is generally known that residual impurities of nonferrous metals have a harmful effect on the quality of cast and rolled metal. At the analysis of effect of impurities of nonferrous metals on quality indices an essential influence of the increased concentrations of nonferrous metals was marked on: 1) formation of the rough cross cracks in some cases resulting in destruction of slabs; 2) formation of cracks perpendicular to a wide side or narrow and face sides of a slab; 3) increase of a rejecting of plate steel regarding surface defects of steelmaking and the defects revealed with the ultrasonic control (presence of internal cracks in the center line area of a sheet).

A thorough investigation and analysis of the manufacturing method of the slabs, undergone to destruction was carried out: 1) in the slab yard of the BOF shop; 2) during transportation or transfer; 3) at reheating in the furnace before rolling; 4) during rolling.

It is necessary to note, that the fact of slabs destruction at a rough cross crack occurs rather seldom. So, a number of the destroyed slabs at all stages (conversions) in the last years came to 5.5 cases / 100 thousand of slabs. It was noted, that exclusively manganese steel microalloyed with niobium or steel fully alloyed with niobium and vanadium, first of all steel grades: St52.3 under DIN 17100 or S355J2G3 under EN 10025 (about 90%) were susceptible to destruction.

The formed crack in overwhelming number of cases passes all over the dendritic-web areas. In the area of a break small-sized stress cracks depart from the basic crack. Microfractographic study was carried out on a focused-beam electronic microscope REMMA-202M and to show, that destruction of samples basically was characterized by fragile destruction of grain boundaries. It confirmed the statement about embrittlement at grains boundaries due to nonferrous impurities.

According to the carried out studies determined were the maximum permissible impurities concentrations: for lead – 0.0003–0.0004%, for antimony – 0.0003%, for tin – 0.0005–0.0006%, for zinc – 0.0020–0.0030%. It was established, that the degree of effect on increase of crack sensibility decreases in the following order «antimony-lead- tin-zinc». Based on this, the empirical formula determining the given total limiting concentration of impurity of nonferrous metals, not rendering visible deterioration of properties of cast and rolled metal of manganese steels with carbon content 0.17–0.22% is offered: C_M = %Sb + 0,75%Pb + 0,5%Sn + 0,1%Zn ≤ 0,0012, where C is the given total concentration of nonferrous metals in finished steel.

At excess of the given "threshold" value expansive growth of deterioration continuous cast slabs – occurrence of rough transverse cracks on the surface of narrow and wide sides of an billet, face cracks perpendicular to wide sides is observed. In most critical cases (for steels with carbon content in the range of 0.18–0.21% of 78 and manganese more than 0.01%) destruction of slabs or presence of a main cross through-the-thickness transverse crack of plate steel is observed.

"Threshold" value $C_м$ increases with simultaneous decrease of the carbon and manganese content. During studies it is marked, that for steel with the carbon content in the range of 0.17–0.21% at increase by carbon in 0.01% "threshold" value of the given factor

$C_м$ should be decreased by 0.0004%. At excess of "threshold "values" $C_м$ for steels with carbon content in the range of 0.10–0.11% and manganese more than 1.6% or with carbon content 0.14–0.16% and manganese in the range of 1.0–1.2% face cracks perpendicular to wide sides at the worst are observed.

Hydrogen impact

Not less essential effect on quality of a surface of concast slab is rendered by availability of the dissolved hydrogen in steel. Change of a heat sink from a mold wall to a solidified billet skin is the factor resulting in formation of the above-mentioned net-like check and star cracks. This assumption is confirmed by calculation of the amount of hydrogen releasing at steel solidification and its getting into the hit in a liquid layer of slag at the copper wall of a mould.

It's from the known published sources that the data for the equilibrium value of hydrogen solubility in liquid steel was taken to be within the limits of 26 ppm near the liquid point and within 8 ppm near the solidus in solid δ-iron. The thickness and length of a liquid slag interlayer was taken for calculations to be respectively 2–3 mm and 600–700 mm, a reference value of hydrogen concentration in solid steel over equilibrium concentration to be 4 ppm. For case of short periods of time it's possible to assume that up to 2 ppm of hydrogen are released from the solid shell of an billet into the liquid interlayer of slag. Taking into account low sorption ability of slag on the basis of and the initial moisture content in the mix to be within 0.4 – 0.5% it is pertinent to make the assumption that hydrogen released from steel forms bubbles floating up to the surface of slag. The greatest possible amount of the released hydrogen in the way of bubbles is comparable to the volume of the whole liquid interlayer of slag. Simultaneously nonuniform hydrogen allocation along the perimeter of billet can be the additional factor that breaks a uniformity of a heat-conducting path and accordingly results in initiation of concast billet surface defects both on wide and narrow sides of billet.

Development of corrective actions

Taking into consideration that a fracture of total mass of a number of elements contained in steel is defining the consumer properties of finished steel products, particular attention was paid to those steel grades that are to the utmost susceptible to the defect forming process. In the course of work several technological innovations were generated both in the field of liquid steel preparation for casting and directly in the process of continuous casting thus allowing to avoid or essentially minimize negative affect of the unstable processes of crystallization and solidification.
A number of measures were worked out at several Works to significantly improve slab surface quality. In case of possible change in steel chemical analysis, not contradicting the regulatory documents, the content of carbon was changed towards minimization.

Several technological measures were suggested for steels with strict specification of chemical composition (in particular, by carbon content): 1) use of recycled low sulphur scrap only in steel melting and primary aluminum for steel deoxidation; 2) optimization of the granulometric composition of slag-forming mixtures for concasting of steel and in a number of cases use slag-forming mixtures of the molten base for the purpose of improving the slag-forming process on the surface of melt in the mould and conditions of heat abstraction between the mould wall and the slab crust; 3) application of special "mild" secondary cooling mode to melt slab steel grades 13Mn1Si and 13Mn1SiNb to decrease thermal stress in the solidifying rim of the slab; 4) slow cooling slabs of steel grade S355Nb slabs including cooling in boxes to reduce internal macro stresses in cast steel.

Found that changing of the heat sink conditions under unsteady casting conditions has negative effect on solidification of steel undergoing peritectic transformation. In that case unsteady solidification process facilitates extension of lap depth and crack initiation of different morphology – transverse, netlike and spider cracks – on the billet surface. Increasing of mixture viscosity due to mixture temperature reduction at metal mirror and billet surface results in slag pulling into billet subsurface layer. Reduction or full stoppage of metal feeding to the mold during transient process leads to almost complete liquidation of compelled upflows in steel and facilitates nonmetallic inclusions entanglement among growing dendrite axis from the direction of CCP minor radius. Reduction of slag layer temperature and billet temperature is a reason of saturation of liquid slag layer with the bubbles of hydrogen escaping from billet and heat sink abrupt change at local points. Reduction of billet surface temperature in unbending zone towards brittleness temperature interval is a reason of initiation or propagation of surface cracks originated in the crystallization zone both on the narrow and broad billet edges.

Essential increasing of concast slabs rejection due to surface defects and downgrading of rolled plates manufactured from the slabs cast under irregular condition is a confirmation of the above mentioned negative factors effect. Rejection of the slabs cast under transient condition due to surface defects is 1.5 – 2 times more than that during casting under stabilized condition. For example, "pipe" defect is detected only under transient condition. At the same time plate downgrading due to the defects discovered with the help of ultrasonic testing, according to 2^{nd} – 3^{rd} class of SEL 072 standard and similar to it, increases 3 – 5 times more. Rolled metal downgrading due to the skins and slag impurities is increasing 2 – 3 times more.

Casting process under irregular condition increases essentially hazard of off-optimum and emergency situations at the CCP. As example of such negative influence is increasing of billet skin sticking index and bleeding index under the mould. Sticking and bleeding index while casting of the first slab's meter after nozzle exchange is 20 – 30 times more, while casting of the second – third meter is 15 – 20 times more than while casting under stabilized condition. Each case of casting under irregular condition leads to a great amount of technological crops such as teeming arrests, both top and ground scraps, scrap in the form of metal remains in tundish while tundish exchange or the termination of the casting process.

One of the possible solutions of the question of casting speed and temperature stabilization is decreasing of transient conditions quantity. It permits to increase the average casting speed to obtain the reduction of crop and metal quality improvement.

Most of the transient conditions, such as submerged nozzles replacement and tundish replacement, finishing of the casting process are related with limited life time of the casting refractory materials such as stopper rod, no swirl nozzle and submerged nozzle. Increasing of refractory components resistance and, hence, the number of heats a series is one of the important conditions of concast billet quality improvement.

With the purpose to reduce the rate of defects in a concast slab, the usage of rational by chemical composition refractory materials, with more than 1.2% manganese mass fraction, for steel casting was introduced at some Iron and Steel Works. Mullite-graphite submerged nozzles were selected as having higher mechanical wear resistance and low sensitivity to manganese interaction. The usage of stopper rod monoblock units and argon blowing of the no swirl nozzle at the rate 0.1 – 0.2 m^3/hr, which prevents inclusion deposition on work surfaces was suggested for the purpose of steel castability improvement and decrease of non-regular conditions during casting.

More difficult question was a selection of optimal casting refractory materials for casting of ordinary peritectic steels, such as carbon and manganese steel with up to 1.2% Mn content. While casting steel of this type, it is possible to use both quartz submerged nozzles less sensitive to the process of alumina particles deposition on refractory work surfaces and high strength mullite-graphitic submerged nozzles. Three different types of casting refractory complete sets were used for comparative experiments: 1) option 1 – jointed stopper rod, biceramic no swirl nozzle and quartz submerged nozzle with steel silicocalcium treatment of the most important steel grades at argon stirring plant; 2) option 2 – jointed stopper rod rod, periclase-graphite nonswirl nozzle and quartz

submerged nozzle with steel silicocalcium treatment of all grades at argon stirring plant; 3) option 3 – stopper rod monoblock unit, periclase-graphite or corundum-graphite no swirl nozzle and mullite-graphite submerged nozzle with steel silicocalcium treatment for all grades at argon stirring plant;

200–300 heats of ordinary carbon grades or low alloy steel grades with manganese content up to 1.2% were made for each option. The process waste quantity during casting (scrap, crop), casting process stability (stopper rod "no closing", metal penetration into the gap between the no swirl nozzle and the stopper rod, choking of submerged nozzle channel, concast billet and rolled plate quality were evaluated. The main parameters of steel casting process and technological waste quantity are given in Table 2.

Table 2. *Casting technological parameters*

Position	Parameters, conventional index	Production option		
		1	2	3
1	Tundish, heat life time	1	1.06	1.56
2	Nozzles life time	1	1.87	6.40
3	Casts in unstable conditions	1	0.63	0.16
4	Stopper rod pair faults	1	0.70	0.06
5	Crops	1	0.85	0.65
6	Scrap	1	0.76	0.72
7	Slab rejection due "gas blister" defect	1	0.56	0.44

The usage of high strength casting refractories together with steel silicocalcium treatment of all grades is fully reasonable.

As the result of the testing, we recommended to abandon the usage of biceramic no swirl nozzles and to use periclase-graphite or corundum-graphite nonswirl nozzles, which have mechanical erosion resistance and are insensitive to alumina deposition on working surfaces. Additionally, with the purpose of abatement of alumina particles deposition, it is recommended to treat all low-carbon steels with silicocalcium core wire. In this process, complex fusible combinations of calcium and aluminum oxides that do not deposit on refractory surface are formed.

All the measures developed and represented in this paper allowed to reduce essentially the quantity of transient casting conditions and off-optimum situations in slab casting.

Introduction of the above research results in casting of carbon and manganese steels of peritectic grades with manganese content up to 1.2% allowed: 1) to increase tundish life time 1.4 – 1.5 times; 2) to increase submerged nozzle life time 3.5 – 6; 3) to decrease 10 – 15 times the number of stopper rod pairs and submerged nozzle faults; 4) to decrease the technological waste quantity 13 – 15 times; 5) to decrease 1.3 – 2.3 times slab downgrading due to "gas blister" defect; 6) to decrease 2.1 times plates downgrading due to steelmaking defects.

Research results of unsteady steel casting conditions influence

The unsteady casting condition impact on concast billets and rolled plates internal and surface defects initiation and propagation are studied. It is demonstrated that concast slabs rejection due to surface defects and rolled plates downgrading due to steelmaking defects and defects indicated by ultrasonic testing essentially increase under unsteady conditions, the probability of non-regular and emergency situations (specifically, concast billet sticking) occurrence increases substantially.

Technological actions that facilitate stabilization of casting speed and temperature by reduction of solidification transient conditions are recommended: reduction of submerged nozzles replacements and increasing of tundish and number of heats in a series.

Usage of optimal refractories with the aim to reduce the possibility of transient conditions occurrence in continuous casting is suggested. This method implies the usage of mullite-graphite stopper rod monoblock units with stopper rod channel argon blowing, periclase-graphite or corundum-graphite no swirl nozzles and mullite-graphite submerged nozzles. The usage of refractories proposed allows to reduce occurrence of unsteady conditions and their negative impact on the complex indicators of concast slab and rolled plates quality.

References

1. Бережницкий Л.Т., Громяк Р.С., Трущ Н.И. О построении диаграмм локального разрушения хрупких тел с остроконечными жесткими включениями // ФХММ.- 1975. – 11, №5. – С. 40-47.

2. Harkogard G.A. A theoretical study of the influence of inclusions upon the initiation and growth of fatigue cracks in steel // Jernkontorets annaler.- 1991.- 155, N6.- P.209-297.

3. Трефилов В.И., Моисеев В.Ф. Дисперсные частицы в тугоплавких металлах.- Киев: Наук.думка, 2008.- 240 с.

Briant C.L., Banerjee S.K., Ritter A.M. The role of nitrogen in the embrittlement of steel // Met.Trans.- 1982.- A13, N7.- P.1939-1951.

4. Драчинский А.С., Подрезов Ю.М., Трефилов В.И. Влияние элементов структуры на энергию межзеренного разрушения // ФММ.- 1983.- 55.- Вып.1.- С.157-164.

5. Столофф С.Н. Влияние легирования на характеристики разрушения // Разрушение.- М.: Металлургия, 1976.- 6.- С.11-89.

6. Бродецкий И.Л., Белов Б.Ф., Позняк Л.А., Троцан А.И. Влияние адсорбционных процессов в границах зерен на хладостойкость низколегированных сталей // ФХММ.- 2005.- №2.- С.124-128.

7. Бродецкий И.Л., Харчевников В.П., Троцан А.И., Белов Б.Ф. О влиянии кальция на зернограничное охрупчивание сталей с карбонитридным упрочнением // МиТОМ.- 1995.- №5.- С.24-26.

8. Бродецкий И.Л., Харчевников В.П., Троцан А.И. Анализ неметаллических включений на границах зерен стали с карбонитридным упрочнением //МиТОМ.-2004.- №3.-С.12-14

9. Control of Surface Ouality of 0.08%<C<0.12% Steel Slabs in Continuous Casting / Vincent Guyot, J.-F. Martin, A. Ruelle e.a //ISIJ International, Vol. 36. - 1996.- Supplement, P. S227-S230.

10. Mazumdar S., Ray S.K. Solidification control in continuous casting of steel // Sadhana, Vol. 26, Parts 1 & 2, February–April 2001, P. 179–198.

EVALUATION OF MECHANICAL PROPERTIES OF DUCTILE CAST IRON AND INVERSE REGRESSION

ОЦЕНИВАНИЕ МЕХАНИЧЕСКИХ СВОЙСТВ ЧУГУНА С ШАРОВИДНОГО ГРАФИТА И ОБРАТНАЯ РЕГРЕССИЯ

Assoc. Prof, PhD. Alexander Popov [1], PhD. Mr. Eng. Jan Ivanov [2] , Br. Eng. Stefan Georgiev [2]
[1] Institute of Mechanics - BAS, Sofia, Bulgaria, E-mail: alpopov@abv.bg
[2] M+C HYDRAULIC Plc, Kazanlak, Bulgaria, E-mail: jeanivanov@yahoo.de

Abstract: *The evaluation of ductile cast iron is common foundry practice. For the correct non-destructive evaluation (NDE) of mechanical properties (ultimate tensile strength; relative lengthening; Brinell's hardness; elasticity modulus) by means ultrasonic testing and inverse regression analysis are used.*

Kay words: MECHANICAL PROPERTIES, DUCTILE CAST IRON, INVERSE REGRESSION

.

1. Introduction

The ultrasonic testing of the mechanical properties of ductile cast iron [1,2,3] is a common practice in M+C HYDRAULIC.

There are methods of regression analysis are used. In literature there are dependencies between the structural characteristics of the cast iron $(F;P;N_G)$ and its mechanical properties $(E;\nu;N_G;R_m;HB)$, where $(F;P;N_G)$ are appropriate *F*,% - quantity of ferrite and *P*,% - quantity of perlite in the metal matrix, N_G ,% - nodular graphite contain; R_m - ultimate tensile strength; A_5 - relative elongation; *HB* – Brinell's hardness; $(E;\nu)$ - elasticity modulus. The following dependencies are considered [4-11]

(1) $(E;\nu)\Rightarrow(V_L;V_T)$;

(2) $N_G=\eta(V_L)$;

(3) $R_m=\gamma_0+\gamma_1.V_L$; $\quad R_m=\beta.V_L^2.HB$;

(4) $A_5=A_5^{(0)}+A_5^{(1)}.V_L$; $A_5=a.(M.V_L^2/HB)^m$;

(5) $HB=h_0+h_1.V_L$,

where $(V_L;V_T)$ are velocities of longitudinal and transversal ultrasonic waves [8,11]. The coefficients in (2)-(5) $\gamma_0;\gamma_1;\gamma;A_5^{(0)};A_5^{(1)};a;M;h_0;h_1$ are subject to determination and depend on the casting technology and the type of graphite in the casting. The dependencies (2) to (5) are regressions models from type

(6) $(N_G;R_m;A_5)=F(V_L;HB)$

In regression analysis [12] the basic principle is " $(F;P;G)$ defines by $(N_G;R_m;A_5;HB)$", where $(F;P;N_G)$ - microstructure characteristics of, $(N_G;R_m;A_5;HB)$ - mechanical properties for ductile cast iron. In this sense, dependencies (2) to (5) are incorrectly. The correct approach is

(7) $V_L=\Psi(N_G;R_m;A_5;HB)$,

where $(F;P;G)\Rightarrow V_L$. In this article the models with one predictor $X=\chi(N_G;R_m;A_5;HB)$ and order n are considered [12]

(8) $V_L=\sum_{K=0}^{n}\beta_K X^K$.

The condition for choice, at *X* = 1, of order m, is $R^2\rightarrow\max$, where R^2 is coefficient of determination.

Table 1.

m	R^2
$m=1$	$R^2\equiv R^2(m=1)$
$m=2$	$R^2(m=2)\approx(1.05\div1.10).R^2$
$m=3,4,5$	$R^2(m=3,4,5)\approx(1.06\div1.13).R^2$
$m\geq6$	The regression matrix is badly determined.

If $m=1$, then the values of R^2 are relatively low. If $m=2$, then the values of R^2 are rises with $\sim(5\div10)$%. If $m=3;4;5$, then the values of R^2 are rises $\sim(1\div3)$% and efforts to calculate it are not justified. If $m\geq6$, then the regression matrix is badly determined and calculations are not made.

Therefore, the optimal choice of the model (8) is one predictor $X\Leftrightarrow(N_G;R_m;A_5;HB)$, and model order m = 2.

2. Relations for ductile cast iron

2.1. Deterministic dependencies

In the theory of elasticity [10,11] is obtained (9)

$$V_L=\sqrt{\frac{1-\nu}{(1+\nu).(1-2.\nu)}}.\sqrt{\frac{E}{\rho}},$$

where the elasticity modulus $E;\nu$ respectively are Young's modulus and Poison's coefficient, density of ductile cast iron - $\rho, kg/m^3$. The deterministic dependence (9) is reduced to

(10) $E=M(\nu).V_L^2$,

where

$$M(\nu)=\rho.\frac{(1+\nu).(1-2.\nu)}{(1-\nu)},\nu=\frac{0.5-(V_T/V_L)^2}{1-(V_T/V_L)^2}.$$

For most ductile cast iron, the reference values for ν are $\nu\in(0.23\div0.28)$. In fact, for ductile cast iron, Poisson's coefficient changes to a very narrow boundary. By means

reference values $med(\nu)=0.25$, $\rho=7.31kg/m^3$, M = 6.092 is obtain. Therefore, the dependence (10) is reduced to

(11) $E \approx 6.V_L^2$.

2.2. Stochastic dependencies

According the experimental data, for ductile cast iron, from M+C HYDRAULIC a polynomial models of (8) are considered

(12) $V_L = \sum_{K=0}^{2} \beta_K X^K$,

where $X \equiv (N_G; R_m; A_5; HB)$, $(\beta_0; \beta_1; \beta_2)$ subject to determination. It are direct regression problems.

The inverse regression problems are determine the confidence intervals $(X_L; X_R)$, when V_L is measured. The equations for $(X_L; X_R)$ are [12]

(13) $\mp \chi(X_{L,R}) + V_L = 0$,

where

$\chi(X_{L;R}) = t.S.\left[\frac{1}{n} + \frac{1}{S_{XX}}\left(X_{L;R} - \overline{X}\right)^2\right]^{1/2} - \sum_{K=0}^{2} \beta_K X_{L;R}^K$, number of measures – n, $S_{XX} = (n-1).S$, $(t, S, \overline{X})$, by means Excel, MS Office are obtain.

The equations (13) are non-linear regarding $X_{L;R}$ and solved by the Newton's method using a ZEROIN algorithm [11], on-line C ++ compiler, at a specified root spacing. The ZEROIN algorithm is resistant and fast approaching.

3. Equipment

Image Analyzer Buehler Omnimet, Digital Ultrasonic Flaw Detector Sitescan 150S, Tensile machine Testometric F300, Hardness tester TIII- 2M.

4. Experiment

Ten samples were made with varying percentages and graphite morphology and mechanical properties. They were determined for them $(N_G; R_m; A_5; HB)$ and $(V_L; V_T)$. Morphology of graphite (N_G) was determined with a Buehler Omnimet image analyzer at an 8x image magnification. The mechanical properties $(R_m; A_5; HB)$ are determined by mechanical testing. The velocities $(V_L; V_T)$, Fig.1. , according ASTM E 494:2015 are calculated.

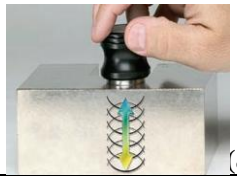
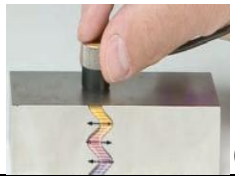
Piezo plate with X – cut for longitudinal waves with velocity V_L	Piezo plate with Y – cut for transversal waves with velocity V_T
 (a)	 (b)

Fig.1. Ultrasonic L-waves (a) and T-waves (b)

5. Inverse regression tasks

5.1, Polynomial models

According the experimental data, for ductile cast iron, confidence intervals $(X_L; X_R)$, are obtained.

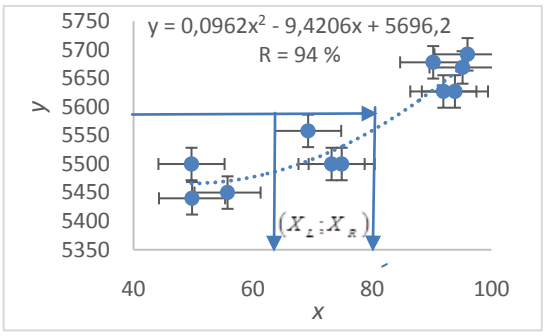


Fig.2. $(x = N_G, \%; y = V_L, m/s)$

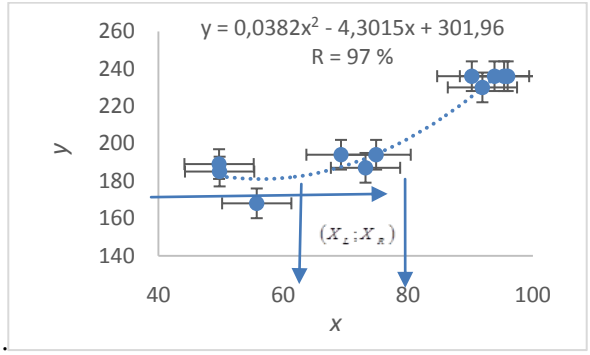


Fig.3. $(x = N_G, \%; y = HB, kgf/mm^2)$

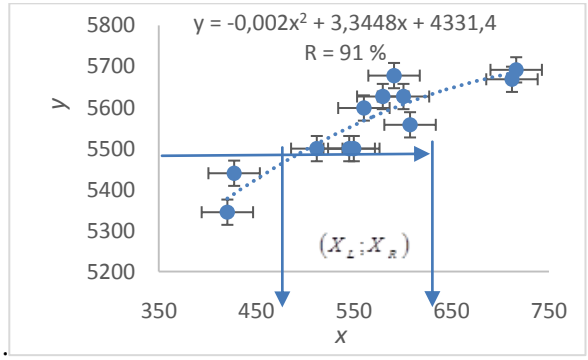


Fig.4. ($x = R_m, MPa; y = V_L, m/s$)

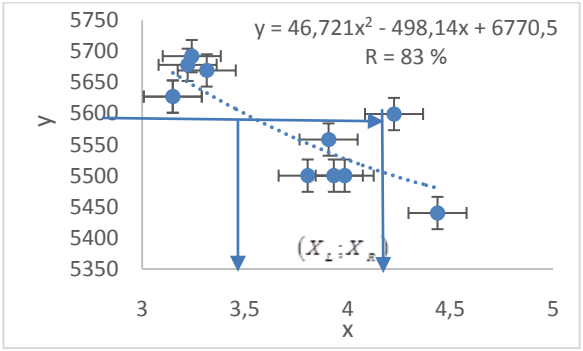


Fig.5. ($x = A_5.\%; y = V_L; /s$)

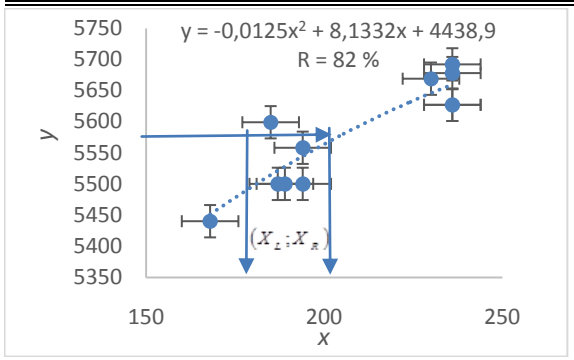


Fig. 6. ($x = HB, kgf/mm^2; y = V_L.m/s$)

5.2. Hybrid models

The introduction of hybrid models in the regression analysis is based on the following assumption. Factor combinations depend on one predictor [4-11]. For example $F(V_L;HB) = A_5$ and $\Psi(V_L;HB) = R_m$. Such an approach is expected R^2 will rise. On Fig. 7. and Fig. 8. specific dependencies are given.

.

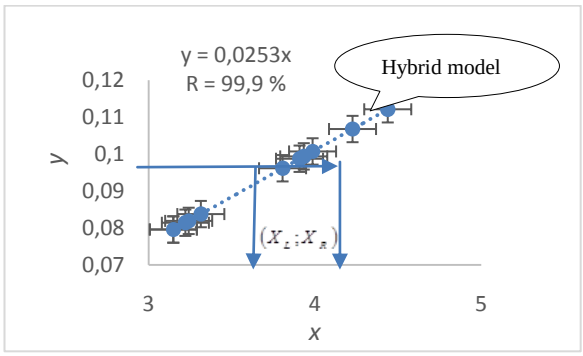


Fig. 7. ($x = A_5, \%; y = 6(V_L^2 / HB)^{4/3}$

.

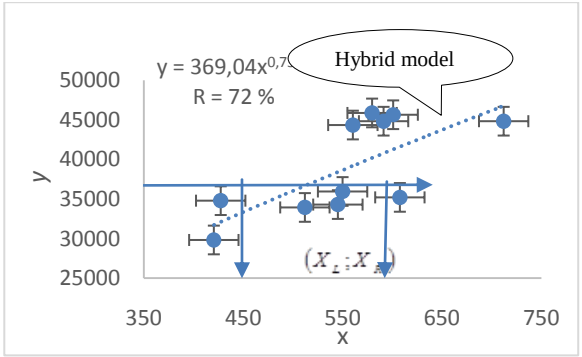


Fig.8. ($x = R_m, MPa; y = 6.V_L^2.HB$)

6. Results

For data from M+C HIDRAULIC Plc the results of inverse regression analysis in Tables 2 - 8. are given. When comparing the results of (Fig.2.) and (Fig.3.), it appears that using the model from (Fig.2.) has less scattering gives a little narrower boundaries evaluation of N_G , %. In this sense, the use of the model from (Fig.2.) is slightly better than the model from (Fig.3.).

Table 3.

A / Polynomial models			
95% probability confidence intervals, $(V_L;V_T)$ for *NDE* of N_G ,% by V_L ,m/s and by *HB* ,kgf/mm^2 *Rm, MPa*, A_5 , *%, HB,* kgf/mm^2 by V_L ,m/s			
-	Characteristics of ductile cast iron	(X_L)	(X_R)
Fig.2.	N_G (V_L)	~ 64	~ 81
Fig.3.	N_G *(HB)*	~ 65	~ 80
Fig.4.	*Rm* (V_L)	~ 470	~560
Fig.5.	A_5 (V_L)	~ 3.6	~ 4.4
Fig.6.	*HB* (V_L)	*~ 175*	*~ 213*

Median values are V_L , m/s =5850; *HB,kgf/mm*^{2}=194.

Table 4.

B / Hybrid models			
95% probability confidence intervals, $(V_L;V_T)$ for *NDE* of A_5 *%* , *Rm, MPa* by $\Psi(V_L$,m/s; *HB* ,kgf/mm^2)			
-	Characteristics of ductile cast iron	(X_L)	(X_R)
Fig.7.	A_5 $(V_L;HB)$	~ 3.8	~ 4.1
Fig.8.	*Rm* $(V_L;HB)$	~ 465	~ 595

Median values are V_L , m/s =5850; *HB,kgf/mm*^{2}=194.

7. Conclusion

The paper examined the possibilities and constructed correct models for assessing the degree of ductile iron spheronization and mechanical properties
by measuring the velocity of propagation of longitudinal ultrasonic waves and Brinell hardness. The numerical values of the coefficients of the models were obtained as well as the coefficients for their determination. For this purpose, the respective inverse regression tasks are solved.

8. References

1. Anderson J.C., K.D. Leaver, R.D. Rawlings, J.M. Alexander, Materials Science, Chapman and Hall, London, 1990
2. Guliaev A.P., Material Science, Metalurgia, Moscow, 1986, (In Russian).
3. Arzamatov B.N., &, Materials Science, MGTU "N.E.Bauman", Moscow, 2003, (In Russian).
4. Ivanushkin E.S., G.S. Belay, Ultrasonic Testing of Castings, Technika, Kiev, 1984, (In Russian).
5. Popov Al., Inverse Problems in Solid Mechanics and Ultrasonic Testing , Series "Applied Mathematics and Mechanics", Vol. 9, Institute of mechanics - BAS, Sofia, 2018. (ISSN: 1314-3034), (In Bulgarian).
6. Litovka V.I., Improving the quality of high-strength cast iron in castings, Naukova dumka, Kiev, 1987 (In Russian).

7. Aleshin N.P., &, Acoustical methods for metal testing, Mashinostroenie, Moscow, 1989. (In Russian).
8. Voronkova L.V., Ultrasonic Testing Possibilities of Cast Iron Ingots, Th.2.2.3., ECNDT 2006, Roma, Italy.
9. Hanza S.S., D. Dabo, Characterization of cast iron using ultrasonic testing, Journal of Cr S NDT, No 18, p.3-7, ISSN 1847-9340, 2017
10. ASTM E 494:2015, Standard Practice for Measuring Ultrasonic Velocity in Materials.
11. Sokolnikov I. V., Mathematical theory of elasticity, Nauka i izkustvo, Sofia, 1972 (In Bulgarian).
12. Draper N.R., Smith H., Applied regression analysis, v.1.,v.2.,Finansi i statistika, Moscow, 1986, (In Russian).
13. Forsythe Dj., M Malcolm, K. Molar, Computer methods in mathematical calculations, Nauka i Izkustvo, Sofia, 1986, (In Bulgarian).

THE INFLUENCE OF NATURAL AGING AND PRE-AGING ON THE MECHANICAL, PHYSICAL AND MICROSTRUCTURAL PROPERTIES OF THE EN AW-6060 ALUMINUM ALLOY

MSc. Stamenković U., Prof. Dr Ivanov S., Assist. Prof. Marković I., Prof. Dr Mladenović S., Prof. Dr Manasijević D., Prof. Dr Balanović Lj.
University of Belgrade, Technical Faculty in Bor, Bor, Serbia

ustamenkovic@tfbor.bg.ac.rs

Abstract: *The aim of this paper is the investigation of the effect of natural aging on the mechanical, physical and microstructural properties of an EN AW-6060 aluminum alloy. These properties were investigated during different aging treatments. Firstly, the effect of natural aging on properties was investigated, after which the influence of natural aging (room temperature pre-aging) on the artificial aging was studied. The results showed the beneficial effect of natural aging in both sets of experiment. During the natural aging, the hardness increased for around 20 % while electrical conductivity values were slightly higher than in the quenched sample. The hardness of the samples gradually increases up to 25 days of natural aging reaching a plateau state, after which the values of hardness remain the same. Also, room temperature pre-aging had a positive effect on subsequent artificial aging. Samples that were pre-aged for 40 days or more before artificial aging had around a 13 % increase in hardness values compared to the samples that were directly artificially aged. Electrical conductivity had increased by around 1 MS/m in pre-aged samples compared to only artificially aged samples. Optical microscopy investigations confirmed the existence of precipitated phases and their distribution in the microstructure.*

Keywords*: ALUMINUM ALLOYS, EN AW-6060, NATURAL AGING, ARTIFICIAL AGING, HARDNESS, ELECTRICAL CONDUCTIVITY, MICROSTRUCTURE, PRE-AGING*

1. Introduction

Mechanical properties of metallic materials are often improved by various heat treatments. In order to strengthen aluminum alloys, age hardening process is used. This process includes solution heat treatment, quenching to room or below room temperature and aging, which can be either natural (performed at room temperature) or artificial (performed at higher temperatures) [1, 2]. The aging process is responsible for the formation of very fine and evenly dispersed particles that hinder the movement of dislocation thus strengthening the alloy through Orowan mechanism [2]. To attain deeper knowledge of the aging process it is very useful to know the precipitation sequence of investigated alloys. The precipitation sequence is usually found by DSC analysis with combination of some other characterization methods. The largely accepted precipitation sequence for Al-Mg-Si alloys which was found by other authors is given as: α_{ssss} → Mg:Si clusters→ G.P. zones→ β''→ β'→ Si (if excess silicon is present)→ β [3-9]. Precipitates given in this sequence appear at different temperatures and affect the structure differently. Natural aging, as it is performed at room temperature, can only produce the clusters of dissolved elements. In the case of EN AW-6060 alloy the most important clusters are that of Mg and Si, as they are the ones that affect structure the most [10]. The effect of natural aging on the mechanical properties can be summarized as either a positive or a negative one. Low-alloyed alloys or often called lean alloys in this series of aluminum alloys often exhibit the positive effect. This means that natural aging leads to an increase in mechanical properties and also higher peak-aged hardness can be achieved after room temperature pre-aging [11-14]. The negative effect occurs in high solute alloys used in automotive and construction industries [1, 2, 15, 16]. The influence of natural aging is still studied, regardless of numerous studies. In this paper the lean alloy from 6xxx series was investigated (EN AW-6060). The aim was to better understand the influence of natural aging and room temperature storage (pre-aging) on hardness, electrical conductivity and microstructural changes. Also, the investigation of positive or negative effects on subsequent artificial aging was performed.

2. Materials and design

Experimental investigation was performed on EN AW-6060 alloy. The alloy was delivered by "AlCu metali d.o.o." company, in peak aged condition (T6 temper) in the form of extruded rectangular bars. The Table 1 represents the chemical composition of the investigated alloy determined by the optical emission spectrometer "Belec Compact Port". Annealing at 550 °C for 6 hours in the electric resistance furnace Heraeus K-1150/2 removed peak aged condition and obtained the O-temper for all of the samples. After that, solution heat treatment was performed at the same temperature for 1 hour followed by quenching in water with ice in order to obtain a super saturated solid solution (α_{ssss}). After obtaining the super saturated solid solution, the samples were subjected to natural aging for a different time from 3 up to 70 days (referenced as NA samples). One sample was directly aged without any room temperature delay in order to achieve peak hardness state (presented on graph as directly aged AA samples). In order to investigate the influence of natural aging on artificial aging (AA), samples that were naturally aged for 3, 10, 40 and 70 days were chosen and artificially aged in the same manner as the directly aged sample (those samples are referenced as NA+AA samples). All the NA samples were compared to the quenched sample (quenched state on the presented graphs), while all the NA+AA samples were compared to only the artificially aged samples (AA samples).

Table 1: *Chemical composition of the investigated alloy (mass. %)*

Si	Fe	Cu	Mn	Mg	Cr	Ni	Zn
0.49	0.182	0.012	0.006	0.594	<0.003	0.028	0.01
Ti	**Pb**	**V**	**Co**	**Sn**	**Zr**	**Al**	
0.005	<0.003	0.014	<0.003	<0.003	<0.003	98.62	

During the aging treatment, all samples were subjected to various characterization methods. Electrical conductivity was measured using the electrical conductivity tester Sigmatest 2.063". Hardness was measured on the VEB Leipzig Vickers hardness tester using a 10 kg load and a 15 s dwelling time. The ASTM E384 standard was followed during the hardness measurements [17].

3. Results and discussion

Analysis of the graph presented in Fig. 1 shows that hardening was achieved through natural aging. All of the naturally aged samples had higher hardness values in comparison to quenched state. After only 3 days of natural aging hardness rapidly increases, and continues to increase until it reaches hardness saturation after which the curve shows the plateau state where hardness remain almost the same up to 70 days. Hardness has a maximum value after 40 days of aging. This value is around 20% higher than the value for the quenched sample.

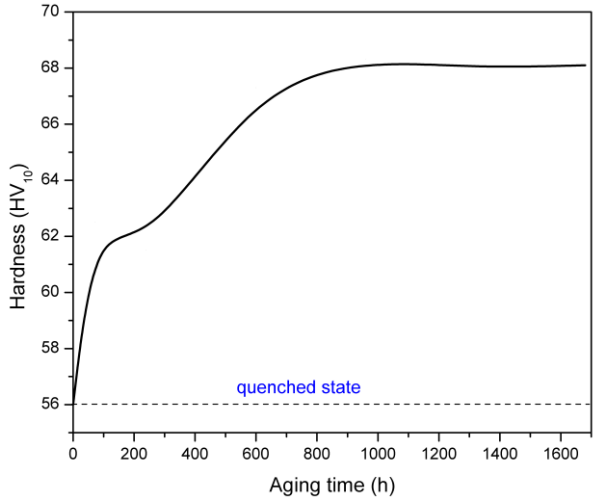


Fig. 1 *Hardness variations of quenched samples during natural aging of EN AW-6060*

During solution heat treatment, Mg and Si atoms dissolved into the Al matrix and remained in the matrix after quenching. Hardness increment was possible due to the formation of magnesium and silicon clusters and co-clusters caused by precipitation during the natural aging process. This formation is causing the restriction of dislocation motion and increasing the hardness of the alloy [1, 2, 10, 16]. The incline of the curve presented in Fig. 1 can be explained by the formation of Mg and Si clusters which occurs after several hours of natural aging discovered through 3D atom probe by L. Cao et al. [18].

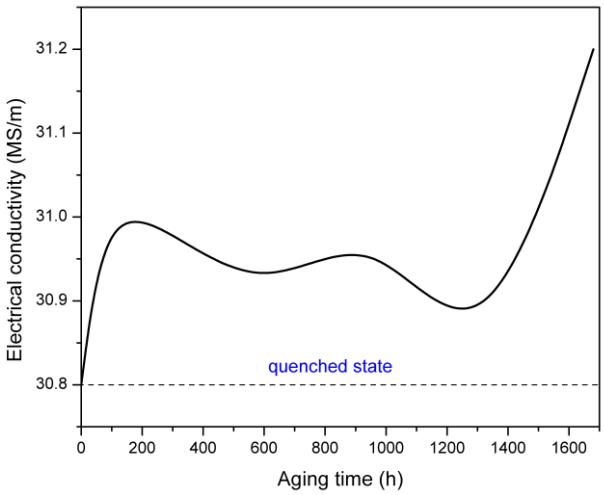


Fig. 2 *Electrical conductivity variations of quenched samples during natural aging of EN AW-6060*

The influence of natural aging on the electrical conductivity of the investigated alloy is presented in Fig. 2. From Fig. 2 it can be concluded that all of the NA samples exhibit slightly higher values of electrical conductivity in comparison to the quenched samples. Electrical conductivity increase can be expected knowing that during natural aging clusters and co-clusters are formed. The quenched solute atoms are released from the super saturated matrix in the form of clusters and co-clusters. This formation is responsible for relaxing the matrix and promoting the free movement of electrons, thus increasing electrical conductivity. The increase in electrical conductivity is not very large due to the fact that this is a lean alloy so the amount of formed clusters cannot have much impact. Usually these clusters have a strong electron scattering effect that can lower the electrical conductivity, but in our case that was not detected [7, 19, 20].

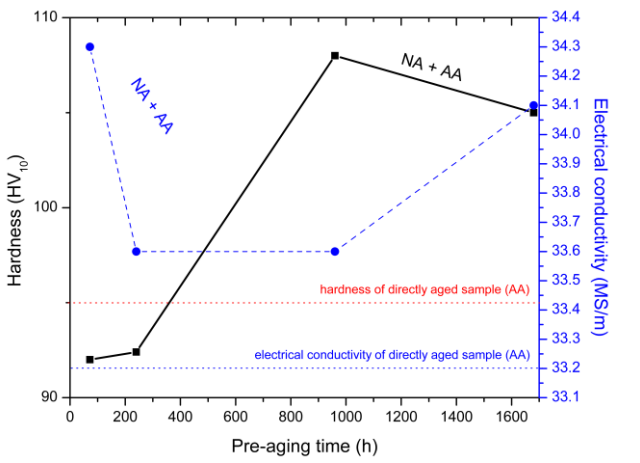
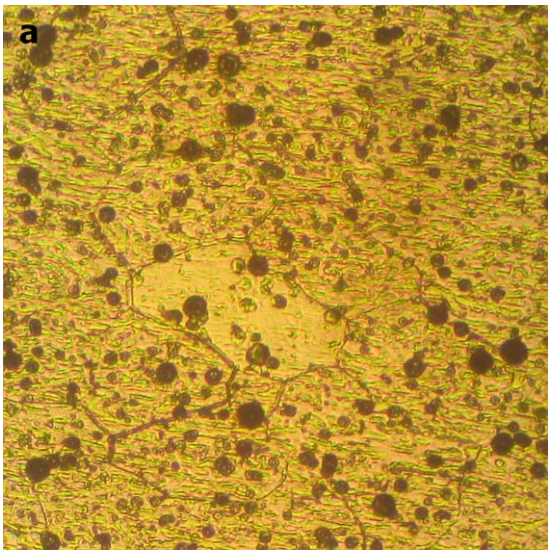


Fig. 3 *The influence of pre-aging on artificial aging on hardness and electrical conductivity of investigated alloy*

In Fig 3 the influence of natural aging (room temperature pre-aging) on the artificial aging has been presented. From the presented graphs in Fig. 3 it can be seen that in both cases, hardness and electrical conductivity, pre-aging had a positive effect on subsequent artificial aging. In order to obtain the highest hardness values the samples need to be peak aged. For the highest values of hardness in peak aged samples the β'' phase is responsible. Any stimulation of the precipitation of this phase results in higher hardness values. In the case of lean Al alloys, clusters and co-clusters formed during the pre-aging help the nucleation of the β'' phase in later precipitation during artificial aging [11, 14]. Samples that were pre-aged for 3 and 10 days had somewhat lower values of hardness in comparison to directly aged samples. In these samples, due to a short period of pre-aging, the nucleation of the β'' phase was not as much affected. Samples pre-aged for 40 and 70 days had enough time to form enough clusters of Mg and Si to stimulate the nucleation, hence the hardness values are higher in comparison to the directly aged ones [2, 6, 10, 11, 14, 15]. In the matter of electrical conductivity, all of the values are higher in the pre-aged samples in comparison to the directly aged sample. This can be ascribed to larger precipitation due to pre-aging and stimulation through nucleation of the β'' phase.

The formation of clusters and the stimulation of precipitation through nucleation sites, caused the β'' phase to appear in the microstructure as finely dispersed particles on the grain boundaries and in the grains, as shown in Fig 4a-b.



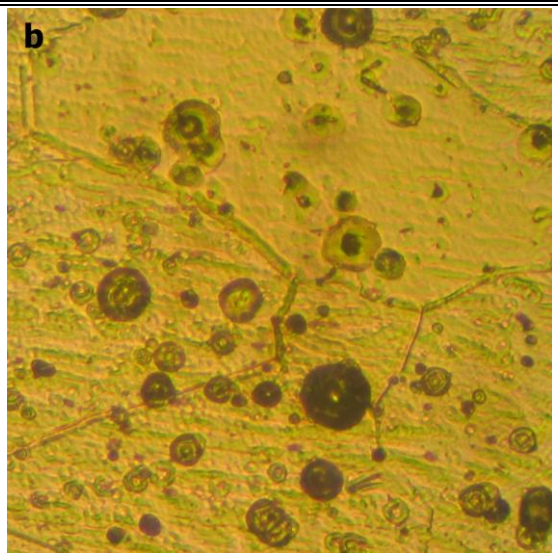


Fig. 4 *Microstructure of the sample naturally aged for 40 days and then peak aged for maximum hardness value; a) magnification x200; b) magnification x500*

4. Conclusions

The influence of natural aging on hardness, electrical conductivity and microstructure was investigated. Key conclusions can be outlined:

- The hardness of the samples naturally aged is higher than those in the quenched state. Maximal hardness is achieved after 40 days of natural aging, after which the hardness goes into the plateau state and hardness remains the same until 70 days of natural aging.
- Naturally aged samples have slightly higher values of electrical conductivity in comparison to the quenched one.
- Natural aging showed positive effect on artificial aging.The nucleation of the β'' phase and the strengthening effect of β'' phase was affected by the formation of magnesium and silicon clusters and co-clusters. The hardness of the pre-aged samples was higher only in the ones pre-aged for 40 and 70 days. Hardness was higher for around 13 % for the pre-aged sample in comparison to the directly aged one. Electrical conductivity was higher in all of the pre-aged samples when compared to the only artificially aged one.
- In the samples that were naturally and subsequently artificially aged, β'' phase appeared in the form of finely dispersed particles.

Acknowledgements

The research results were developed with the assistance of the Ministry of Education, Science and Technological Development of the Republic of Serbia under the projects OI 172037 and TR34003.

References

[1] Pogatscher S., Antrekowitsch H., Leitner H., Ebner T., Uggowitzer P.J., Mechanisms controlling the artificial aging of Al–Mg–Si Alloys - Acta Materialia, Volume 59 (2011), pp. 3352-3363.

[2] Cuniberti A., Tolley A., Castro Riglos M.V., Giovachini R., Influence of natural aging on the precipitation hardening of an AlMgSi alloy - Materials Science and Engineering: A, Volume 527 (2010), pp. 5307–5311.

[3] Milkereit B., Wanderka N., Schick C., Kessler O., Continuous cooling precipitation diagrams of Al–Mg–Si alloys - Materials Science and Engineering: A, Volume 550 (2012) pp. 87-96.

[4] Mrowka-Nowotnik G., Influence of chemical composition variation and heat treatment on microstructure and mechanical properties of 6xxx alloys - Archives of Materials Science and Engineering, Volume 46 (2010), pp. 98-107.

[5] Birol Y., Precipitation during homogenization cooling in AlMgSi alloys - Transactions of Nonferrous Metals Society of China, Volume 23 (2013), pp. 1875-1881.

[6] Gupta A.K., Lloyd D.J., Court S.A., Precipitation hardening in Al–Mg–Si alloys with and without excess Si - Materials Science and Engineering: A, Volume 316 (2001), pp. 11-17.

[7] Edwards G.A., Stiller K., Dunlop G.L., Couper M.J., The precipitation sequence in Al–Mg–Si alloys - Acta Materialia, Volume 46 (1998), pp. 3893-3904.

[8] Shang B.C., Yin Z.M., Wang G., Liu B., Huang Z.Q., Investigation of quench sensitivity and transformation kinetics during isothermal treatment in 6082 aluminum alloy - Materials & Design, Volume 32 (2011), pp. 3818-3822.

[9] Vedani M., Angella G., Bassani P., Ripamonti D., Tuissi A., DSC analysis of strengthening precipitates in ultrafine Al–Mg–Si alloys - Journal of Thermal Analysis and Calorimetry, Volume 87 (2007), pp. 277–284.

[10] Jin S., Ngai T., Zhang G., Zhai T., Jia S., Li L., Precipitation strengthening mechanisms during natural ageing and subsequent artificial aging in an Al-Mg-Si-Cu alloy - Materials Science and Engineering: A, Volume 724 (2018), pp. 53-59.

[11] Chang C., Wieler I., Wanderka N., Banhart J., Positive effect of natural pre-ageing on precipitation hardening in Al-0.44 at% Mg-0.38 at% Si alloy - Ultramicroscopy, Volume 109 (2009), pp. 585-92.

[12] Strobel K., Lay M.D.H., Easton M.A., Sweet L., Zhu S., Parson N.C., Hill A.J., Effects of quench rate and natural ageing on the age hardening behaviour of aluminium alloy AA6060 - Materials Characterization, Volume 111 (2016), pp. 43-52.

[13] Abid T., Boubertakh A., Hamamda S.,Effect of pre-aging and maturing on the precipitation hardening of an Al–Mg–Si alloy - Journal of Alloys and Compounds, Volume 490 (2010), pp. 166-169.

[14] Lai Y.X., Jiang B.C., Liu C.H., Chen Z.K., Wu C.L., Chen J.H., Low-alloy-correlated reversal of the precipitation sequence in Al-Mg-Si alloys - Journal of Alloys and Compounds, Volume 701 (2017), pp. 94–98.

[15] Birol Y., The effect of processing and Mn content on the T5 and T6 properties of AA6082 profiles - Journal of Materials Processing Technology, Volume 173 (2006), pp. 84-91.

[16] Aruga Y., Kozuka M., Takaki Y., Sato T., Formation and reversion of clusters during natural aging and subsequent artificial aging in an Al-Mg-Si alloy - Materials Science and Engineering: A, Volume 631 (2015), pp. 86–96.

[17] Standard Test Method for Microindentation Hardness of Materials, Accessible on Internet: https://www.astm.org/Standards/E384.htm

[18] Cao L., Rometsch P.A., Couper M.J., Clustering behavior in an Al-Mg-Si-Cu alloy during natural ageing and subsequent under-ageing - Materials Science and Engineering: A, Volume 559 (2013), pp. 257–261.

[19] Cui L., Liu Z., Zhao Xi., Tang J., Liu K., Liu X., Qian C., Precipitation of metastable phases and its effect on electrical resistivity of Al-0.96Mg2Si alloy during aging - Transactions of Nonferrous Metals Society of China, Volume 24 (2014), pp. 2266-2274.

[20] Prabhu T.R., Effects of ageing time on the mechanical and conductivity properties for various round bar diamaters of AA2219 Al alloy - Engineering Science and Technology, an International Journal, Volume 20 (2017), pp. 133-142.

MATERIALSCIENCE – MATHEMATICS AND PHYSICS FOR EVALUATION OF LIQUIDS IN FOUNDRY

Chi. Ass. Eng. A. Maheva, PhD., Ass. Prof. Eng. St. Bushev, PhD.,
Institute of Metal Science, Equipment and Technologies With Hydro- and
Aerodynamics Center „Acad. A. Balevski“
Sofia 1574, 67 „Shipchenski prohod“ blvd. Bulgaria
Bulgarian academy of sciences
anna13@abv.bg, stbushev@abv.bg

Abstract *The base process was obtained: 3D hardening temperature field for the K-test under heat transfer at conditions with maximum intensity. A methodology for determining macro-level defects in aluminum alloys. It is definitely the placement of the K-test method in the process of creating the first order phase transition in a casting technology. The idea of interaction between the classical theory of crystallization and quantum mechanics for the processes of structure formation at casting was introduced by Stefan's task in volume with nano-size.*

Keywords: MATHEMATICS, PHYSICS, MICROSTRUCTURE, ALUMINIUM ALLOY, TASK OF STEFAN IN NANO-SPHERE

1. Introduction – mathematical basis of the foundry; material evaluation (metal, alloy (primary, secondary), ceramic casting)

The basic processes of material science are: casting and heat treatment, collectively called die-casting. On Fig. 1 presents a diagram of methodology and connectivity of the most important fundamental scientific areas for high-tech production of the smallest producer (detail).

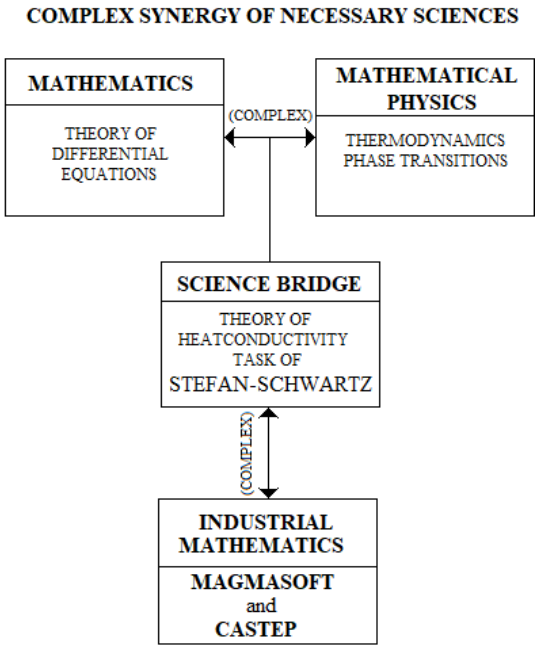


Fig. 1 *Synergy (a complex combination) of high-tech foundry science of a single manufacturer (detail). The connection between mathematics and mathematical physics is a science bridge between software MAGMASOFT [26] and CASTEP (first-principles calculation) [27].*

The working properties of the materials are determined by the structures, which have to describe their creation through the connection between mathematics and mathematical physics from the science bridge (Fig. 1). Fundamental knowledge in industry is used through computational software (Fig. 1).

Mathematics we present in general with work [1] and today it is used everywhere; in research it has become a working language because every science is differentiated through it. Work [2] and the whole development of mathematics has shown that there is no complete (mathematical) mathematics, but it develops itself from an inner necessity without the use of physical experiments. Methods of advancement in theoretical physics are presented in [3]: The principles of quantum mechanics are new ideas observed in experiments and described through mathematical formalism (mathematical theories). The functional link [4] entropy (S) and the probability of the state (π) of the system is eq. of Boltzmann in general with a constant for determining $S = k\ln\pi + \text{const}$, where k is a Boltzmann constant. The difficulty in determining this constant is the separation of the set of dynamic states of the phase space (∞^{2f}), where f – the number of degrees of freedom of the system. Трудностите за определяне на тази константа е разделяне на множеството от динамични състояния на фазовото пространство (∞^{2f}), където f – брой на степени на свобода на системата. Thus (∞2f) is separated into very small cells of the same (hyper-volume) τ: 1. Classical statistical mechanics - indefinite multiplier in π; 2. Quantum mechanics - introduces discrete quantum states: the division of (∞^{2f}) is of cells with hyper-volume hf, where h - the plane of Planck. In [4] is presented the atomic heat capacity based on the Debye temperature quantum mechanics.

Experimentally, a reduction in nanocrystalline Cu and Pd grain size reduction was observed [5].

The material science we present on [6, 7, 8, 9, 10, 11, 12, 13, and 14]: 1. Metal science and hardening [6, 7] - from the electronic structure of the atoms, between atomic bonds, crystal structure, defects and real crystal, properties, X-ray analysis, crystallization and solidification of metals and their alloys; 2. Solid State Theory and Physics of Metal [8, 9, 10, 11,] Atomic view of building-properties from classical physics and quantum mechanics. We note a natural methodological connection from a fundamental point of view between works [6÷11]. Work [12] is an important development for a generalized pattern of strength properties - toughness and resistance to demolition materials; 3. The history of material science is presented by work through separate editions of [13] i.e. a dynamic process of developing learning to teach. We are interested in the theory of alloys. In different editions, the emphasis is on the inclusion of new knowledge of competition in the economy. A problem is a release of knowledge; 4. Principles and system of stereometric metallography methods are presented in [14].

The mathematical experiment is a basic tool besides for research [15] (in pure mathematics discoveries, supporting theorems, and last but not least appraisal of applications [1, 2]). The mathematical experiment was imposed in the industry through the rapid development of mathematical modeling [16]. The [17] is a presentation of the need of using modern computer technology as an active tool in mathematical research. For example, MAGMASOFT is based on modern computer technologies that are constantly being upgraded for high competition. Work is [18] a fundamental example of industrial mathematical physics - nano-particles of gold become corrosively unsustainable. Mathematics is generally a tool that is often stimulated by need for hypothesis assessment and/or predictive discovery (in mathematical and theoretical physics).

Modern Quantum Theory of Solids [19] and modern ideas such as quantum fluctuations and strong electronic correlations. Different topics are dealt with: the general theory of phase transitions, harmonic and anharmonic grids, Bose condensation and superfluidity, modern aspects of magnetism including resonant valence bonds, electrons in metals, and strong electron correlations are seen in terms of ordering and elementary excitement.

The theory of the solid body [20] (or the physics of condensed matter) evolved after the discovery of quantum mechanics. It deals with problems related to materials from **fundamental** to **technological** problems (**quantum mechanics industry**). The progress of industrialized countries is largely a consequence of quantum mechanics [20]. Condensed matter (solids) consists of atomic nuclei (ions) and electrons arranged in an elastic recess. Describe their interaction. Typical scales known from atomic and molecular systems are: Radius length of Bohr; Energy: Hartree with a constant for fine structure. The fundamental theory of common origin of states is sought: electrons interact with each other and through ionic coulombic interaction. Effective (reduced) theories are formulated as an important step (part) of the condensed matter physics of various common Earth states: metal theory, semiconductors, superconductivity.

In [21] are presented the main ideas and methods for the current applications of the variation theory in theoretical physics and chemistry. The known variational principles of classical mechanics and optimization theory are addressed by the variation principles, formalism, and computational methodology of connected and continuous quantum states of interacting electrons in atoms, molecules, and condensed matter

From the works [19, 20, and 21] follows the mandatory use of quantum mechanics in the industry. For example, 34% of the US economy is based on quantum mechanics. The application of quantum mechanics in foundry as a first step in Bulgaria is the methodological proximity of works [6 and 9].

The use of quantum mechanics in the foundry should be from the preparation of the material to the casting and more important structural factors influencing the properties of Al-alloys are [24]: ***macro size of the grains of the solid solution and the state of their boundaries; the amount, shape and temperature of the eutectic crystallization; the amount and size of the secondary phases and their interaction with the solid solution during the heating process***. Physics-chemical properties affecting the casting strength: ***micro-resistance of the solid solution; energetic state of the crystalline lattice of the solid solution (interatomic interaction forces, character state); atomic diffusion coefficient of aluminum and diffusion of the atoms of the alloying elements and impurities in the crystalline grid of the solid solution; quantity and nature of distribution of crystal lattice defects (vacancies, dislocation, impurity atoms) and their interaction with the atoms of the alloying elements***. Quantum numbers are: the quantum number is n and accepts only positive values n = 1, 2, 3, …; an orbital quantum number l = 0, 1, 2, 3, … , n-1, $0 \le l \le n-1$; magnetic quantum number m_i = 0, ±1, ±2, … , ±l, $|m_i| \le l$; spin quantum number s - which occupies only ± 1/2 and defines the moment of impulse of the electron $P_s = \hbar\sqrt{s(s-1)}$. Pauli's principle: In the metal, every possible state of the electron can be occupied by an electron. The electronic state is uniquely defined by the four quantum numbers; there are no two electrons of conductivity with the same four quantum numbers. Not to be taken into account ⇒ Pauli's principle is: each state is described by three quantum numbers and can be encountered twice; it is understood that the two electrons in this state must have the opposite spin. In the electronic gas the impulses p_s (or p) do not have a forward direction, so all p are located within a sphere with max radius p_0 and volume $(4/3)\pi p_0^3$, where p_0 is the maximum impulse corresponding to the energy of Fermi's energy E_0: $E_0 = p_0^2/2m$, where m – electron mass. [10]. The p_0 and E_0 dimensions are defined by Pauli's general quantum theorem: At any state of any z-dimensional system corresponds volume $\hbar^z$ in the phase space (in the impulse space and coordinates). The aim of work is shown in Fig. 2

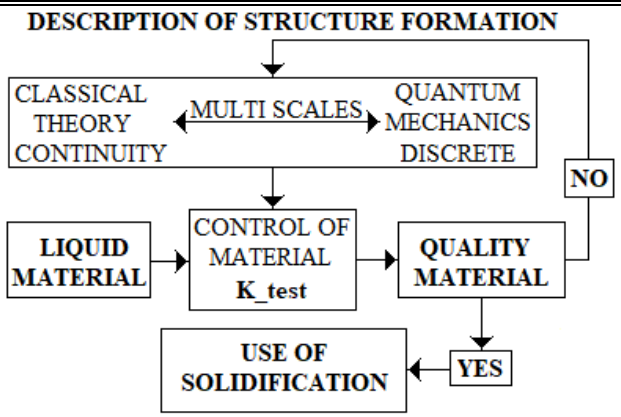
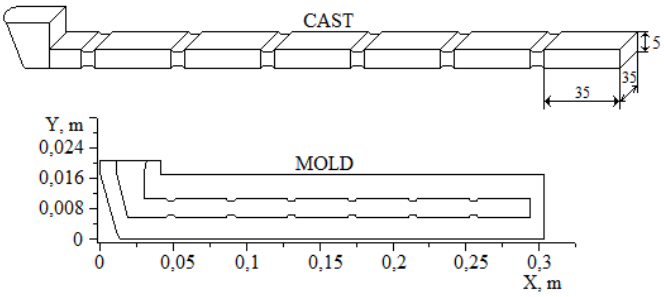


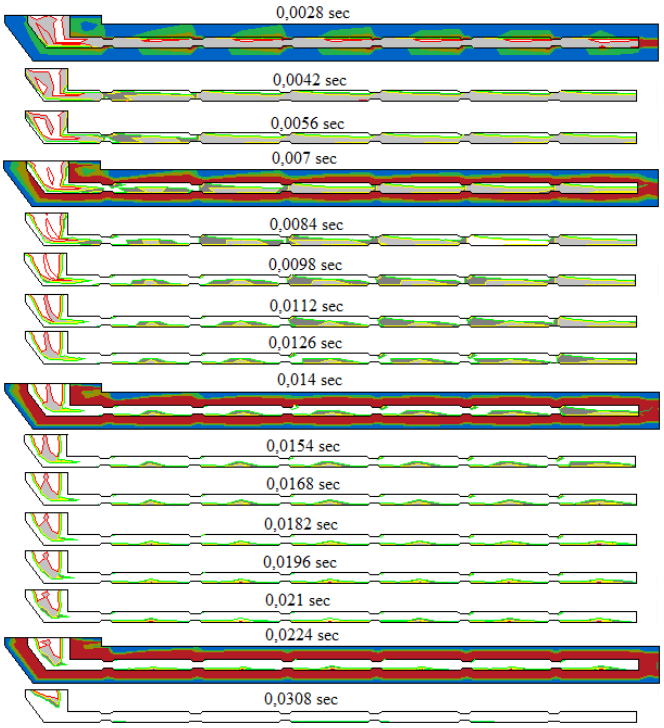
Fig. 2 *The place of the K-test in the process of forming the structure in a first-order phase transition in a casting technology.*

2. Computational Physics - Melt Solidification Temperature Range in the K-Test

The mathematical model for the calculation of the hardening temperature field is the 3D task of Stefan-Schwarz realized with the finite element method at the dates: $\alpha_{C|M}$ = 56000 w/m^2 K, $\alpha_{M|Ar.media}$ = 28000 w/m^2 K, λ_L =104 w/m K, c_L = 30,54 J/kg K, ρ_L = 2500 kg/m^3, λ_S = 83 w/m s K, c_S =30,54 J/kg K, ρ_S = 2500 kg/m^3, $T_m \pm \Delta$= 554 ± 3,5 ° C, Q_L = 160000 J/kg $T_{0|M}$ = 20 ° C, $T_{0|C}$ = 558 ° C



a) Cast and mold for K-test;



b) Temperature field of solidification in K-test;

Fig. 3 *The role of K-test for the first order phase transition before every castings is the give important technological information.*

The K-test is a visual estimate of the number of non-metallic inclusions of the rapidly-validated sample castings (Figure 3a) from a casting grade. Repeat gravitational flooding in a molten metallic form is done several times. The transverse grooves on the top and bottom surfaces of the slab form the places of rupture. It is believed that the retention of non-metallic inclusions from the melt increases in the channels due to some retention effect.

In Fig. 4 are represented by: a rapid crystallized test sample for the K-test (Fig 3a) and the resultant casting structure of a type of care wheel

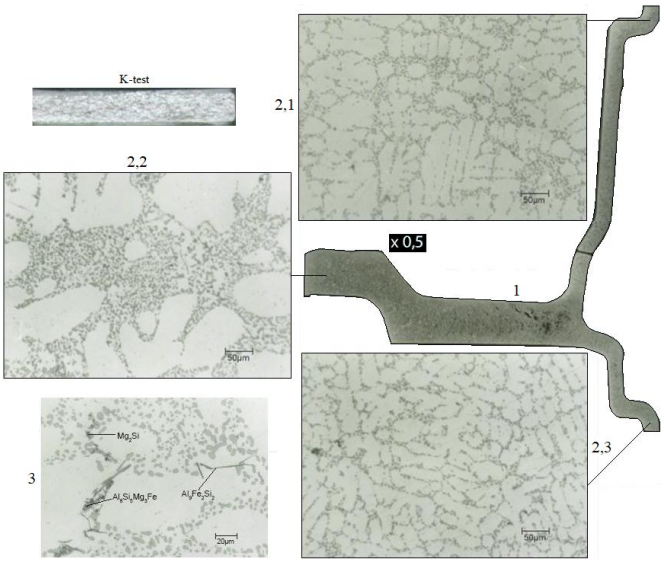


Fig. 4 *Lom on the K-test for visual observation. Polycrystalline structures obtained in local casting volumes: 1 macro-grinding; micro-grindings: (2,1 2,2 2,3); Phases in solid material 3.*

Fig. 3 is the most important information: K-test of liquids → phase transition of first order → real structure of solid body → work properties. Fig. 4 introduced **mathematical experiment**: numerical investigation of the solidification and results **Local solidification velocity.** Stefan-Schwartz task is the bridge (Fig. 1) and it is bridge between theoretical thermodynamics and (metal physics + theory of solid body).

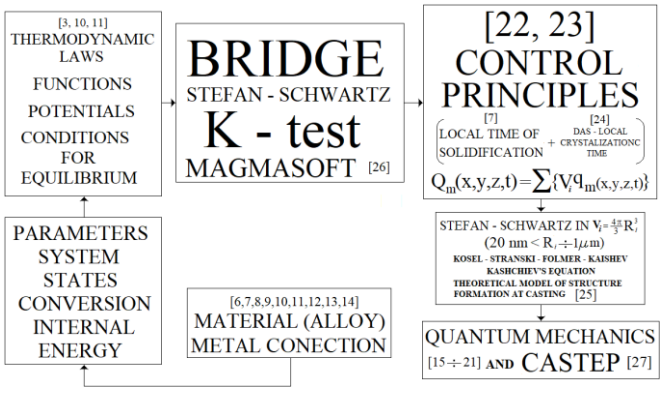


Fig. 5 Mathematical experiment and Computational physics.

Types of Chemical connection: Ion crystals Ion crystals - the crystal lattice is composed of oppositely charged ions connected by an ionic bond; Valence crystals - the atoms are connected in a crystal lattice with covalent (or homeopolar) bonds; Metals - a crystalline lattice made up of positive ions, whose repulsive senses are counterbalanced by free electrons; Molecular crystals - a grid built of separate molecules or atoms interconnected with intermolecular (of Van der Waals) forces. It is well known, that electrostatic nature of chemical connection is attraction and repulsion of electrical charges [9]. Chemical connection are defined from electron structure of the interaction atoms and effects of quantum character of the electrons movement: The energy of ionization J of a neutral atom is the difference with a negative sign (-) between the energy of the atom in its basic state and the energy of the single (+) ion (also in the basic state). J (measured eV), associated with the electronic structure, and the periodic change of the properties of the chemical elements; Energy of the kernel of electrons (electronic affinity) ζ. Many atoms of chemical elements are connected to an additional electron by releasing energy equal to the difference between the energy of the neutral atom in basic state and the energy of the basic state of the corresponding negative ion; Electro-negative based on J and ζ characterizes the ability of atoms in a molecule to attract electrons to itself, atom A associates an electron by cleavage from atom B. When $J_B - \zeta_A < J_A - \zeta_B$ or $J_A + \zeta_A > J_B + \zeta_B$ the electron will strive to move from atom B to atom A i.e. $J_A + \zeta_A$ or the semi-sum $x = (J_A + \zeta_A)/2$ (Mulliken) is a quantitative measure of electro-negative. The energy of the ionic (chemical) bond U is the difference from the interaction energy W and the difference $(- J + \zeta)$ needed to form neutral positive and neutral ions $U = W - (- J + \zeta) = W + J - \zeta$. The energy of the ion crystal lattice between *i-th* and *j-th* ions is sum: a potential energy of interaction W_{ij}; repulsing forces; potential energy of coulomb interaction $W_i = \Sigma_j W_{ij}$. If the surface effects are neglected, the full energy U of a crystal composed of 2N ion or N molecules is: $U = NW_i = NW$. *Methodology for application is* – the necessary work φ spent on approaching two charges or half a crystal ($\varphi_{K/2}$) is: $\varphi = q_1 q_2/4\pi\varepsilon_0 r$, $\varphi_{K/2} = e/4\pi\varepsilon_0 r(-e/1\ e/2 - e/3 + e/4 - \cdots) = (-e^2/4\pi\varepsilon_0 r) ln2$, or $\varphi_{1/2} \equiv (-e^2/4\pi\varepsilon_0 r)\Phi$, where Φ corresponds of $ln2 \Rightarrow$ there is a need for work to create a 3D lattice of a large number of particles, among which only coulomb forces $E_{Lattice} = (-e^2/4\pi\varepsilon_0 r)\Phi$, where $E_{Lattice}$ is the lattice energy, Φ is constant of Madelung [10].In the metal bond, valence electrons are also called generic. They move in the force field of the atoms of the lattice, forming the lattice; are not localized around their atoms but move freely; and interact with one another. In their movement electrons do not disturb the chemical properties of metals. The number of electrons of each atom does not change. The energy of each individual bond in the metal grid is smaller than in a two-atom metal molecule, and the inter-atomic distances are correspondingly larger. Metal alloys are solid solutions. The crystal lattices of the alloys can be: substitution solutions at comparable sizes of different atoms; incorporation solutions when smaller size atoms are introduced into the crystal lattice by atoms of larger size. For describing the structures and properties of metals and materials in general, quantum mechanics is used to search for the corresponding solutions of the Schrödinger equation

$$-\hbar^2\nabla^2\psi(\boldsymbol{r})/2m + V(\boldsymbol{r})\psi(\boldsymbol{r}) = E\psi(\boldsymbol{r}),$$

$$\psi_k(\boldsymbol{r}) = exp(i\boldsymbol{k}.\boldsymbol{r})u_k(\boldsymbol{r}),$$

$$u_k(\boldsymbol{r}) = u_k(\boldsymbol{r} + T_n),$$

where m is the mass of the electron; $\hbar$ is a Planck constant; *V* is the periodic potential of the interaction electron/(all other electrons); ψ is a wave function, a solution to the Schrödinger equation; $\boldsymbol{k}$ is a vector defined by the vector base $\mathbf{t}_1$, $\mathbf{t}_2$ and $\mathbf{t}_3$ of the crystal Brave lattice $\mathbf{T}_{n_1n_2n_3} = n_1\mathbf{t}_1 + n_2\mathbf{t}_2 + n_3\mathbf{t}_3 \equiv \mathbf{T}_n$, n is the number of the ordered numbers (n_1, n_2, n_3); u_k is a periodic function with the period of *V*.

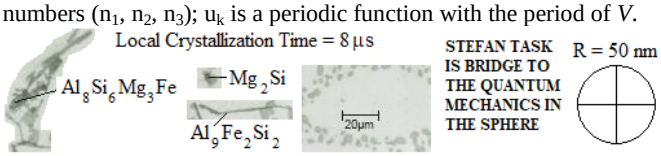


Fig. 6 *Character phases (Fig. 4, 3); sphere R = 50 nm which cannot see in the scale 20 μm; Local Crystallization Time LCT = (20/10)³=8 μs.*

Stefan's task in a sphere with a radius of R_{nm} = 50 nm is our proposal for a bridge between the task of Stephen-Schwartz (the first-order phase transition) and the general theorem of Pauli's quantum mechanics [10]. V is volume in Euclidean space; N is the sum of the electrons of the conductivity (e-gas) n = N/V and:

$$\left(\frac{4\pi}{3}p_0^3V = \frac{N}{2}\hbar^3;\ p_0 = \hbar\left(\frac{3n}{8\pi}\right)^{1/3};\ E_0 = \frac{\hbar^2}{2m}\left(\frac{3n}{8\pi}\right)^{2/3}\right) \leftrightarrow V_{nm} = \frac{4\pi}{3}R_{nm}^3, \quad (1)$$

for a particular material (alloy), a necessary geometric matching is sought for the formation of the polycrystalline structure in the die by Stefan's task in the sphere volume with radius R = 50 nm:

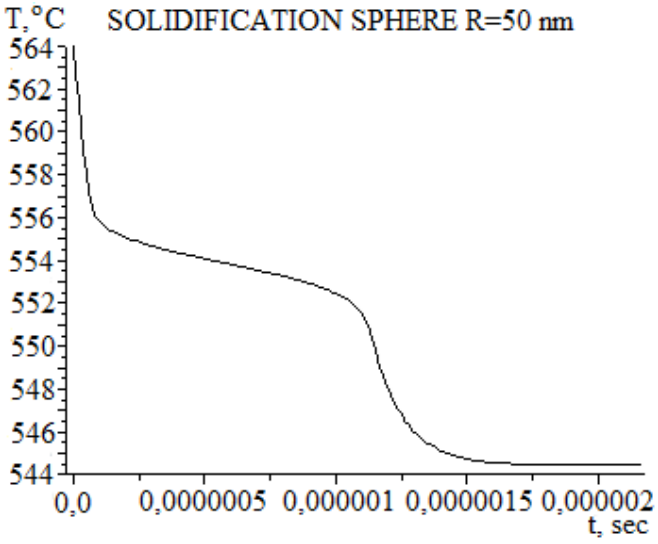


Fig. 7 *Time-temperature curve of solidification of nano-sphere from melt of aluminum alloy (Fig. 3), i. e. conditions of local solidification.*

The process of solidification in a radius sphere, 50 nm is a convenient tool for connecting foundry (MAGMASOFT) and Quantum mechanics (CASTEP) software (first-principles). This software are convention for using the methodology of mathematical experiment and computational physics [16, 17]. Application of CASTEP (or other software) to form a real polycrystalline structure is an important manufacturing tool.

3. Conclusions

1. A 3D Stefan-Schwartz mathematical model is applied in heat transfer with maximum intensity for a K-test. It is obtain the basic process in the real casting volume: the non-stationary temperature field of solidification (separating the latent heat) in the real macro-geometry in the phase transition zone.

2. Stephen's task in nano-volume was chosen as a bridge between software of quantum mechanics to description of structure formation at casting and for example MAGMASOFT.

4. References

1. B. Russell, The principles of mathematics, Taylor & Francis e-Library, 2009 ISBN 10: 0-203-86476-X

2. Gödel's Proof of Incompleteness - English Translation - James R Meyer, *https://www.jamesrmeyer.com/pdfs/godel-original-english.pdf*

3. E. Fermi, Thermodynamics, Prentice-Hall, INC, New York, 1937, Second stereotype edition, Publish house Harkov University, 1973.

4. P. A. M. Dirac, The principles of quantum mechanics, 3-rd edition, University Oxford press, Oxford, 1948.

5. A.H. Chokshi, A. Rosen, J. Karch, H. Gleiter, On the validity of the Hall-Petch relationship in nanocristalline materials, Scripta METALLURGICA Vol. 23, pp. 1679-1684, 1989.

6. A. Balevski, Metalscience, Technics, Sofia, 1962. (In Bulgarian)

7. M. Flemings, Solidification Processing, Peace, Moscow, 1977. (In Russian)

8. J. Blakemore, Solid state physics, Metallurgy, Moscow, 1972. (In Russian)

9. M. Borisov, K. Marinova, Introduction of physics of the solid body part I, Science and Art, Sofia, 1977. (In Bulgarian)

10. G. Schulze, Physics of metals, Peace, Moscow, 1971, (In Russian)

11. Ts. Uzunov, Physics of metals, Technical University, Sofia, 2004. (In Bulgarian)

12. S. Vodenicharov, Dynamic destruction of metals structures, Bulged Ltd. (In Bulgarian) ISBN 978-954-92552-3-2

13. W. D. Callister, Materials Science and Engineering: an introduction, John Wiley & Sons, Inc., New York, 2007. ISBN-13: 978-0-471-73696-7

14. S. A. Saltikov, Stereometric metallography, Metallurgy, Moscow, 1976. (In Russian)

15. R. H. F. Jackson, P. T. Boggs, S. G. Nash, S. Powell, Guidelines for reporting results of computational experiments. Report of the ad not committee, Mathematical programing 45 (1991) 413-425, North Holland.

16. T. Chernogorova, These of Professor, The method of computational experiment to processes from metallurgy, laser physics, ecology and financial, Bulgarian academy of sciences, Institute of Mathematics, 2013. (In Bulgarian)

17. U. Landman. Materials by numbers: Computations as tools of discovery, PNAS, May 10, 2005, vol. 102, no. 19 6671–6678.

18. D. H. Bailey and J. M. Borwein, Experimental mathematics: Examples, Methods and Implications, Notice of the AMS, volume 52, Number 5, 2005.

19. D. I. Khomskii, Basic Aspect of the Quantum Theory of Solids, Cambridge University Pres, 2010, ISBN-13 978-0-511-78832-1

20. M. Sigrist, Solid State Theory, Lecture website http://www.itp.phys.ethz.ch/education/fs14/sst

21. K. R. Nesbet, Variational principles and methods in theoretical physics and chemistry, 2002, eBook ISBN 0-511-04162-4

22. S. Bushev, These of PhD, Controllability problems of crystallization process in casting, TU – Sofia, 1993.

23. S. Bushev, G. Moumdjian, A possibility to influence the dynamics of a phase transition of first order during casting in open thermodynamic systems, Comptes rendus de l'Académie bulgare des Sciences, Tome 46, N^{o} 7, p.27-30, 1993.

24. A. Maneva, These of PhD, Investigation of the structure and properties of castings from subeutectic aluminum alloys depending on the ratio of primary and secondary alloys, Bulgarian academy of sciences, Institute of metal science, equipment and technology with hydro- and aerodynamic center „acad. A. Balevski", Sofia, 2013. (In Bulgarian)

25. S. Bushev, Theoretical model of structure formation in die casting, XXII International scientific technical conference „FOUNDRY 2015", 16-17 April 2015 Pleven, Bulgaria (In Bulgarian)

26. G. Evt. Georgiev, The new Tools for Automatic Optimization of Casting Technologies in the Latest Version of MAGMASOFT – MAGMA5.3.7, Proceedings of Sixth National Conf. with Int. Participation "Material science, Hydro- and Aerodynamics and National Security", May, 29-30, **ISSN 1313-8308,** pp.145-149, 2017.

27. CASTEP, www.tcm.phy.cam.ac.uk/castep/oxford/castep.pdf

THE MAXIMAL VALUES OF PACKING COEFFICIENT FOR PARTICLES WITH DIFFERENT FORMS

Prof. Dr. Phys. and Math. Liopo V.[1], Mast. of Phys. Liaushuk I.[1], Assoc. Prof. Dr. Eng.Auchynnikau Y.[2] , Assoc. Prof. cand. Phys. and Math. Sabutz A.[1], Assoc. Prof. cand. Eng. Sarokin V.[2], PhD Yankov E.[3]
Faculty of Physics and Technology[1]– Yanka Kupala State University of Grodno, Belarus,
E-mail: liopo@grsu.by , ilavshuk@grsu.by , sabutz@grsu.by
Faculty of Innovative Technologies of Mechanical Engineering [2] – Yanka Kupala State University of Grodno, Belarus,
E-mail: ovchin@grsu.by, sorvg@grsu.by
University of Ruse 3 – Bulgaria
E-mail: eyankov@uni-ruse.bg

Abstract: *It was analyzed the methods of constructions the matter with maximal of packing coefficient when the objects consist of the particles with forms either spheres or rods or plates. It was calculated the relations the partial size for relating of maximal packing coefficient. As examples of objects with coefficient of packing theirs particles we look on abrasive materials and products of the powder metallurgy and solid fuel etc.*

KEYWORD: COMPOSITE, COEFFICIENT OF PACKING, CLOSED PACKING (*CP*), MAXIMAL CP, FORMS OF OBJECTS, SPHERE, ROD, PLATE.

1. Introduction

Composite materials represent a combination of two main components. Continual phase is a matrix or a basis of a composite, and disperse (extender modifier) of a component are created from particles of the substances which are usually different from substance of matrix. The aim of using of modifier is changing of composite material properties. Usually concentration of disperse fillers modifiers small – from a share percent to several tens percent.

But there are many of materials various functional purpose where mass and volume of particles concentration should have the greatest possible. The continual basis in this case has the function of sticking together substance that allows to receive objects of the big sizes. The coefficient of packing of particles in such materials is parameter on the size of which properties of an object depend.

The aim of the our research is to justify the use of packing coefficient as the numerical parameter of quality assessment of substances of various functional purpose.

The object of the research is composite materials with the maximal possible coefficient of packing of particles.

The subject of the research is the closed packings of particles of various form. On the example of spherical packing it is shown that the coefficient of packing can be increased, when particles with smaller radii r_{OC} and r_T are included into octahedral and tetrahedral emptiness respectively, in comparison with particles of the main phase *R*. The closed packings of particles of a cylindrical and plate form are considered.

The next research tasks are solved

1. To analyze the ratios of radii two spheres for achieve the maximal values of coefficient closed packing;
2. To calculate the maximal possible value of coefficient of *K* for spherical particles in the closed packing of spheres with *R*, r_T and r_{OC} radii;
3. To analyze the maximal value of closed packing coefficient for spherical, rod and plate particles.

2. The closed spherical packings

The coefficient of compactness of a system of discrete physical objects is equal to the relation of total volume of these objects (*V*) to the volume of all the system – (*W*), that is. $\left(K = {}^{V}\!/_{W}\right)$. This coefficient for the closed spherical packings equals $K \approx 74\%$. If in tetrahedral and octahedra spheres vacancies of the corresponding sizes are placed, then the coefficient of compactness increases. Materials with the increased value *K* are used in production of abrasive tools, products of powder metallurgy, solid-state fuel elements of different function, etc.

The Closed Packings of Spherical Particles (*CPSP*) are formed by next algorithm. The first step is construction closed packing monolayer of spherical particles. The second is the location the spheres between three spheres of the lower layer. This layer consist of the same the first layer. The spheres of the third layer may take place by two types. This spheres are located over the vacancies of second spheres but over the spheres of the first layer and the second possibility is location the third layer spheres over the vacancies of second layer and over the first too. At the same time ordered packings of two types are possible: three-layer … *ABCABCABC* … and two-layer … *ABABAB* … At the same time lattices with *FCC* cells (face-centered cubic) and *HCP* (hexagonal closed packing) of types (figure 1) are formed.

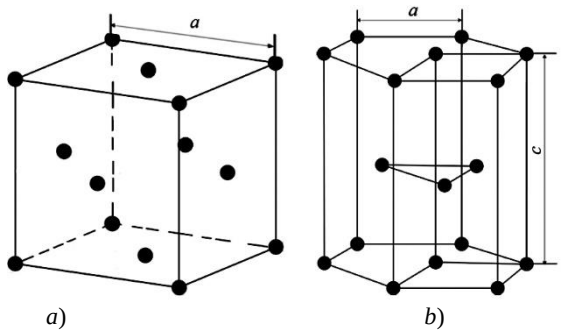
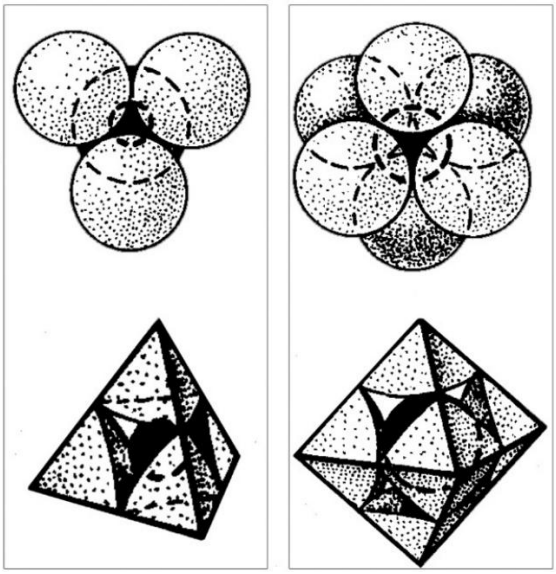


Fig. 1. *– Cells of lattices of three-layer and two-layer packings of identical spheres: a) FCC , b) HCP*

Parameters of cells of these packings: *FCC* – $a = b = c = 2\sqrt{2R}$, $\alpha = \beta = 90^\circ$, *HCP* – $a = b = 2R$, $c = 4\sqrt{6}R/3$, $\alpha = \beta = 90^\circ$, $\gamma = 120^\circ$ (α, β, γ – angular parameters of cells, *a*, *b*, *c* – linear parameters of cells) *R* – radii of spheres. Crystallographic coordinates of spheres in cells have the values: *FCC* – $(000)\left(\frac{1}{2}\frac{1}{2}0\right)\left(\frac{1}{2}0\frac{1}{2}\right)\left(0\frac{1}{2}\frac{1}{2}\right)$; *HCP* – $(000)\left(\frac{2}{3}\frac{1}{3}\frac{1}{2}\right)$ [1]. Therefore, compactness coefficients for the specified spherical systems have the values:

$$K = \frac{\pi}{3\sqrt{2}} \approx 74\%. \qquad (1)$$

Between spheres of the next layers in the closed spherical packings vacancies of tetrahedral and octahedral types (*TV* and *OV* respectively) are formed (figure 2).



a) tetrahedral *b*) octahedral

Fig. 2. *– Types of* vacancies *in the closed spherical packings* [*2, P. 104*]

Radii of spheres which can enter tetrahedral (r_{TV}) and in octahedral (r_{OV}) vacancies are equal:

$$\begin{aligned} r_{TV} &= R\left(\sqrt{\frac{3}{2}}-1\right) \approx 0,225R \\ r_{OV} &= R\left(\sqrt{2}-1\right) \approx 0,414R \end{aligned} . \qquad (2)$$

If $r_{TV} < 0,225R$ and $r_{OV} < 0,414R$ then the closed packing of spheres with a radii of R will not be destroyed. In the closed packing of spheres the *OD* systems are possible where the distribution of layers will look like:

...ABACBCBCABAC… .

that is, layers like *A*, *B*, *C* form a chaotic mixed layers, but only layers of different types can be found next to each other, their alternation in the direction normal to layers can be next. But in this case: first, the geometry of vacancies is preserved, and secondly, the compactness factor has the same value $K \approx 74\%$ [3].

The ratio of vacancies n_{TV} and n_{OV} to the total number of N spheres with a radius R is defined as follows: All spheres with a radii of R are in tops of structural polyhedrons (figure 2) which fill all volume of a system without admissions.

Volumes of tetrahedrons and octahedrons V_T, V_{OC} are the following:

$$\begin{aligned} V_T &= \frac{2}{3}\sqrt{2}R^3 \\ V_{OC} &= \frac{8}{3}\sqrt{2}R^3 \end{aligned} . \qquad (3)$$

Therefore,

$$K = \frac{N \cdot \frac{4}{3}\pi R^3}{n_T V_T + n_{OC} V_{OC}} = \frac{N \cdot \frac{4}{3}\pi R^3}{n_T \frac{2\sqrt{2}}{3} R^3 + n_{OC} \frac{8\sqrt{2}}{3} R^3} = \frac{\pi\sqrt{2}N}{n_T + 4n_{OC}} = \frac{\pi\sqrt{2}}{6}, \qquad (4)$$

that is,

$$n_T + 4n_{OC} = 6N . \qquad (5)$$

or

$$\frac{n_T}{N} + 4\frac{n_{OC}}{N} = 6 \qquad (6)$$

The condition (6) is applicable to any closed spherical packing including ordered ones. If N is the number of balls (atoms), then, taking into account the translation, n_i/N can have the value $1 \le n_i/N$ and must be a positive integer. As appears from (6) $n_{OC}/N = 1$ otherwise $n_T/N < 0$ which is impossible. Thus, the number of octahedral vacancies in the densest pack of N spheres is equal to N, and tetrahedral vacancies are $2N$. Naturally, this is true when boundary defects are not considered.

Coordinates of tetrahedral vacancies in *FCC* cell are the following:

$$\begin{matrix} \left(\frac{1}{4}\frac{1}{4}\frac{1}{4}\right)\left(\frac{3}{4}\frac{3}{4}\frac{1}{4}\right)\left(\frac{3}{4}\frac{1}{4}\frac{3}{4}\right)\left(\frac{1}{4}\frac{3}{4}\frac{3}{4}\right) \\ \left(\frac{1}{4}\frac{1}{4}\frac{3}{4}\right)\left(\frac{3}{4}\frac{3}{4}\frac{3}{4}\right)\left(\frac{3}{4}\frac{1}{4}\frac{1}{4}\right)\left(\frac{1}{4}\frac{3}{4}\frac{1}{4}\right) \end{matrix} . \qquad (7)$$

Coordinates of octahedral vacancies are located in points:

$$\left(\frac{1}{2}\frac{1}{2}\frac{1}{2}\right)\left(00\frac{1}{2}\right)\left(0\frac{1}{2}0\right)\left(\frac{1}{2}00\right). \qquad (8)$$

The centers of tetrahedral vacancies in a cell of *HMDP* are located in points:

$$\left(00\frac{3}{8}\right)\left(00\frac{5}{8}\right)\left(\frac{1}{2}\frac{3}{2}\frac{1}{8}\right)\left(\frac{1}{2}\frac{3}{2}\frac{7}{8}\right). \qquad (9)$$

Coordinates of octahedral vacancies in *HMDP* cell are:

$$\left(\frac{2}{3}\frac{1}{3}\frac{1}{4}\right)\left(\frac{2}{3}\frac{1}{3}\frac{3}{4}\right) \qquad (10)$$

Coordinates in (7-10) are specified in crystallographic basis.

Volumes of *FCC* and *HMDP* cells of the systems are equal:

$$V_{FCC} = 2V_{HMDP} = 16\sqrt{2}R^3$$

In large volumes it is impossible to obtain the closed packing in actual practice as $K_{\max} \approx 74\%$ for monodimensional spheres.

3.The increase in the coefficient of compactness the spheres packages

Let's consider the increase in the compactness factor K_0 compared to the packing of spheres of the same size on the basis of *HMDP* cell (*N*=2).

The change of coefficient of compactness is the following when filling octahedral vacancies:

$$\Delta K_{OC} = \frac{2 \cdot \frac{4}{3}\pi 0,414R^3}{8\sqrt{2R^3}} \approx 5,3\% . \quad (11)$$

When filling only tetrahedral vacancies, the change in the compactness coefficient is equal to:

$$\Delta K_T = \frac{4 \cdot \frac{4}{3}\pi 0,225R^3}{8\sqrt{2R^3}} \approx 1,7\% \quad (12)$$

Thus, the maximal value of the coefficient *K* for the densest packing of spheres with radii *R*, r_T and r_{OC} has the following value of (11-12):

$$K_{\max} \approx 74 + 5,3 + 1,7 \approx 81\% \quad (13)$$

If smaller spheres of the corresponding radii which form a tetrahedron around a sphere with a radii r_T are placed in vacancies of tetrahedrons between spheres of *R* and r_T, and small spheres forming octahedron around a ball with a radii of r_{OC} are placed in the octahedron, then the coefficient of compactness will still increase approximately by $\Delta K \approx 6\%$. All these conclusions describe the case with strict distribution of spheres with a radii r_T and radii r_{OC} and also smaller spheres.

If the property of plasticity is inherent in spherical particles, then with a hydrostatic pressure it is possible to reach the packing coefficient coming to $K_{\max} \approx 100\%$. The difference from this value is defined by the total volume of the interpartial areas filled, for example, with the glue substance.

4. Packing of non-spherical particles

If particles have the non-spherical form, for example, cylindrical or plate, then the coefficient of packing of K_{max} will exceed 74%. So, for particles of a cylindrical form at identical radii it is: $K_{\max} = \frac{\pi}{2\sqrt{3}} \approx 90\%$

If cylinders with radii *r* equal to $r_{med} = R\left(\frac{2}{3}\sqrt{3} - 1\right)$ are placed in the void between the cylinders then

$$K_{\max} = \frac{\pi R^2 + \pi r^2}{2R^2\sqrt{3}} \approx 93\%$$

It is assumed that the bases of cylindrical particles are connected without gaps. When systems from particles of a cylindrical form emerge the formation of their mutual configuration as liquid crystals is possible.

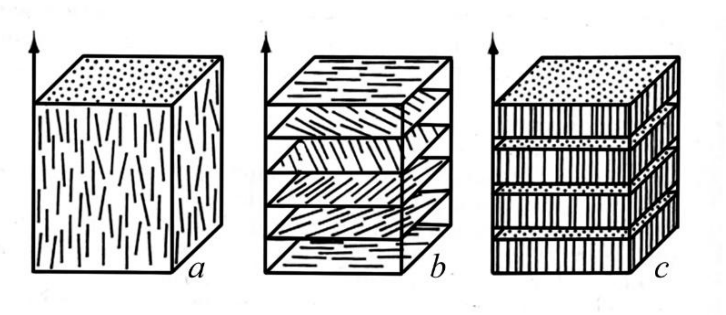


***Fig. 3.** – Schemes of liquid crystals with linear molecules: a – nematic, b– cholesteric, c– smectic* [*2, P. 186*]

In all cases, the resulting substance will have anisotropic properties. If the particles are in the form of plates, then theoretically the packing coefficient can be close to 100%. K_{max}, is caused by contacts between the plates. To achieve K_{max} for rod, and also for plate particles they should be textured in substance.

5. Packing coefficient as process parameter

The idealized model packings considered above will not correspond to real objects due to a number of factors. For example, in a model of spherical packings there can be various areas, even with the closed packing, with contacts between them breaking this condition. For cylindrical and plate particles their chaotic mutual configurations, which means possible lack of texture. Particles in ideal models have some sizes (radii of spheres, radii of cross sections of cylinders, thickness of plates) with identical values. In practice these parameters are described by the corresponding statistical distributions.

In formation of packings in the conditions of hydrostatic pressure spherical particles will get a form of polyhedrons Voronoy [4]. If for particles with various sizes their mechanical properties are various (for example, coefficients of their plasticity), then particles will get a form of polyhedrons Delone. From this it follows that with an identical mass of powder of particles of which the three-dimensional object is made coefficients of compactness can be various. If the mass of particles is equal to *m*, and their density in substance is ρ then, knowing the volume of the product created from these particles (*W*), the coefficient of compactness is defined by the condition:

$$K = \frac{m\bar{\rho}}{\rho M} \quad (14)$$

where *M* is the mass of the created object. If particles of initial material did not undergo changes (were not oxidized, did not receive residual deformations, did not undergo phase transformations) in the course of its production, then $m = M$ and ρ remains invariable, therefore

$$K = \frac{\bar{\rho}}{\rho} \quad (15)$$

where $\bar{\rho}$ is the density of the final product.

For real objects, knowing the sizes of particles of the main substance, for conditions when $K = K_{\max}$, it is possible to calculate necessary concentration of smaller particles.

Therefore, it is possible to determine density of systems of the closed packings corresponding to models. When comparing experimental density, the studied substances with their values at $K = K_{\max}$ the parameter will be received which can correlate with properties of the all system.

Thus experimental value ρ can act as a process parameter for the analysis of an object at variations of concentration, the sizes, forms, etc. when, for example, the compared objects with identical initial structures.

6. Conclusion

Small disperse materials with sizes of particles from 10^{-6} to 10^{-9} *m* can be used as fillers modifiers, for example, of polymeric composite materials. But there are substances which cornerstone only fine particles are, and concentration of glue substance does not exceed several percent. Abrasive materials, solid-state fuel elements, products of powder metallurgy, etc. belong to this category. The technological properties of such substances depend on the coefficient of *K* – compactness (packing) of the particles.

The work shows that it is possible to increase the greatest possible value of coefficient of *K* for particles of spherical shape to 81%. For cylindrical and plate particles it can approach 100%. This coefficient can be calculated only for model objects. For substances with $K = K_{\max}$ it is possible to calculate the value of density ρ. The relation of an experimental density to ρ describes difference of packing of particles in an object from their ideal model.

Therefore, this experimental value can be used as technological, and especially hierarchical characteristic to analyze the impact of changes of conditions of formation of the substances created from fine particles.

7. References

1. **Vainshtein, B.** Sovremennaja kristallografija, Moscow, Nauka, 1979. Vol. 1. 384 p.
2. **Vainshtein, B.** Sovremennaja kristallografija, Moscow, Nauka, 1979. Vol. 2. 360 p.
3. **Conway, J., Sloane, N**. Sphere Packings, Lattices, and Groups, New York , Springer-Verlag, 1999. 703 p.
4. **Galiulin, R.** Kristallograficheskaia karta mira., Uspekhi fiz. Nauk, 2002. Vol. 172, № 2, p. 229 – 233.